University of Alberta

Synthesis and Characterization of Functional Iron and Germanium Nanomaterials

by

Melanie Hoffman

A thesis submitted to the Faculty of Graduate Studies and Research
in partial fulfillment of the requirements for the degree of

Doctor of Philosophy

Department of Chemistry

Fall 2012
Edmonton, Alberta

I dedicate this thesis to

Detlef Werner

~ an inspirational teacher

Abstract

Germanium nanomaterials have many potential applications based on their size-tunable optical and electronic properties, for example in photodetectors, photovoltaics and non-volatile memory.

In this work, the synthesis of Ge nanoparticles by two different methods based on tailorability through the substituent chemistry of the Ge precursors is explored.

In Chapter Two, the effect of the organic substituent upon thermal decomposition of organogermanium oxides $(RGeO_{1.5})_n$ to yield oxide-embedded germanium nanocrystals (Ge-NCs) is investigated. Substituents with stable radical formation or the presence of β-hydrogen are found to facilitate NC formation at lower temperatures. Lower temperature limits germanium production to a pathway based on disproportionation only, and not – as previously – also on hydrogen reduction of germanium oxides. The organic substituent also introduces tailorability of organogermanium oxide properties, such as melting points. For R = *n*-butyl, benzyl, these are lowered below the disproportionation temperature, yielding melts containing Ge-NCs.

The knowledge gained in the substituent study is applied to solution synthesis of Ge-NCs in Chapter Three. The *n*-butyl substituent, which formed Ge-NC from $(n\text{BuGeO}_{1.5})_n$ at 300 °C, can eliminate by radical and β-hydride elimination pathways. In the molecular compounds $n\text{Bu}_x\text{GeH}_{4-x}$ (x = 1-4), reductive elimination also becomes possible. We propose this leads to the decrease in decomposition temperature of $n\text{Bu}_x\text{GeH}_{4-x}$ from x = 4 to x = 1.

In the second section of this thesis, Chapter Four, the catalytic activity of metal-decorated iron/iron-oxide core-shell nanoparticles (M/Fe@Fe_xO_y) in Heck and Suzuki couplings is investigated. Electroless deposition of noble metals on Fe@Fe_xO_y generates the catalyst. The catalytic activity of Pd/Fe@Fe_xO_y is improved over standard heterogeneous catalysts (*e.g.*, Pd/C) in Heck coupling of styrene and bromobenzene. Leaching studies in Suzuki coupling of bromobenzene with phenylboronic acid show elevated Pd levels in solution during reaction, suggesting Pd is solvated during catalysis in a quasi-homogeneous mechanism. Less Pd is found in the final product, suggesting Pd is deposited back onto the Fe@Fe_xO_y support after catalysis.

In Chapter Five, a summary of our findings regarding the effects of organic substituents on Ge-NC synthesis and catalysis employing metal-decorated Fe@Fe_xO_y is presented, followed by a detailed discussion of future research directions.

Acknowledgments

Almost 10% of my high school graduate class are females in Chemistry. I have many people to thank for paving my way to where I am now, many of whom I will forget as I do what I always do best .. finish last minute. But the person I would like to acknowledge first is the person that inspired so many of us to go and explore chemistry. My personal interest in nanoscale materials stems from the enthusiasm with which my late high school teacher Detlef Werner unfolded the world of chemistry applications before us, in particular with his passion and interest for everything "nano". Danke, Herr Werner, dass Sie mich hierzu inspiriert haben!

Next, of course, is the man I can thank for keeping me in the program – and yes, my husband played a big role in that, too, but we'll save him for later. Right now, I want to thank Jon. Jon, I appreciate you in so many ways that I can't bring them all onto paper here at this time. Throughout my time in the group, you have always been positively encouraging to me personally, and left me the freedom of pondering the next step without much pressure. At times, that was maybe more challenging in a way, but it has also been an immensely forming and useful learning experience that I am very grateful for. You teach your students to be independent without abandoning us. You check in regularly, you give advice, man I wish I had learnt your sales pitch! But above all, you see us as human beings, not as science slaves, which is probably one of the major reasons I didn't give up on grad school. Becoming part of your research family has been a great journey, thank you for guiding me on it, and thank you so much for having so much fun with us along the way!

Part of all that fun have been the numerous Veinot graduates that I have had the honour of working and drinking beer and working out and getting married with (*not* to!). Janet, though I find your footsteps a few sizes too big for me to step into, I idolize you as my first grad student mentor! Thank you for sharing your wisdom, and your stories. De-Ann, Eric, Shaune, the workout team before Joel wanted to beat Jose in weightlifting – thank you for all the insightful chats and your motivated coaching in the pool and on the track! I would also like to

acknowledge Colin Hessel for being a big(headed) scary teddy bear who was apparently just poorly understood. Mike Dang, you little doctor in the making, don't hassle the Hoff! Joel Kelly, thank you for your endless science love, many an enjoyable coffee break and an after work beer, as well as a home for a summer!! Team wedding-ready breathed your exercise routine, and you are the first person that has made me enjoy being at the gym – together with Jose and Weggli of course!! Jose! Thank you for getting me on a summer soccer team on a regular basis! Way to go team captain! You have always given me a place to feel at home between all the science-crazies that were the rest of the Veinotites when I joined the group. Weggli – you have become such an amazing friend, and I am endlessly grateful for all the times we have shared – craziness, happiness, bixibikingness, nyancatness .. just plain amazing! A shoutout also to everyone else in the group – sorry, I am seriously running out of time!!

Adam, you go right along with that nyancatness, what an amazing time grad school has been with you, you have been a great friend, someone to lean on and have a lot of fun with and sing 99 Luftballons with, too. Mind-blowing, almost like SPACE!!

I know I am leaving out many people here that I love – know that I hold you dearly in my heart, and I am grateful for all the times we have spent and the contributions you have made to me getting to where I am now. I appreciate you!!

I would like to thank my committee for helping me make this work come together in the form it is now, and everyone in the Chemistry Department and at U of A who have become friendly faces that I enjoy being around so much after all these years! Thank you for all the support you have given me over the last years!!

Thank you also to my German Bestie, Doni, for always lending an open ear and spending many a lunch break skyping and exchanging the pains of student life – oh how we will miss it! But now we have Robbie Williams to look forward to next summer – thanks to him, too!

I would like to thank Jana for teaching me to say “I am good” to myself, and for becoming a lovely friend over the years, and Beckmo for spending many a Scrabble night at Steeps saving me from the depths of thesis terror.

Lastly, I would like to thank my family for being ever so supportive of my endeavours. Kate and Mike, I thank you so much for taking me into your home six years ago and being the catalyst for this exciting journey that took me out of Germany to new and exciting adventures. I appreciate everything you have done and continue to do for me, and am so happy to have a family that is full of great friends!! It has also been wonderful to grow into the Hoffman family, where there is so much love and happiness and maple salmon and Nutella cupcakes. What a lucky girl I am!

Mum, I admire how you never make me feel bad for being so far away, and have always encouraged me to go out and explore and live my life to the fullest. I miss you guys, but what an experience it has been how distance can bring you closer. Armin, thank you for being a great “father” and seeing us through everything!! Thank you to my brother for the many cheers you bring into my life. Ian, you’re a blast and I love you so much!

And finally, I would like to thank my amazing husband, without whom I would now be fat and unhappy and would probably never have clean clothes to wear. Sean, you are the backbone of my life, you give me the strength and stability to just keep on trucking and see things through to the end, and to find happiness as I go along. Thank you for the endless hours you have spent waiting for me, or passing your time without me because I was once again busy at work, and for never holding it against me. I love you in so many ways, thank you for being my partner and friend, and so much more!

Thank you everybody!!!

Table of Contents

Chapter 1: Introduction 1

1.1. An Introduction to Nanoscience 2

1.2. How Nano is Different – Size-Dependent Properties 9

1.2.1. The Importance of the Surface 9

1.2.2. The Effect of Size on Magnetic Properties 10

1.2.3. Optical and Electronic Properties at the Nanoscale 11

1.2.3.1. Molecules 12

1.2.3.2. Bulk Solids 13

1.2.3.2.a. Structure and Bonding Types 13

1.2.3.2.b. The Bulk "MO Diagram": Band Structures 15

1.2.3.3. Optical and Electronic Quantum Size Effects 19

1.3. Scope of this Thesis 22

1.4. References 25

Chapter 2: Understanding the Formation of Elemental Germanium by Thermolysis of Sol-Gel Derived Organogermanium Oxide Polymers 28

2.1. Introduction 29

2.1.1. Germanium nanocrystal synthesis 30

2.1.1.1. Zintl salt metathesis 30

2.1.1.2. Reduction of germanium halides 31

2.1.1.3. Thermal decomposition 36

2.1.1.4. Plasma pyrolysis 38

2.1.1.5. Solid-state and physical methods 38

2.1.2. Background of the current study 41

2.2. Experimental Details 44

2.2.1. Material Preparation 44

2.2.1.1. Reagents and Materials 44

2.2.1.2. Polymer preparation 44

2.2.1.3. Composite preparation 45

2.2.2. Material Characterization 46

2.2.2.1. Fourier-Transform Infrared Spectroscopy (FT-IR) 46

2.2.2.2. Thermogravimetric Analysis (TGA) 46

2.2.2.3. Matrix Assisted Laser Desorption Ionization Mass Spectrometry (MALDI-MS) 47
2.2.2.4. X-Ray Crystallography 47
2.2.2.5. X-Ray Diffraction (XRD) 47
2.2.2.6. X-Ray Photoelectron Spectroscopy (XPS) 47
2.2.2.7. Elemental Analysis (EA) 48
2.2.2.8. Transmission Electron Microscopy (TEM) 48
2.3. Results and Discussion 49
2.3.1. Synthesis of Ge-rich oxides by sol-gel polymerization 49
2.3.2. Formation of Ge-NC/GeO2 composites by thermal processing of Ge-rich oxides 61
2.3.3. Influence of processing temperature, time and atmosphere on Ge-NC formation 70
2.4. Conclusions and Future Work 75
2.5. References 77

Chapter 3: The Influence of Substitution on Thermal Decomposition of Molecular n-Butylgermanes to Germanium Nanoparticles 80
3.1 Introduction 81
3.2 Experimental Details 96
3.2.1 Material Preparation 96
3.2.1.1 Reagents and Materials 96
3.2.1.2 Identification of a suitable solvent 96
3.2.1.3 Hot injection synthesis of Ge NPs 97
3.2.2 Material Characterization 100
3.2.2.1 Fourier-Transform Infrared Spectroscopy (FT-IR) 100
3.2.2.2 Thermogravimetric Analysis (TGA) 101
3.2.2.3 X-Ray Diffraction (XRD) 101
3.2.2.4 X-Ray Photoelectron Spectroscopy (XPS) 101
3.2.2.5 Elemental Analysis (EA) 102
3.2.2.6 Transmission Electron Microscopy (TEM) 102
3.2.2.7 Raman Spectroscopy 102
3.3 Results and Discussion 103
3.3.1 Qualitative Determination of Decomposition Temperatures 103
3.3.2 Hot Injection at High Temperature (400 °C) 105
3.3.3 Hot Injection at Lower Temperature (325 °C) 113

3.3.4 Hot Injection at Lower Temperature (325 °C) in Trioctylamine (TOA) 117
3.4 Conclusions and Future Work 122
3.5 References 123

Chapter 4: Metal Decorated Iron/Iron Oxide Core-Shell Nanoparticles as Recoverable Catalyst Systems 126
4.1. Introduction 127
4.1.2. Heck and Suzuki Reactions 129
4.1.3. Iron/Iron Oxide Core-Shell Nanoparticles 132
4.2. Experimental Details 136
4.2.1. Material Preparation 136
4.2.1.1. Reagents and Materials 136
4.2.1.2. Synthesis of iron/iron oxide core-shell nanoparticles 136
4.2.1.3. Metal deposition on $Fe@Fe_xO_y$ 137
4.2.1.4. Heck reaction 138
4.2.1.5. Suzuki reaction 140
4.2.2. Material Characterization 143
4.2.2.1. Transmission Electron Microscopy (TEM) 143
4.2.2.2. X-Ray Photoelectron Spectroscopy (XPS) 143
4.2.2.3. Inductively coupled plasma mass spectrometry (ICP-MS) 144
4.2.2.4. Gas chromatography-mass spectrometry (GC-MS) 144
4.3. Results and Discussion 145
4.4. Conclusions and Future Work 153
4.5. References 155

Chapter 5: Conclusions and Future Work 157
5.1. Germanium Nanoparticle Synthesis 158
5.1.1. Solid-State Synthesis from $RGeO_{1.5}$ 159
5.1.2. Future Work 160
5.1.3. Solution Synthesis by Hot Injection of $n Bu_xGeH_{4-x}$ 164

5.1.4. Future Work in nBu$_x$GeH$_{4-x}$-based Synthesis 165
5.2. Metal-Decorated Iron/Iron Oxide Nanoparticles in Catalysis 168
5.2.1. Conclusions 168
5.2.2. Future Work 169
5.3. References 174
Appendix A: Supplementary Data for Chapter 2 178

Appendix B: Oxide and Semiconductor Patterned Surfaces Based on Sol-Gel Chemistry within Block-Copolymer Micelles 185

List of Tables

Table 2.1. Summary of sol-gel polymerization reactions. 45

Table 2.2. Mass loss observed in Thermogravimetric Analysis (TGA) 57

Table 2.3. Summary of sample processing showing lowest temperature at which Ge-NC formation was observed in XRD along with Scherrer analysis results for Ge- NC diameters. All samples were processed for 1 h in 5% H_2/95% Ar. 63

Table 3.1. Ge-C bond strengths for different organic substituents in mono- and tetraalkylgermanes. 88

Table 3.1. Reaction conditions for hot injection of $n\text{Bu}_x\text{GeH}_{4-x}$.....100

Table 4.1. Metal loading of $\text{Fe@Fe}_x\text{O}_y$.....138

Table 4.2. Heck reaction conditions.....140

Table 4.3. Suzuki reaction conditions 142

List of Figures

Figure 1.1. Nanomaterials confined in (a) one, (b) two and (c) three dimensions. 2

Figure 1.2. When relating the size of a 3-4 nm nanoparticle to a football the scale-up compares to relating a football to the size of the Earth.[4,5] 3

Figure 1.3. The Lycurgus cup, (a) in reflected light, (b) in transmitted light, (both ©Trustees of the British Museum, reproduced with permission). 4

Figure 1.4. Diagram of interactions in electron microscopy, adapted from ref. 14 6

Figure 1.5. (a) The principle of STM and AFM is to probe the contour of a surface with an atomically sharp tip that is moved at a distance to the surface to maintain a constant tunnelling current (STM) or a constant force (AFM) (adapted from ref. 21). Examples of images are shown in (b)-(e): Xenon atoms manipulated by STM on a Ni (110) surface,[22] (c) ball-and-stick model of pentacene, (d) STM image of pentacene, (e) AFM image of pentacene, recorded with a CO-terminated tip.[23] Images (c)-(e) adapted from ref. 23 8

Figure 1.6. Molecular orbital diagram of dihydrogen: The 1s orbitals of two hydrogen atoms, shown at the left and right hand side, combine to form bonding (lowered in energy) and antibonding molecular orbitals (raised in energy) in the molecule H_2, shown at the centre. 13

Figure 1.7. Bands are depicted as continuous due to the extremely close spacing of ~N_A energy states in a solid A_n. To describe the band structure in more detail, the band can be deconvoluted into energy states as a function of the momentum vector k. The band shown on the right is representative of an s- or p_z-orbital overlap. 16

Figure 1.8. Band structures for certain points in the Brillouin zones of (A) CdSe and (B) Ge, showing the respective direct and indirect band gap (transition marked by red arrows). Adapted from ref. 47 and 48. 18

Figure 1.9. The band gap between valence band (VB) and conduction band (CB) increases with decreasing crystal size. 20

Figure 2.1. Ge-NC sizes obtained from reduction by (a) $LiAlH_4$, (b) $Li(C_2H_5)_3BH$, (c) $LiBH_4$, (d) $NaBH_4$ (reproduced from ref. 5). 33

Figure 2.2. (A) Transmission electron micrograph (inset: high-resolution TEM) of Ge-NC 4 ± 1.7 nm in diameter. (B) NIR PL from Ge-NCs 3.2 – 4.0 nm in average diameter (reproduced from ref. 4).....36

Figure 2.3. High-resolution transmission electron micrograph of Ge-NCs liberated from a silicon dioxide matrix. Adapted from ref. 3.....39

Figure 2.4. X-Ray Diffraction Patterns of GRO powders **1-6** before thermal processing.....53

Figure 2.5. Ge 3d X-Ray Photoelectron Spectra of GROs **1-6** before thermal processing, and amorphous GeO_2 for reference.....54

Figure 2.6. Fourier-Transform Infrared Spectra of GROs **1-6** before thermal processing.....55

Figure 2.7. Thermogravimetric Analysis of GROs **1-6** before thermal processing.....56

Figure 2.8. X-Ray crystal structure perspective view of the $[(^tBuGe)_6O_9]$ molecule. Non-hydrogen atoms are represented by Gaussian ellipsoids at the 20% probability level. Hydrogen atoms are not shown. The full crystal structure report was published by Puff *et al.*[48] 58

Figure 2.9. Photograph showing the physical appearance of GROs **1-5** (left to right, bottom) and corresponding Ge-NC/GeO_2 composites **7-11** (left to right, top). **8** and **10** are processed on Si wafer pieces.....62

Figure 2.10. X-ray diffraction (XRD) patterns for GROs processed at the lowest Ge NC-forming temperature as indicated in Table 2.3. A standard bulk Ge pattern is included for comparison. 64

Figure 2.11. (A) Transmission electron micrograph of **7** (R = ethyl). Dotted lines highlight areas where the presence of Ge-NCs is suggested by a region of darker contrast. (B) High-resolution transmission electron micrograph of **7** (R = ethyl) showing lattice fringes of a Ge-NC embedded in amorphous oxide. (C) Close-up of the Ge(111) lattice fringes 64

Figure 2.12. X-ray photoelectron (XP) spectra of the Ge 3d region for GROs (dashed lines) and their composites obtained from processing at the lowest Ge NC- forming temperature as indicated in Table 2.3 (solid lines). The XP spectrum of amorphous GeO_2 is included for comparison. 67

Figure 2.13. Fourier-transform infrared (FT-IR) spectra for GROs processed at the lowest Ge NC-forming temperature as indicated in Table 2.3 68

Figure 2.14. Elemental analysis (EA) of the hydrocarbon content of GROs processed at the lowest Ge NC-forming temperature as indicated in Table 2.3. The precursor GROs are included for comparison 69

Figure 2.15. X-ray powder diffraction (XRD) patterns for **1** (R = ethyl) and its composites processed at indicated peak temperatures in 5% H_2/95% Ar (left) or 100% Ar atmosphere (right). 71

Figure 2.16. X-ray photoelectron (XP) spectra of the Ge 3d region for **1** (R = ethyl) and its composites processed at indicated peak temperatures in 5% H_2/95% Ar (left) or 100% Ar atmosphere (right). 73

Figure 2.17. Fourier-transform infrared (FT-IR) spectra for **1** (R = ethyl) and its composites processed at indicated peak temperatures in 5% H_2/95% Ar (left) or 100% Ar atmosphere (right). 75

Figure 3.1. Graph comparing literature reports of Ge PL with predictions based on the effective mass approximation.[6-23] Data points represent reported Ge-NC diameters, plotted with error bars to represent either standard deviation (where available) or particle diameter ranges where average and standard deviation were not reported..... 84

Figure 3.2. Nucleation and Growth as a function of monomer concentration as proposed by the LaMer theory of burst nucleation (adapted from ref. 63). 93

Figure 3.3. (A) Experimental setup for solvent degassing, (B) Experimental setup for hot injection, with the area of injection indicated in pink 99

Figure 3.4. Photographs of hot injection products in octacosane and toluene from reactions of nBu$_2$GeH$_2$ at (A) 325 °C, (B) 340 °C, (C) 350 °C, and (D) 400 °C. 104

Figure 3.5. Experimental series qualitatively estimating nBu$_x$GeH$_{4-x}$ (x = 1, 2, 3) decomposition temperatures (marked by orange ×) in hot injection experiments. nBu$_4$Ge was placed according to ref. 21. The coloured dots indicate the colour of solutions or suspensions obtained at the indicated temperatures. 105

Figure 3.6. Photographs of products (A) **1**, (B) **3**, and (C) **4** obtained from hot injection of (A) nBuGeH$_3$, (B) nBu$_3$GeH, and (C) nBu$_4$Ge in octacosane at 400 °C and dispersed in toluene (prior to workup). **2** was macroscopically comparable to **1** and **3**. 106

Figure 3.7. Transmission electron micrographs of **1** (A, E), **2** (B, F), **3** (C, G), and **4** (D, H), from thermal decomposition of (A, E) *n*BuGeH$_3$, (B, F) *n*Bu$_2$GeH$_2$, (C, G) *n*Bu$_3$GeH, and (D, H) *n*Bu$_4$Ge at 400 °C. The insets in images A-D are selected area electron diffraction (SAED) patterns of **1-4**, respectively. 107

Figure 3.8. Size analysis of aggregated particles observed in TEM imaging of (A) **1**, (B) **2**, and (C) **3**. The analysis is based on measurement of ≥100 particles.....109

Figure 3.9. High-resolution X-ray Photoelectron Spectra of the Ge 3d region for samples **1-3**.....110

Figure 3.10. X-ray powder diffraction patterns of solids **1-3** obtained from hot injection at 400 °C. The yield of **4** was insufficient for XRD. 111

Figure 3.11. Thermogravimetric analysis (TGA) of pure octacosane and samples **1-3** from hot injection at 400 °C. 112

Figure 3.12. Photograph after hot injection in octacosane at 325 °C and 30 min reaction of (A) *n*BuGeH$_3$ (**5**), (B) *n*Bu$_2$GeH$_2$ (**6**), (C) *n*Bu$_2$GeH$_2$ reaction mixture in toluene (**6**), and (D) *n*Bu$_3$GeH reaction mixture in toluene (**7**).....114

Figure 3.13. TEM images of samples **5** (A, D), **6** (B, E), and **7** (C, F) obtained from hot injection of (A, D) *n*BuGeH$_3$, (B, E) *n*Bu$_2$GeH$_2$, (C, F) *n*Bu$_3$GeH in octacosane at 325 °C. 115

Figure 3.14. High-resolution XPS of the Ge 3d region for samples **5-7** synthesized by hot injection in octacosane at 325 °C. The absence of low- oxidation state Ge in **6** and **7** is attributed to exposure to air over a period of one week in contrast to sample **5**, which was only exposed to air for hours, showing the limited oxidative stability of the products. 116

Figure 3.15. Photographs of samples **8** (A), **9** (B), and **10** (C) immediately after hot injection of (A) *n*BuGeH$_3$, (B) *n*Bu$_2$GeH$_2$, (C) *n*Bu$_3$GeH in trioctylamine at 325 °C. 118

Figure 3.16. TEM images of (A) **8**, (B) **9**, and (C) **10** from hot injection of (A) *n*BuGeH$_3$, (B) *n*Bu$_2$GeH$_2$, (C) *n*Bu$_3$GeH in trioctylamine at 325 °C. White arrows indicate the observation of very beam-sensitive material, which is likely trioctylamine impurity. 119

Figure 3.17. XPS of the Ge 3d region for samples **8-10** synthesized by thermal decomposition at 325 °C in trioctylamine. 120

Figure 3.18. Representative Raman spectrum of sample **9**, showing the Ge-Ge phonon around 300 cm^{-1} 120

Figure 4.1. Publications on nanoparticle catalysis from 1995 to 2011, adapted from ref. 1. (SciFinder search "nanoparticle and catalysis", duplicates removed.) 127

Figure 4.2. Homogeneous catalytic mechanisms for (A) Heck and (B) Suzuki couplings, adapted from refs. 22 and 23. 130

Figure 4.3. Remediation capacity of nZVI imparted by the complex formation capacity of the hydroxylated oxide surface and the reductive capacity of the zerovalent iron core, adapted from ref. 28. 133

Figure 4.4. X-ray photoelectron (XP) spectrum of the Pd 3d region for $Fe@Fe_xO_y/Pd$ before (red/solid trace) and after catalysis (blue/dashed trace). The location of the zero-oxidation state fit for the Pd $3d_{5/2}$ signal is shown to illustrate the presence of multiple metal oxidation states. 146

Figure 4.5. Transmission electron microscopy (TEM) images of (A) $Fe@Fe_xO_y$, (B) $Fe@Fe_xO_y/Pd$, and (C) $Fe@Fe_xO_y/Pd$ after catalysis. The scale bars are 100 nm 147

Figure 4.6. X-ray photoelectron (XP) spectrum of the Pd 3d region for $Fe@Fe_xO_y/Pd$ prepared with the maximum (black trace), 2/3 of the maximum (red trace) and 1/3 of the maximum Pd loading (yellow trace). 153

Figure A.1. XRD patterns of **2** processed at increasing temperature for one hour in 5% H_2/95% Ar (left) and 100% Ar atmosphere (right). .179

Figure A.2. XRD patterns of **3** processed at increasing temperature for one hour in 5% H_2/95% Ar (left) and 100% Ar atmosphere (right). .179

Figure A.3. XRD patterns of **4** processed at increasing temperature for one hour in 5% H_2/95% Ar (left) and 100% Ar atmosphere (right). .180

Figure A.4. XRD patterns of **5** processed at increasing temperature for one hour in 5% H_2/95% Ar (left) and 100% Ar atmosphere (right). .180

Figure A.5. X-Ray Photoelectron (XP) spectra of the Ge 3d region of **2** processed at indicated peak temperatures for one hour in 5% H_2/95% Ar (left) or 100% Ar atmosphere (right). 181

Figure A.6. XP spectra of the Ge 3d region of **3** processed at indicated peak temperatures for one hour in 5% H_2/95% Ar (left) or 100% Ar atmosphere (right). 181

Figure A.7. XP spectra of the Ge 3d region of **4** processed at indicated peak temperatures for one hour in 5% H_2/95% Ar (left) or 100% Ar atmosphere (right). 182

Figure A.8. XP spectra of the Ge 3d region of **5** processed at indicated peak temperatures for one hour in 5% H_2/95% Ar (left) or 100% Ar atmosphere (right). 182

Figure A.9. FT-IR spectra of **2** processed at indicated peak temperatures for one hour in 5% H_2/95% Ar (left) or 100% Ar atmosphere (right). 183

Figure A.10. FT-IR spectra of **3** processed at indicated peak temperatures for one hour in 5% H_2/95% Ar (left) or 100% Ar atmosphere (right). 183

Figure A.11. FT-IR spectra of **4** processed at indicated peak temperatures for one hour in 5% H_2/95% Ar (left) or 100% Ar atmosphere (right). 184

Figure A.12. FT-IR spectra of **5** processed at indicated peak temperatures for one hour in 5% H_2/95% Ar (left) or 100% Ar atmosphere (right). 184

Figure B.1. Atomic Force Microscopy (AFM) images of (A) PS-*b*-P4VP (annealed), (B) PS-*b*-P4VP (annealed and processed in air), (C) Thermogravimetric Analysis (TGA) of PS-*b*-P4VP in air, (D) TEOG (annealed and processed in air), (E) PS-*b*-P4VP with TEOG (annealed and processed in air), and (F) X-ray Photoelectron Spectroscopy (XPS) of the Ge 3d region for (E). . 197

Figure B.2. AFM images of (A-B) PS-*b*-PMMA (annealed), (C) PS-*b*-PMMA with TEOG (annealed and processed in air), (D) PS-*b*-P4VP (annealed), (E) PS- *b*-P4VP with TEOG (annealed and processed in air), and (F) TEOG blank (annealed and processed in air). 198

Figure B.3. AFM images of PS-*b*-P4VP/TEOG (0.5 wt%) processed at (A) 400 °C in air, (B) 470 °C in 20% H_2, and (C) 500 °C in 20% H_2. (D) Scanning electron micrograph of PS-*b*-P4VP/TEOG processed at 470 °C in 20% H_2. (E-F) XPS of the Ge 3d region for PS-*b*-P4VP/TEOG processed at (E) 470 °C in 20% H_2, and (F) 500 °C in 20% H_2 200

List of Schemes

Scheme 2.1. Ge-NC synthesis by metathesis of Zintl salts (*e.g.,* NaGe) with tetrachlorogermane, followed by surface functionalization with alkyl Grignard or alkyl lithium reagents. 30

Scheme 2.2. Ge-NC synthesis by reduction of tetrachlorogermane, here showing the followed by surface functionalization with alkyl Grignard or alkyl lithium reagents 31

Scheme 2.3. Thermal decomposition of molecular germanes may form Ge-NCs. 32

Scheme 2.4. Synthesis of mixed-surface Ge-NCs by plasma pyrolysis. 38

Scheme 2.5. Sol-gel synthesis followed by solid-state reduction of GeO_2 nanodomains to Ge-NCs. 39

Scheme 2.6. Formation of Ge-NC/GeO_2 composites from thermolysis of $(RGeO_{1.5})_n$ formed by hydrolysis and condensation of chloride- or alkoxy-substituted molecular precursors. 51

Scheme 2.7. Proposed elimination pathways for R-group cleavage. 60

Scheme 3.1. Band gap energy decrease from benzene to pentacene.[2,3] 82

Scheme 3.2. Pictorial representation of exciton quantum confinement. 82

Scheme 4.1. General Scheme for (A) Heck and (B) Suzuki coupling reactions. 129

Scheme 4.2. (a) Heck and (b) Suzuki coupling reactions investigated here. 148

Scheme 4.3. Trimerization of phenylboronic acid to triphenylboroxin. 150

Scheme B.1. Structural formula of (A) Polystyrene-*block*-poly-4-vinylpyridine (PS-*b*-P4VP) and (B) Polystyrene-*block*-polymethylmethacrylate (PS-*b*-PMMA). 187

Scheme B.2. Examples of block copolymer self-assembly in solution (B-F) and in the solid state (G): (A) Schematic representation of AB-diblock copolymer, (B) vesicle, (C) micelles, (D) inverse micelles, (E) lamellar blocks, (F) cylindrical or tubular micelle, (G) equilibrium morphologies in the solid state (S: spherical, C: cylindrical, G: gyroidal, L: lamellar). Adapted from refs. 20-22. 188

Scheme B.3. Mechanisms of (A) acid- and (B) base-catalyzed sol-gel reaction of Si or Ge alkoxides (adapted from ref. 28). 191

Scheme B.4. Proposed crosslinking mechanism for sol-gel reaction of TEOG in the presence of P4VP and trace water. 199

List of Symbols, Nomenclature and Abbreviations

°C	degree Celsius
1D	one-dimensional
2D	two-dimensional
3D	three-dimensional
Å	Ångstrom (= 0.1 nm)
a	lattice constant
a_B	Bohr exciton radius
AFM	atomic force microscopy
AO	atomic orbital
BCP	block copolymer
CB	conduction band
cm^{-1}	wavenumber
CMOS	complementary metal-oxide semiconductor
CNT	classical nucleation theory
d	diameter
DMF	dimethylformamide
e	electron charge
E	energy
e^-	electron
EA	elemental analysis
EDX, EDS	energy-dispersive X-ray spectroscopy
E_F	Fermi level
E_g	band gap
EMA	effective mass approximation
EN	electronegativity
eV	electronvolt
$Fe@Fe_xO_y$	iron-iron oxide core-shell nanoparticles
FS	freestanding
FT-IR	Fourier-transform infrared spectroscopy
GC-MS	gas chromatography coupled with mass spectrometry

GRO	germanium-rich oxide
h	hour
$\hbar$	reduced Planck constant
h^+	hole
HOMO	highest occupied molecular orbital
HRTEM	high-resolution transmission electron microscopy
HSQ	hydrogen silsesquioxane
ICP-MS	inductively coupled plasma mass spectrometry
IPA	isopropyl alcohol
IR	infrared
K	Kelvin
k	momentum vector
kJ	kilojoule
kV	kilovolt
LCAO	linear combination of atomic orbitals
LUMO	lowest occupied molecular orbital
M	metal
m_0	electron rest mass
MALDI	matrix assisted laser desorption ionization
m_e	effective mass of an electron
mg	milligrams
m_h	effective mass of a hole
min	minute(s)
mL	millilitres
mmol	millimole
MO	molecular orbital
MS	mass spectrometry
N_A	Avogadro's number, 1.662×10^{19}
NC	nanocrystal
nm	nanometer
NP	nanoparticle

nZVI	nanoscale zerovalent iron
Pd/C	palladium on carbon
PL	photoluminescence
pm	picometer
ppm	parts per million
PZC	point of zero charge
r	radius
SAED	selected area electron diffraction
SEM	scanning electron microscopy
STM	scanning tunelling microscopy
T	temperature
TEM	transmission electron microscopy
TEOG	tetraethoxygermane
TEOS	tetraethoxysilane
TGA	thermogravimetric analysis
TOA	trioctylamine
TOF	turnover frequency
TON	turnover number
VB	valence band
XP	X-ray photoelectron
XPS	X-ray photoelectron spectroscopy
XRD	X-ray diffraction
Δ	difference
δ	resolution limit
κ, k	static dielectric constant
λ	wavelength
μ	reduced mass
μm	micrometer
μmol	micromole

Chapter 1:

Introduction

1.1. An Introduction to Nanoscience

Nanomaterials are generally defined to be materials that have at least one dimension in the size range of 1-100 nm. Restricting dimensions allows the formation of different materials such as nanosheets or –films, with thicknesses below 100 nm (1D), nanowires, with diameters below 100 nm (2D), and nanoparticles, or nanoclusters, both referring to particles with all three dimensions below 100 nm.[1]

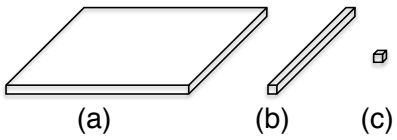

Figure 1.1. Nanomaterials confined in (a) one, (b) two and (c) three dimensions.

The origin of the prefix "nano" is the Greek word νανος meaning "dwarf".[2] How does the size of a nanoparticle compare to everyday items we can relate to? If we compare the size of a 3-4 nm nanoparticle to a European football, the scale between the two is of the same order of magnitude as comparing said football to the size of the Earth – one of the reasons it is challenging to truly comprehend the minute structures that are the subject of nanoscience (Figure 1.2). Examples of other things that exist at the size scale of the nanoparticles discussed in this thesis include the human immunodeficiency virus (HIV) and the width of a double-stranded helix of DNA, our genetic material.[3]

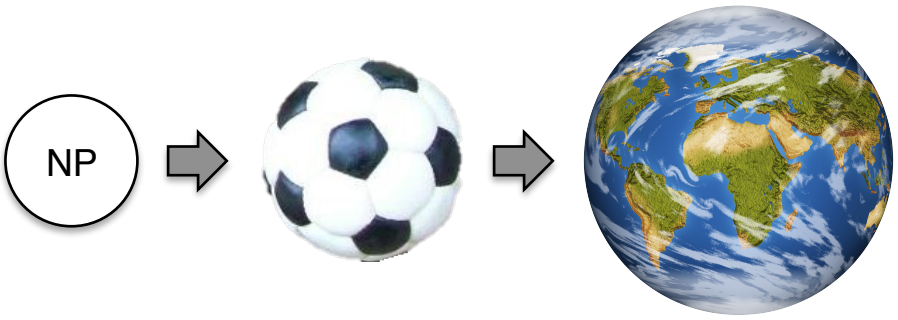

Figure 1.2. When relating the size of a 3-4 nm nanoparticle to a football the scale-up compares to relating a football to the size of the Earth.[4,5]

Nanotechnology is often perceived as a relatively recent phenomenon, with the term coined in 1974 by Norio Taniguchi, a physicist at Tokyo Science University.[6] However, as many researchers insist, nanochemistry is not at all that recent, previously it was simply referred to as colloid chemistry (colloids being dispersions of matter with at least one dimension of 1 nm – 1 μm).[7] Our understanding of nanomaterials has only really started to advance since the mid-20th century, but nanoparticles have unknowingly been used in a number of applications since the Roman Period. A famed example from this period is the Lycurgus Cup (4th century AD), which is in exhibit at the British Museum in London (Figure 1.3). The cup is made of dichroic glass, with intriguing optical properties that are imparted to it by the presence of nanoparticles of gold and silver. Their presence stains the glass green (reflected light), though it appears red when illuminated from within (transmitted light).[8] Nanoparticles are found in similar applications throughout the ages, causing the ruby red (gold NPs) and deep yellow (silver NPs) colours of stained glass windows from the Medieval Period (500-1450), the beautiful iridescent or metallic glazes (copper and silver

NPs) applied by the Deruta Ceramicists of Umbria during the Renaissance Period (1450-1600), and a popular purple dye known as The Purple of Cassius (gold NPs and tin hydroxide).[9,10] Silver NPs were also fundamental to the development of photography, with Joseph Niepce's discovery of the light-mediated decomposition of silver halides to nanoparticles in 1827 yielding the pigments of black-and-white photography.[9] Recipes for the production of nanoparticles were first documented by Antonio Neri, an Italian glass maker, in his glass-making manual *L'Arte Vetraria* (The Art of Glass) in 1612, and in Andreas Cassius' 1685 description of Purple of Cassius synthesis, though both documents do not suggest they are aware of the nature of their products.[10]

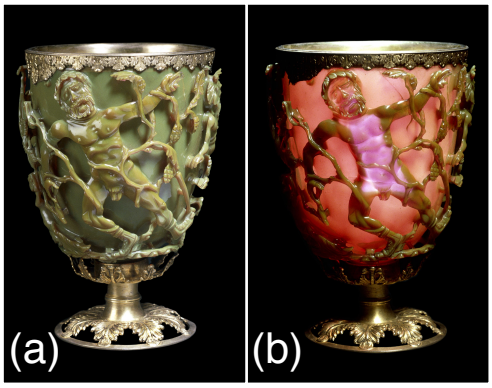

Figure 1.3. The Lycurgus cup, (a) in reflected light, (b) in transmitted light, (both © Trustees of the British Museum, reproduced with permission).

A more systematic study of colloids and their properties started with Michael Faraday's synthesis of colloidal gold solutions, which are still in exhibit at the Royal Institute in London, England. In 1857, he presented his findings on

thin metal films and "finely divided metal" in the Bakerian Lecture, an annual prize lecture of the Royal Society.[11] At this point, researchers were already aware that different colours could be obtained from different species of gold – as we would understand much later, the observed colour can be controlled based on the gold nanocrystal size. The understanding of colloids slowly grew, continued by Albert Einstein's connection of nanoparticle Brownian motion with their diffusion coefficient, and Gustav Mie's development of Mie theory.[12,13] Mie theory is a mathematical solution of the Maxwell equations for the interaction of electromagnetic radiation (light) with a sphere (the metal nanoparticle). It relates the size to the scattering of certain wavelengths, shorter wavelengths being scattered the most.

From here on, it still took decades for nanoscience to develop into what it is today – a burgeoning field of research and development. Importantly, the advent of imaging techniques capable of "opening our eyes" to the nanodomain, and even beyond, to the ability of "seeing" atoms, enabled this boom. The imaging of nanomaterials is challenging because their sizes are a few orders of magnitude smaller than the wavelength of light - which at 400 – 700 nm determines the resolution limit δ of light microscopy ($\delta \approx \lambda/2 \approx 200$ nm).[14] The first imaging technique that was able to break through the resolution limit of visible light made use of the wave-particle duality described in quantum mechanical theory by Albert Einstein (Photoelectric Effect: particle nature of light) and Louis de Broglie (any moving particle has an associated wave).[15,16] Following this theory, Ernst Ruska at the University of Berlin first demonstrated

electron microscopy in 1931.[17,18] Electrons of a certain speed (*i.e.*, accelerating voltage) are effectively light of a very short wavelength, and can be used to image features on the nanoscale. For example, the 200 kV transmission electron microscope (TEM) used for the work presented in this thesis produces an electron beam with a wavelength of about 2.5 pm.[14] TEM images can be thought of as a silhouette of the material inserted into the beam, where contrast is based on scattering of the electron beam. Next to imaging, a variety of other interactions of the sample with the electron beam are of analytical value. Auger electrons and X-rays emitted from the sample can be used for elemental analysis, electron diffraction for crystal analysis, and so forth. A diagram representing these interactions is shown in Figure 1.4.

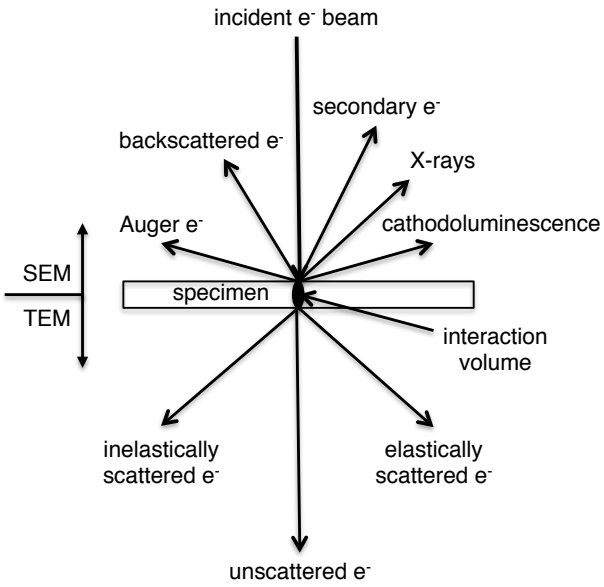

Figure 1.4. Diagram of interactions in electron microscopy, adapted from ref. 14.

Further important developments were made in the 1980s, when imaging and manipulation of atoms became possible. Scanning tunnelling microscopy (STM), developed in 1981 by Swiss scientists Gerd Binnig and Heinrich Rohrer at IBM, has the ability to image individual atoms on a surface.[19] To achieve this, an atomically sharp conducting tip (*i.e.*, it ends in a single atom) is brought close enough to a surface that electrons can tunnel from the surface to the tip, or the tip to the surface (Figure 1.5.a). This produces a current that is sensitive to changes in the electronic structure of the sample, and can thus be converted into an image of the electronic structure (Figure 1.5.d). Donald M. Eigler and Erhard K. Schweizer, of IBM in San José, later showed that the STM could also be used to move atoms into specific locations, which generated a lot of excitement as the first demonstration of controlled manipulation on the atomic scale (Figure 1.5.b).[20]

Binnig was also involved in the development of atomic force microscopy (AFM) with Christoph Gerber, again at IBM Zürich.[21] Here, an atomically sharp tip is brought into physical contact with the surface, and is dragged or tapped across the sample (Figure 1.5.a). The inflection of the cantilever on which the tip is mounted is followed by means of a laser and provides topographic information of the surface (Figure 1.5.e), but can also be modified to give chemical or electronic information.[21-23]

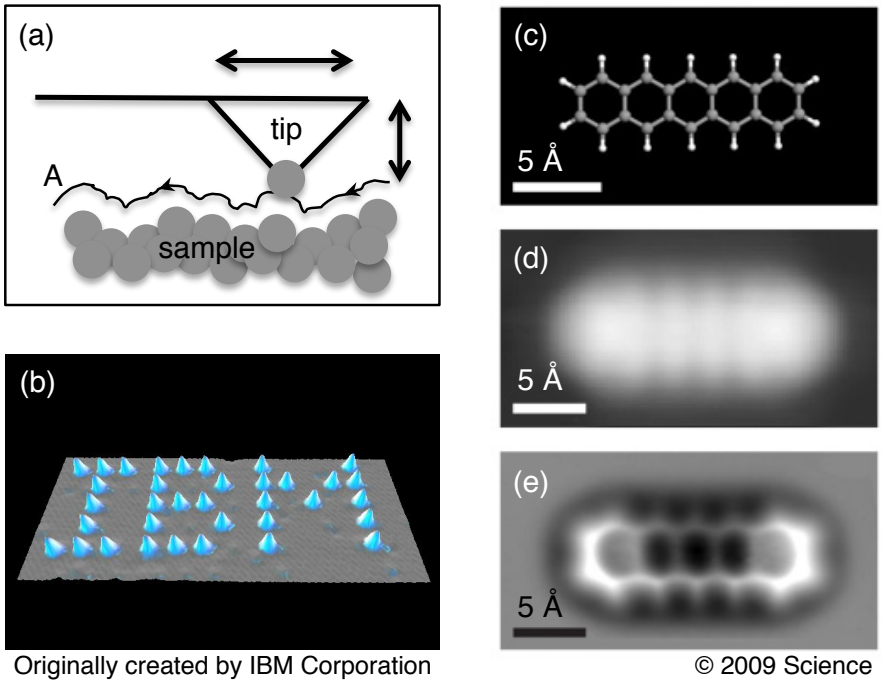

Figure 1.5. (a) The principle of STM and AFM is to probe the contour of a surface with an atomically sharp tip that is moved at a distance to the surface to maintain a constant tunnelling current (STM) or a constant force (AFM) (adapted from ref. 21). Examples of images are shown in (b)-(e): Xenon atoms manipulated by STM on a Ni (110) surface,[24] (c) ball-and-stick model of pentacene, (d) STM image of pentacene, (e) AFM image of pentacene, recorded with a CO-terminated tip.[25] Images (c)-(e) adapted from ref. 25.

With many powerful analytical tools at hand, researchers have deepened our understanding of processes at the nanoscale and developed synthetic methods for a vast variety of nanostructures – in terms of sizes and shapes as well as chemical composition. In the following section, an introduction to the properties of nanoparticles will be given, to answer the question why these materials are of such interest.

1.2. How Nano is Different – Size-Dependent Properties

Now, what makes nanomaterials so fascinating? We have already seen that their colour will differ from the appearance of the bulk material, indicating changes in their electronic and optical properties. At the nanoscale, we observe luminescence from materials such as silicon, which does not luminesce in the bulk. We observe drastic decreases in melting points, increases in reactivity, and changes in magnetic properties.[26,27] All these changes are linked to the intermediate size of nanomaterials in the range between molecules and extended bulk materials. Within the consequences of this size regime, the key effects that drive the research presented in this thesis are the surface area and electronic and optical properties of nanomaterials.

1.2.1. The Importance of the Surface

Since nanoparticles contain a relatively small number of atoms, an increasingly large proportion of atoms reside at the surface as particle size decreases. The increased surface area and resulting influence of surface properties is responsible for a range of property changes that are observed at the nanoscale, including melting point depression and increased reactivity.

Surfaces have higher free energy due to the lower coordination of surface atoms in comparison with atoms in the bulk.[28] As the contribution of surface energy to the overall energy of the system becomes more significant with decreasing size, the liquid state becomes increasingly energetically favourable. In the liquid state, surface atoms are mobile and can rearrange to minimize surface energy, while they are locked into position in the solid state.[28] This effect

decreases the melting point exponentially with decreasing size for very small nanoparticles.[26]

The increased surface area also implies that more of a given material is available for surface-mediated reactions, leading to substantial improvements in activity of nanoscale materials towards heterogeneous catalysis (in particular when the surface reaction is the rate-limiting step).[29,30] Among surface atoms, defect sites such as step edges, corners and kinks have a range of lower coordination numbers than atoms on planes, increasing their reactivity.[28,30-32] The proportion of these sites increases with decreasing size, contributing a second factor to improved catalytic properties.[30] We explore the application of this effect in Chapter Four. The importance of various factors influencing catalytic activity and selectivity differs with the type of catalyzed reaction, but other factors that have been identified include the nature of support materials, chemical composition of the catalyst, and presence of stabilizers, to name a few.[29,31,33] Catalysis remains a field of intense research efforts with many fundamental mechanistic questions to answer.

1.2.2. The Effect of Size on Magnetic Properties

An interesting phenomenon that has been observed in nanoparticles of magnetic materials (Fe, Co, Ni, their (mixed) oxides and alloys) is superparamagnetism. Below a critical size (tens of nanometers, material dependent), the particles consist of a single magnetic domain.[27] Above a critical temperature, the blocking temperature, these particles exhibit superparamagnetic behaviour: they no longer display individual atomic magnetic moments, but act as

one big paramagnet with up to 10^4 times larger magnetic moment than a bulk paramagnetic material.[27,34] The magnetic moments also randomize quickly, leading to no magnetic moment in the absence of a magnetic field.[27] Among others, this aids colloidal stability of magnetic nanoparticles and is useful in view of their potential biological applications.[34] Magnetic nanoparticles show promise for a broad range of applications, ranging from catalyst supports[35-37] to contrast agents for magnetic resonance imaging (MRI), hyperthermal therapy agents, and magnetic drug delivery.[34]

Iron-iron oxide core-shell nanoparticles ($Fe@Fe_xO_y$), also known as nanoscale zerovalent iron (nZVI), offer remarkable reductive capabilities in addition to their magnetic characteristics. In this context, nZVI is a well-studied environmental remediation agent. Facilitated by the low standard reduction potential of iron, nZVI reductively degrades halogenated organic compounds, and removes metal ions through adsorption onto the hydroxylated surface followed by reduction.[38-40] The promise of magnetic recoverability and their ability to reduce metals onto their surface drew us to investigate $Fe@Fe_xO_y$ as catalyst supports (see Chapter 4), however, we observed substantially degraded magnetic properties upon metal deposition.[41-43]

1.2.3. Optical and Electronic Properties at the Nanoscale

The other key change in properties at the nanoscale is the observation that, even though the structure of nanomaterials is often equivalent to that of the bulk, their electronic and optical properties are different. Thus, nanoscale gold and silver are not gold and silver in colour, but rather exhibit a variety of colours

depending on their size and shape.[8] Nanoscale semiconductors emit visible light in notable intensities, the wavelength of which can again be tuned with nanocrystal size.[44,45] Since the structure is the same, and bonding dictates the electronic properties, how do these observed differences arise? We will consider first the relationship of bonding with electronic and optical properties in molecules and bulk solids, before examining in more detail the causes of nanomaterial optical and electronic properties.

1.2.3.1. Molecules

Bonding in organic molecules is predominantly covalent. In ideal covalent bonds, electron density is shared between atoms by favourable overlap of singly occupied atomic orbitals of appropriate symmetry. Mathematically, the bonding can be described by solving the Schrödinger equation for the molecule. A good approximation of the result is given by linear combination of atomic orbitals (LCAO). In LCAO, atomic orbitals are combined to yield the same overall number of molecular orbitals (MOs) (Figure 1.6). If the overlapping portions of AO wave functions are in phase, a bonding interaction results, and the MO is lowered in energy. If they are out of phase, an antibonding interaction results, and the MO is increased in energy relative to the original AOs. The energy by which bonding and antibonding MOs split depends directly on the extent of overlap between the AOs. If there is a high degree of overlap, a strong bond is formed and the splitting energy is high. If there is however only a low degree of overlap, the bonding is weak and the splitting energy is low. The resulting MO diagram is populated with electrons according to the Aufbau and Pauli principles, and

Hund's rule. The energy gap between the highest occupied MO (HOMO) and the lowest unoccupied MO (LUMO) is the band gap, which corresponds to the lowest energy at which electronic and optical transitions are observed.[46]

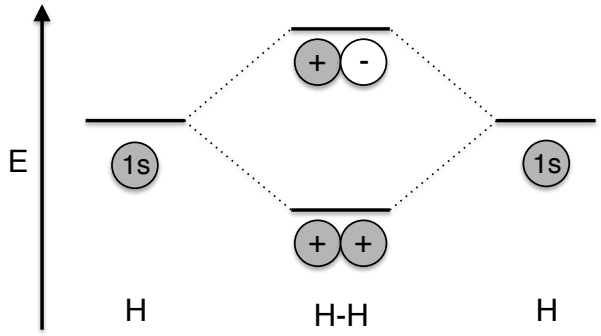

Figure 1.6. Molecular orbital diagram of dihydrogen: The 1s orbitals of two hydrogen atoms, shown at the left and right hand side, combine to form bonding (lowered in energy) and antibonding molecular orbitals (raised in energy) in the molecule H_2, shown at the centre.

1.2.3.2. Bulk Solids

1.2.3.2.a. Structure and Bonding Types

The structures of solids can be divided into two broad areas based on their ordering: crystalline and amorphous solids. Crystalline solids exhibit structural order over a long range with all atoms having defined locations in the periodic crystal lattice. The translational symmetry of a crystal lattice is defined by its smallest building block, the unit cell. In amorphous solids, no long-range order is present.[47] Crystalline and amorphous materials may be differentiated between by

techniques such as X-ray diffraction (XRD), in which crystalline solids will give sharp reflections while amorphous materials have an extremely broad, featureless signature.

Solids can also be classified according to their bonding. Of interest in the context of this work are ionic, network covalent and metallic solids; molecular solids will not be discussed. A bond may be formed when atoms approach one another and their orbitals overlap. Depending on the difference in electronegativity (EN) between the approaching atoms, the electrons may be transferred from one atom to another, forming positively and negatively charged ions. Non-directional electrostatic forces attract the ions to each other, constituting ionic bonds. The magnitude of the electronegativity difference (ΔEN) dictates the polarization of bonds from the extreme of complete electron transfer in ionic bonding (large ΔEN) to the other extreme, covalent bonding (small ΔEN). In a true covalent bond, electron density is shared equally between atoms. Here, the geometry of the overlapping orbitals localizes the bonding electrons between nuclei, giving the bonding directionality and a defined space, in contrast to the non-directional ionic bonds. In intermediate cases, polar covalent bonds are polarized towards the more electronegative element. Metallic bonding is different again, the valence electrons are now not associated with any particular atom. Instead, they are fully delocalized across a close-packed array of non-directionally bonded atoms.[47] Iron oxides are examples of mostly ionic compounds, while germanium is a covalent solid.

1.2.3.2.b. The Bulk "MO Diagram": Band Structures

Bonding in the extended solid can be evaluated with similar tools as used for molecules above. LCAOs become more complex, and thus are evaluated in more detail for specific points of interest (characteristic points within the Brillouin zone, *vide infra*).[48] Using the terminology of solid-state physics, LCAOs are termed Bloch functions and represent the basis of the band structure, the bulk "MO diagram". The band structure arises from the combination of a large number of discrete energy levels in an extended solid, based on the contribution of energy levels from ~N_A (Avogadro's number, 6.022×10^{23}) atoms or unit cells making up the bulk solid. The large number of discrete energy levels is thus approximated as a continuous band (Figure 1.7).[48]

The band structure of a solid describes the allowed energy states of an electron as a function of the magnitude of the electron's momentum (k: wavevector or momentum vector), which is inversely proportional to its wavelength.[49] In a three-dimensional crystal lattice, the energy of the electron is direction dependant and can be approximated by considering the electron placed in a periodic potential. According to Bloch's theorem, waves travelling through a crystal lattice will undergo constructive interference when the wavelength is proportional to the lattice spacing.[49] The points at which constructive interference is observed are periodic and constructs what is commonly known as a reciprocal lattice in reciprocal or momentum space. The volume in momentum space within the limits $0 < |k| < \pi/a$, a being the lattice constant, contains all unique values of k. It has different dimensions than the crystal unit cell, but is conceptually

comparable: It is the smallest repeat unit of electronic energy states in momentum space, and is known as the Brillouin zone. The energy versus wavevector diagram (Figure 1.7) shows how the energy of the electron changes, based on its direction of travel through the crystal lattice, as a function of the magnitude of its momentum. The direction of travel is given between characteristic points within the Brillouin zone (*e.g.,* Γ - centre of the zone, Roman letters (M, X, L, *etc.*): centres of different faces) and corresponds to the equivalent direction of travel through the crystal lattice in real space.[49] Analogous to MO diagrams, the lower energy part of a band is bonding, while the high-energy part of a band is antibonding. Also, the dispersion of the band (effectively the energy separation between maximum bonding and maximum antibonding states) is proportional to the degree of orbital overlap, *i.e.*, to the strength of bonding, analogous to the dependence of bonding and antibonding MO energy splitting on bond strength.[48]

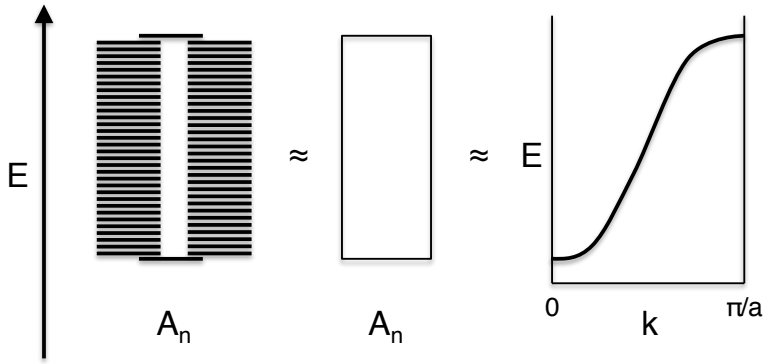

Figure 1.7. Bands are depicted as continuous due to the extremely close spacing of ~N_A energy states in a solid A_n. To describe the band structure in more detail, the band can be deconvoluted into energy states as a function of the momentum vector k. The band shown on the right is representative of an s-orbital overlap.[48]

A consequence of band structures is there are no substantial energy gaps between electronic states within a band; there is instead an apparent continuum of states (Figure 1.7). Bands can be separated by energy gaps, can overlap with one another, and can be only partially filled, which influences electron mobility (conductivity) in the solid. The highest state or energy level that is occupied at 0 K is referred to as the Fermi level, E_F. The Fermi level lies within or at the top of the valence band, while the unoccupied band immediately above in energy is referred to as the conduction band. In metals, valence and conduction bands overlap or bands are only partially filled, and thermal energy is sufficient to fully delocalize electrons throughout the solid. In semiconductors, valence and conduction bands are separated by a band gap of ~1-4 eV. Here, the Fermi level lies within the band gap, and is a measure of the ease with which electrons are promoted across the band gap to the conduction band. At room temperature, thermal energy is sufficient to promote a small number of electrons across the band gap into the conduction band, causing the material to have limited conductivity. In the case in which the band gap is larger than ~4 eV, the material is no longer electrically conductive at room temperature – these materials are generally referred to as insulators.[47,48]

An important factor in light emission, and thus in excitation and relaxation of electrons across the band gap in semiconductors, is the relative location of conduction band minima and valence band maxima in reciprocal space. In direct band gap semiconductors, such as CdSe, the lowest conduction band minimum is at the same point in reciprocal space as the highest valence band maximum

(Figure 1.8.a). Conservation of electron spin and momentum are respected in any electronic transition. In indirect band gap semiconductors, prominent examples being Si and Ge, the conduction band minimum and valence band maximum are located at different points in reciprocal space. For an electron to move across the band gap, excitation and relaxation have to be accompanied by a phonon (a lattice vibration) (Figure 1.8.b).[47]

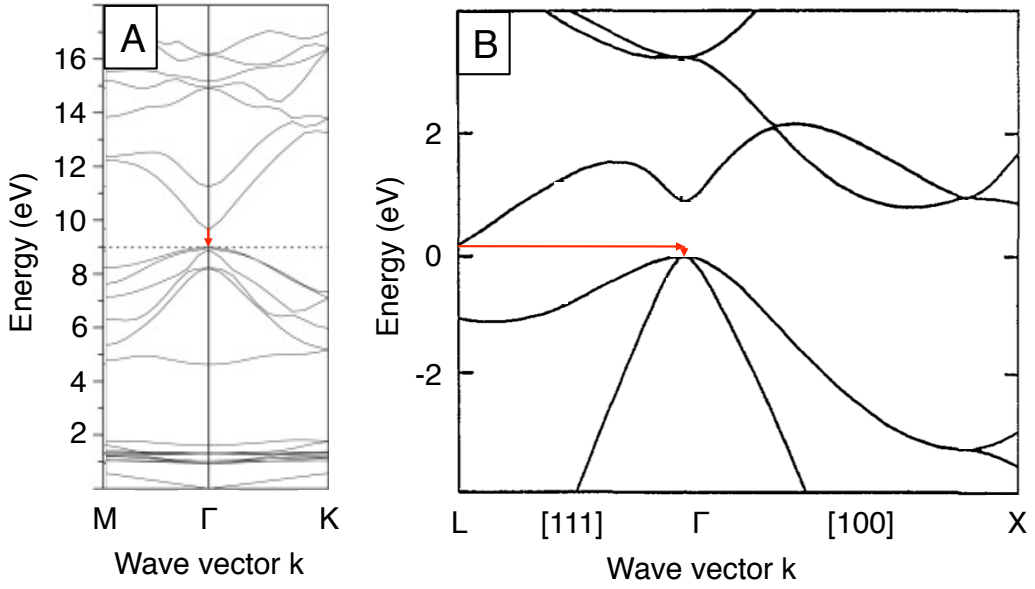

Figure 1.8. Band structures between certain points in the Brillouin zone (BZ) (Γ = centre of BZ; hexagonal crystal lattice: M = centre of a rectangular face, K = edge between two rectangular faces; face-centered cubic crystal lattice: L = centre of a hexagonal face, X = centre of a square face, [111] and [100] indicate the direction of electron travel that is represented going out from the zone centre in two directions) of (A) CdSe and (B) Ge, showing the respective direct and indirect band gap (transition marked by red arrows). Adapted from ref. 54 and 55.

This additional requirement makes excitation and relaxation less likely, and causes excited states to have longer lifetimes. The long-lived excited state is more susceptible to alternative, non-radiative relaxation pathways, quenching photoluminescence in the bulk material at room temperature. The observation of photoluminescence in nanomaterials of Si and Ge is attributed to the spatial confinement of the exciton as well as a reduction in non-radiative pathways.[50-53] The spatial confinement of the exciton increases the electron-hole interaction and thereby increases the rate of recombination in comparison to the bulk materials.[52] The small size of nanocrystals further reduces the effect of non-radiative recombination pathways. Non-radiative decay can occur at dopant atoms, lattice and surface defects (*e.g.*, dangling bonds), as well as through mechanisms such as Auger recombination, and interfacial energy or charge transfers.[50,51] In bulk materials, charge carriers scatter over macroscopic length scales due to the long-lived excited state, and are easily deactivated by a low density of defect traps. In surface-passivated nanocrystals, Auger recombination is slowed due to the isolation of electron-hole pairs in separate crystals, while defects can only quench excitons formed in the same crystal, leading to observable photoluminescence from nanocrystalline Group 14 semiconductors.[51]

1.2.3.3. Optical and Electronic Quantum Size Effects

The historic examples of stained glass and brightly coloured solutions exemplify the observed change in noble metal optical properties with size (*vide supra*).[8,11] The extensively delocalized electrons in metals (often referred to as a 'sea of electrons') are susceptible to polarization by the electric field of

electromagnetic radiation (*i.e.,* light), leading to collective electron oscillation. This plasmon oscillation lies in the visible wavelength region for nanoscale Au, Ag, and other metals, causing brightly coloured nanoparticle solutions (*vide supra*).[8,56] In semiconductors such as CdSe and Si, we observe size-dependent emission of light from nanoscale materials.[44,45] In these cases, quantum confinement can be responsible for the observed changes in optical properties. In the quantum confinement regime, properties are dictated by quantum mechanics. Discrete energy levels and a reduction in the number of AOs contributing to the formation of conduction and valence bands lead to thinning that is most noticeable at the band edges (Figure 1.9).[28] Thus, the band gap energy increases with decreasing nanocrystal size.

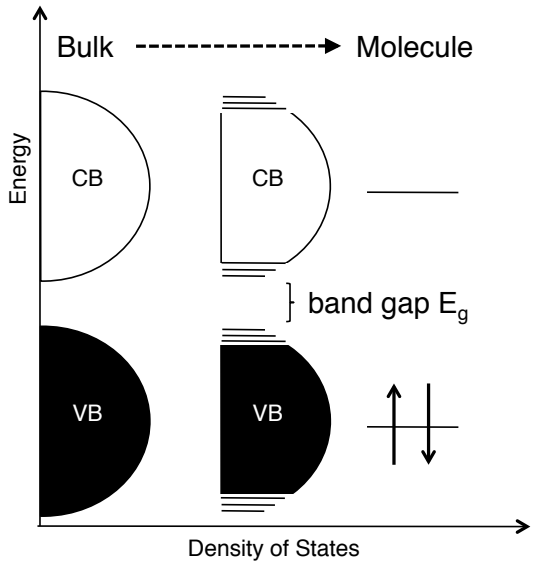

Figure 1.9. The band gap between valence band (VB) and conduction band (CB) increases with decreasing crystal size.

Upon excitation into the conduction band, an electron leaves behind a corresponding hole (or "absence of an electron", with properties equivalent to that of an electron except for its positive charge) in the valence band.[57] This electron-hole pair is bound by Coulomb forces and forms a quasiparticle known as an exciton. A measure of the physical separation of the electron and corresponding hole is given by the Bohr exciton radius, a_B:

$$a_B = \frac{\kappa \hbar^2}{\mu e^2}, \quad \frac{1}{\mu} = \frac{1}{m_e} + \frac{1}{m_h} \qquad (1.1)$$

In equation 1.1, κ is the static dielectric constant (also referred to as the relative permittivity ε_r), $\hbar$ is the reduced Planck constant, e the charge of an electron, and μ the reduced mass, which is calculated from the effective masses of electron (m_e) and hole (m_h) at their respective locations in reciprocal space. Quantum confinement is evident at crystal sizes below the Bohr exciton radius. In Ge, the Bohr exciton radius is calculated as 24.3 nm for a static dielectric constant κ of 15.8, and lightest electron and hole effective masses of $0.082m_0$ and $0.043m_0$.[57,58] This is large in comparison to Si (4.9 nm)[50] and CdSe (3 nm)[59], suggesting that quantum confinement effects will be observed at substantially larger crystal sizes for Ge.

1. 3. Scope of this Thesis

The work presented in this thesis has two main foci. It is aimed at increasing our understanding of the processes underlying Ge-NC synthesis and investigating new ways to eventually achieve materials with well-defined optical and electronic properties. Further, it examines the catalytic activity of iron/iron oxide nanoparticles with metals reduced onto their surface by electroless deposition. More detailed introductions to these topics are included in each chapter.

A major part of this work is focused at deepening the understanding of the factors influencing Ge-NC formation in a solid-state synthesis. Our group has previously shown that Ge-NCs can be formed within a germanium oxide matrix through sol-gel polymerization of $PhGeCl_3$ followed by thermal decomposition of the polymer.[60,61] We were interested to know the exact role of the phenyl group in this synthesis, and set out to investigate if we could change our resulting materials by using different organic substituents.[62] Chapter Two details the investigation of a range of organic substituents in $(RGeO_{1.5})_n$. The choice of substituent was found to induce changes in Ge-NC formation temperatures and in (undesirable) C incorporation into the final product, among others. We propose this arises from increased options for R-group elimination in structurally different substituents. Plausible mechanisms include the originally suggested radical cleavage and, for a number of the investigated groups, β-hydride elimination. Complete data sets for all substituents are presented in Appendix A.

The n-butyl substituted sol-gel product yielded the lowest Ge-NC formation temperature, which lead us to transfer this substituent into a molecular environment and investigate Ge-NC synthesis from decomposition of $n\mathrm{Bu}_x\mathrm{GeH}_{4-x}$ (x = 1-4). Of particular interest in this study, which is discussed in Chapter Three, is the influence of the hydride substituents on thermal decomposition. Our results show that the decomposition temperature decreases with increasing number of hydride substituents. In extension of our hypothesis formed in Chapter Two (the temperature of decomposition is lowered when more, and energetically more favourable, decomposition pathways become available) we suggest the hydride substituent facilitates reductive elimination as a third mechanism, lowering the energy needed for decomposition. The differences in decomposition temperatures are also reflected in products obtained from hot injection at 400 °C. In our setup, this temperature was unable to generate crystalline Ge. The lack of crystallinity excluded a detailed study of the optical properties, since a well-defined electronic structure is only to be expected from a well-defined, crystalline physical structure.

In Chapter Four, metal decorated iron/iron-oxide core-shell nanoparticles ($\mathrm{M/Fe@Fe_xO_y}$) are tested as low-cost catalysts with facile synthesis and good recoverability. The particles are produced by spontaneous electroless deposition of metal salts on $\mathrm{Fe@Fe_xO_y}$, which are obtained by borohydride reduction of iron (III) chloride solutions. Hypothetically, these materials should be able to reduced the amount of metal used, since small islands or shells of metal are formed on $\mathrm{Fe@Fe_xO_y}$, and a large proportion of the metal atoms will thus be on the surface. They also show reduced leaching of catalytic metal into the final product, due to

the reducing ability of the support material. After reaction, the solvated metal is redeposited on the support. However, under the conditions tested, these materials showed only relatively poor activity in Heck coupling reactions, but good activity towards Suzuki couplings in a mixture of ethanol and water in air.

Chapter Five summarizes the results of the investigations regarding Ge-NC synthesis and the study of metal-decorated $Fe@Fe_xO_y$ as catalysts for C-C bond formation. Research directions worth pursuing in these areas in the future are discussed in detail.

1.4. References

(1) Milmo, S. EU proposes nanomaterial definition http://www.rsc.org/chemistryworld/News/2011/October/21101101.asp (accessed Jun. 2012).
(2) Dictionary definition of nano http://www.encyclopedia.com/doc/1O13-nano.html (accessed Jun. 2012).
(3) Scale of the Universe http://scaleofuniverse.com (accessed Jun. 2012).
(4) Football (ball) - Wikipedia, the free encyclopedia http://en.wikipedia.org/wiki/Football_(ball)#Dimensions (accessed Jun. 2012).
(5) Diameter of Earth http://www.universetoday.com/13860/guide-to-space/ (accessed Jun. 2012).
(6) Taniguchi, N. *Proc. Intl. Conf. Prod. Eng. Tokyo, Part II, Japan Society* **1974**.
(7) *IUPAC Compendium of Chemical Terminology*; Nič, M.; Jirát, J.; Košata, B.; Jenkins, A.; McNaught, A., Eds. 2nd ed. IUPAC: Research Triagle Park, NC, 2009.
(8) Liz-Marzan, L. M. *Mater. Today* **2004**, 26–31.
(9) History of Nano http://www.discovernano.northwestern.edu/whatis/History (accessed Jun. 2012).
(10) Hunt, L. B. *Endeavour* **1981**, *5*, 61–67.
(11) Faraday, M. *Phil. Trans. R. Soc.* **1857**, *147*, 145–181.
(12) Einstein, A. *Ann. Phys.* **1905**, *322*, 549–560.
(13) Mie, G. *Ann. Phys.* **1908**, *330*, 377–445.
(14) Williams, D. B.; Carter, C. B. In *Transmission Electron Microscopy*; Springer US: Boston, MA, 2009; pp. 3–22.
(15) Einstein, A. *Ann. Phys.* **1905**, *322*, 132–148.
(16) de Broglie, L. In *Nobel Lectures Physics, 1922-1941*; Elsevier Publishing Company: Amsterdam, 1965.
(17) Knoll, M.; Ruska, E. *Ann. Phys.* **1932**, *404*, 607–640.
(18) Knoll, M.; Ruska, E. *Ann. Phys.* **1932**, *404*, 641–661.
(19) Binnig, G.; Rohrer, H.; Gerber, C.; Weibel, E. *Appl. Phys. Lett.* **1982**, *40*, 178–180.
(20) Eigler, D. M.; Schweizer, E. K. *Nature* **1990**, *344*, 524–526.
(21) Binnig, G.; Quate, C. F.; Gerber, C. *Phys. Rev. Lett.* **1986**, *56*, 930–933.
(22) Gacem, K.; El Hdiy, A.; Troyon, M.; Berbezier, I.; Ronda, A. *Nanotechnology* **2010**, *21*, 065706.
(23) Barattin, R.; Voyer, N. *Chemical Communications* **2008**, 1513–1532.
(24) *almaden.ibm.com*.
(25) Borman, S. *Chem. Eng. News* **2009**, *87*, 6.
(26) *Nanoscale Materials in Chemistry*; Klabunde, K. J., Ed. Wiley-Interscience: New York, USA, 2001.
(27) Lu, A.-H.; Salabas, E. L.; Schüth, F. *Angew. Chem. Int. Ed.* **2007**, *46*,

1222–1244.
(28) Alivisatos, A. P. *J. Phys. Chem.* **1996**, *3654*, 13226–13239.
(29) Ross, J. R. H. *Heterogeneous Catalysis*; Elsevier: Amsterdam, 2012.
(30) *Nanoscale Materials in Chemistry (2nd Edition)*; Klabunde, K. J.; Richards, R. M., Eds. 2nd ed. Wiley-Interscience: Hoboken, NJ, USA, 2009.
(31) *Selective Nanocatalysts and Nanoscience*; Wiley-VCH Verlag GmbH & Co. KGaA: Weinheim, Germany, 2011.
(32) Reetz, M. T.; Westermann, E. *Angew. Chem. Int. Ed.* **2000**, *39*, 165–168.
(33) Cuenya, B. R. *Thin Solid Films* **2010**, *518*, 3127–3150.
(34) Colombo, M.; Carregal-Romero, S.; Casula, M. F.; Gutiérrez, L.; Morales, M. P.; Böhm, I. B.; Heverhagen, J. T.; Prosperi, D.; Parak, W. J. *Chem. Soc. Rev.* **2012**, *41*, 4306–4334.
(35) Zhu, Y.; Stubbs, P.; Ho, F.; Liu, R.; Ship, P. *Chem. Cat. Chem.* **2010**, *2*, 365–374.
(36) Polshettiwar, V.; Luque, R.; Fihri, A.; Zhu, H.; Bouhrara, M.; Basset, J.-M. *Chem. Rev.* **2011**, *111*, 3036–3075.
(37) Shylesh, S.; Schünemann, V.; Thiel, W. R. *Angew. Chem. Int. Ed.* **2010**, *49*, 3428–3459.
(38) Li, X.-Q.; Elliott, D.; Zhang, W.-X. *Crit. Rev. Solid State Mater. Sci.* **2006**, *31*, 111–122.
(39) Li, X.-Q.; Zhang, W.-X. *J. Phys. Chem. C* **2007**, 6939–6946.
(40) Macdonald, J. E.; Kelly, J. A.; Veinot, J. G. C. *Langmuir* **2007**, *23*, 9543–9545.
(41) Daou, T. J.; Grenèche, J. M.; Pourroy, G.; Buathong, S.; Derory, A.; Ulhaq-Bouillet, C.; Donnio, B.; Guillon, D.; Begin-Colin, S. *Chem. Mater.* **2008**, *20*, 5869–5875.
(42) Hormes, J.; Modrow, H.; Bönnemann, H.; Kumar, C. S. S. R. *J. Appl. Phys.* **2005**, *97*, 10R102.
(43) Paulus, P. M.; Bönnemann, H.; van der Kraan, A. M.; Luis, F.; Sinzig, J.; de Jongh, L. J. *Eur. Phys. J. D* **1999**, *9*, 501–504.
(44) Murray, C. B.; Norris, D. J.; Bawendi, M. G. *J. Am. Chem. Soc.* **1993**, *115*, 8706–8715.
(45) Hessel, C. M.; Henderson, E. J.; Veinot, J. G. C. *Chem. Mater.* **2006**, *18*, 6139–6146.
(46) Silberberg, M. S. *Chemistry*; 6th ed. McGraw Hill: New York, USA, 2012.
(47) Fahlman, B. D. *Materials Chemistry*; 2nd ed. Springer, 2011.
(48) Hoffmann, R. *Angew. Chem. Int. Ed.* **1987**, *26*, 846–878.
(49) Saleh, B. E.; Teich, M. C. *Fundamentals of Photonics*; Wiley-Interscience, 1991.
(50) Cullis, A. G.; Canham, L. T.; Calcott, P. D. J. *J. Appl. Phys.* **1997**, *82*, 909–965.
(51) Brus, L. E.; Szajowski, P. J.; Wilson, W. L.; Harris, T. D.; Schuppler, S.; Citrin, P. H. *J. Am. Chem. Soc.* **1995**, *117*, 2915–2922.
(52) Kanemitsu, Y. *J. Lumin.* **2002**, *100*, 209–217.

(53) Nikolova, L.; Riabinina, D.; Kadari, B.; MacLeod, J. M.; Chaker, M.; Rosei, F. *ECS Trans.* **2010**, *28*, 15–31.
(54) Heath, J. R.; Shiang, J. J.; Alivisatos, A. P. *J. Chem. Phys.* **1994**, *101*, 1607–1615.
(55) Zhuravlev, K. K. *Physica B* **2007**, *394*, 1–7.
(56) Kreibig, U.; Vollmer, M. *Optical Properties of Metal Clusters*; Springer: Berlin, 1995.
(57) Van Zeghbroeck, B. V. *Principles of Semiconductor Devices and Heterojunctions*; 1st ed. Prentice Hall, 2009.
(58) Maeda, Y.; Tsukamoto, N.; Yazawa, Y.; Kanemitsu, Y.; Masumoto, Y. *Appl. Phys. Lett.* **1991**, *59*, 3168–3170.
(59) Brus, L. *Appl. Phys. A* **1991**, *53*, 465–474.
(60) Henderson, E. J.; Hessel, C. M.; Veinot, J. G. C. *J. Am. Chem. Soc.* **2008**, *130*, 3624–3632.
(61) Henderson, E. J.; Hessel, C. M.; Cavell, R. G.; Veinot, J. G. C. *Chem. Mater.* **2010**, *22*, 2653–2661.
(62) Hoffman, M.; Veinot, J. G. C. *Chem. Mater.* **2012**, *24*, 1283–1291.

Chapter 2:

Understanding the formation of elemental germanium by thermolysis of sol-gel derived organogermanium oxide polymers

A version of this chapter has been published:

Hoffman, M.; Veinot, J. G. C. Chem. Mater. ***2012****, 24, 1283-1291.*

2.1. Introduction

Group 14 semiconductor nanomaterials (*i.e.*, Si, Ge, and their alloys) constitute an attractive field of research, spurred by the observation of photoluminescence (PL) from Si nanostructures more than 20 years ago.[1] The unexpected size-tunable optical response of nanomaterials of indirect band-gap semiconductors, their prevalence in the electronics industry, and their biocompatibility have lead to extensive efforts in understanding and controlling their synthesis.[2] For both Si and Ge an extensive body of literature describes the synthesis of oxide-embedded as well as freestanding nanostructures. However, the understanding of Si nanomaterial chemistry has advanced much further than that of Ge. Thus, a detailed study of factors influencing the formation of Ge nanocrystals (NCs) is of paramount importance.

Free-standing Ge-NCs show promise in applications such as Bragg reflectors,[3] light-emitting diodes, solar cells,[4] and biological imaging[5,6] by virtue of their high refractive index and PL that extends well into the near-IR. Oxide-embedded Ge-NCs have been investigated for use in optical devices[7-11] as well as non-volatile memory,[7,12,13] where the smaller band gap, larger Bohr exciton radius and lower carrier effective masses compared to Si offer fast switching and write/erase speeds. In this context, Ge-NCs embedded in low-k (*e.g.*, SiO_2)[12,13] as well as high-k (*e.g.*, HfO_2)[7] dielectrics have been investigated. Recent reports have suggested the use of GeO_2 as high-k dielectric, making the study of its phase stability of interest to the electronics industry.[14,15] In this regard, it is particularly important to understand the thermal properties of germanium oxides and their

evolution at temperatures below 425 °C (*i.e.*, the thermal budget of a CMOS chip).[16]

2.1.1. Germanium nanocrystal synthesis

A variety of innovative procedures have been developed for the preparation of Ge nanocrystals. Key examples are summarized briefly in the following sections.

2.1.1.1. Zintl salt metathesis

Metathesis reaction of Zintl salts such as NaGe and Mg_2Ge with $GeCl_4$ to afford Ge-NCs has been investigated in detail by the Kauzlarich group. Reaction at reflux in glyme, di- or triglyme over periods from 2 to 24 hours followed by surface functionalization with alkyl lithium or Grignard reagents affords oxidatively stable alkyl-terminated Ge-NCs (Scheme 2.1).[17-20]

Scheme 2.1. Ge-NC synthesis by metathesis of Zintl salts (*e.g.,* NaGe) with tetrachlorogermane, followed by surface functionalization with alkyl Grignard or alkyl lithium reagents.

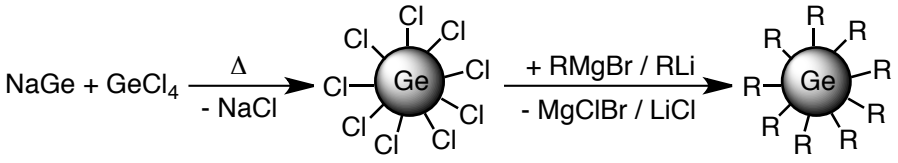

Reaction of $GeCl_4$ with NaGe yield Ge-NCs of 3.5 ± 1.2 nm diameter, with excitation-wavelength dependent PL peaking around 390 nm.[17] The choice of germanide (NaGe, KGe, Mg_2Ge) did not substantially affect Ge-NC formation.[18] Different precursor ratios and solvent offer limited size control in this method, however, larger Ge-NPs were amorphous and required annealing at 600 °C to achieve crystallinity.[18] These larger NCs show lower energy emission and the authors attributed this to quantum confinement, though the PL excitation energy used was also lower than for 3.5 nm Ge-NCs.[18] In the interest of direct comparison, it would be useful to report PL excited at the same energy. In a study of different terminal groups on alkyl functionalized Ge-NCs, (acetals, alcohols, esters), Ge-NCs from Zintl salt metathesis exhibit a PL maximum around 410 nm, independent of the surface group.[20]

2.1.1.2. Reduction of germanium halides

Scheme 2.2. Ge-NC synthesis by reduction of tetrachlorogermane, here showing the followed by surface functionalization with alkyl Grignard or alkyl lithium reagents.

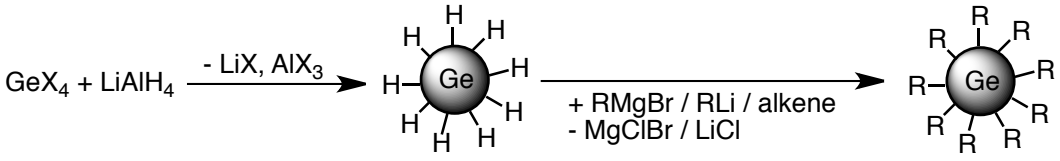

The most commonly reported approach to Ge-NC synthesis in solution involves reduction of germanium halides (Scheme 2.2). Though the use of hydride reducing agents leads to the formation of appreciable quantities of toxic and

pyrophoric GeH_4,[21] this synthetic approach receives much attention throughout the literature. This method produces Ge-NCs at room temperature with size control being offered by controlling the nature and concentration of the reducing agent, additives, and reaction temperature.

In an early report by Wilcoxon and coworkers, reaction of $LiAlH_4$ or hydrazine with tetrachlorogermane yielded Ge-NCs 2 to 10 nm in diameter.[22] PL was observed around 350 to 700 nm for crystalline clusters of 2-5 nm diameter.[22] In contrast, a narrower size distribution (6.7 ± 0.6 nm) could be obtained by ultrasonic reduction using $LiAlH_4$.[23] Smaller nanoparticles with narrow size distributions were obtained from ultrasonic reduction with $NaBH_4$ (4.8 ± 0.7 nm), or hydrazine (3.8 ± 0.6 nm) in the presence of octanol; no PL was reported in this study.[23] Interestingly, $NaBH_4$ reduction of $GeCl_4$ in a mixture of $C_{12}E_5$ (pentaethylene glycol monododecyl ether) / toluene gave substantially larger Ge-NCs (see Figure 2.1.d).[5]

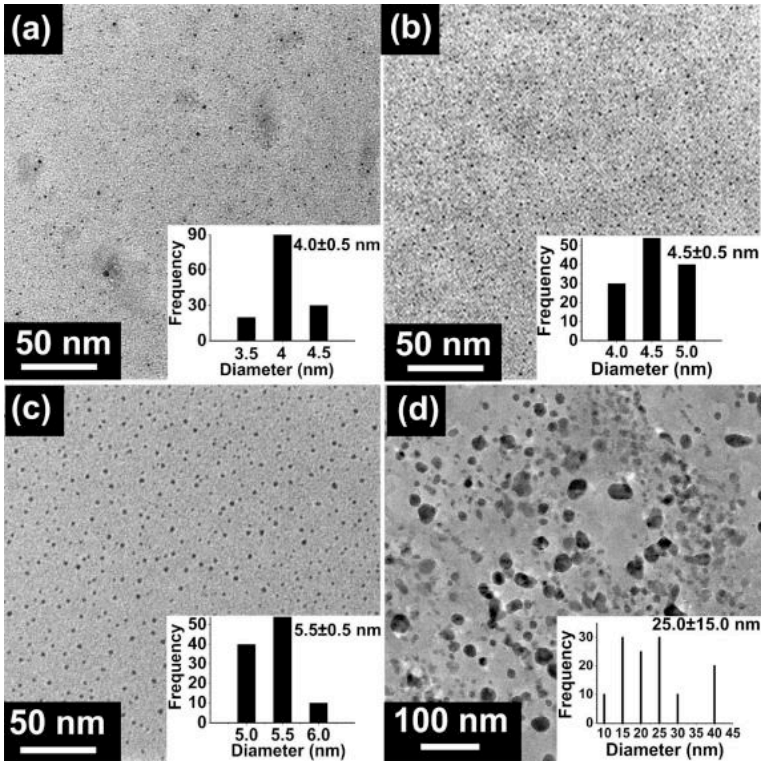

Figure 2.1. Ge-NC sizes obtained from reduction by (a) $LiAlH_4$, (b) $Li(C_2H_5)_3BH$, (c) $LiBH_4$, (d) $NaBH_4$ (reproduced from ref. 5).

This may be related to reducing strength, to the "inverse micelle approach", or to a difference in addition rates. Likely, reducing strength is not the key factor, since this difference was not observed in the other work described above. Both Tilley and Wilcoxon claim localization of the Ge-NC synthesis within inverse micelles, however, appreciable solubility of $GeCl_4$ in both phases brings into question the localization of Ge within micelles.[25] This could lead to poor size control. However, the observation of less polydisperse samples using different reducing agents (Figure 2.1.a-c) is not consistent with the micelle hypothesis. Instead, this difference may arise from different addition speeds or relative reactivity of the reducing agents.

Combined size and shape control arising from changes in reducing agent addition rate was demonstrated by the Tilley group.[24] Slow addition of superhydride to a mixture of $GeCl_4$ in toluene and trioctylammonium bromide (TOAB) resulted in the formation of Ge-NCs with a mean size of 5 nm, while fast addition lead to the formation of triangular particles 50 nm in diameter.[24] The 5 nm Ge-NCs exhibited blue PL of very short lifetime (1-2 ns), suggesting its origin was not the indirect band gap transition in Ge.[24]

Considering further studies involving sodium borohydride as reducing agent, inconsistencies become apparent. In a recent study, the reduction of $GeCl_4$ by $NaBH_4$ in the presence of polyvinylpyrrolidone (PVP) and ethylene glycol was reported to give amorphous NPs of 5 ± 1 nm, which were crystallized by annealing at 600 °C.[28] These particles were reported to oxidize within 30-60 minutes in air.[28] Recently, the Hu group reported $NaBH_4$ reduction of GeO_2 in basic solution, again in the presence of PVP, forming Ge-NPs with sizes ranging from 6-18 nm and blue PL after crystallization at 600 °C.[29]

Na(naphthalide) is yet another reducing agent that has been explored in Ge-NC synthesis. Reduction of $GeCl_4$ in 1,2-dimethoxyethane for 10 min yielded spheres of 3-7 nm in diameter that exhibited PL at 380 nm. Non-luminescent tetrahedra 30-49 nm in diameter were obtained after 45 min reaction.[25] The NCs were surface-functionalized using *n*-butyllithium.[25] Different sizes of Ge-NCs were achieved by varying the ratio of $GeCl_4$ to naphthalide reducing agent.[26] The Kauzlarich group further investigated temperature as a means of controlling size in this reaction, showing NC sizes after 10 min of reaction in glyme ranging from

an average of 5 nm at -40 °C to 11 nm at 70 °C.[27] These NCs were surface-functionalized using butylmagnesium chloride, no PL was reported.[27]

Germanium iodides are also often used as NC precursors in solution reduction. In 2004, the Veinot group reported the formation of blue-emitting Ge-NCs 2-7 nm in diameter using $LiAlH_4$ reduction of GeI_4 in toluene with cetyltrimethylammonium bromide (CTAB).[30] A variety of reports have investigated the formation of Ge-NCs from germanium iodides using butyllithium reagents.[4,31,32] Here, GeI_2 or a combination of GeI_2 and GeI_4 is heated to 200 °C in hexadecylamine. *n*BuLi (or *t*BuLi, in the Hanrath group example) in a solvent such as oleylamine or octadecene is injected, and the solution is brought to a final temperature of up to 300 °C. NC sizes were reported to increase with increasing all precursor concentrations, as well as with increasing GeI_4/GeI_2 ratio (where mixtures were used), and slower temperature ramp rate after injection of BuLi.[4,31,32] Near-infrared PL (Figure 2.2) as well as oxidative stability of 3-4 weeks at ambient conditions were observed upon reaction of Ge-NCs with octadecene.[4,31]

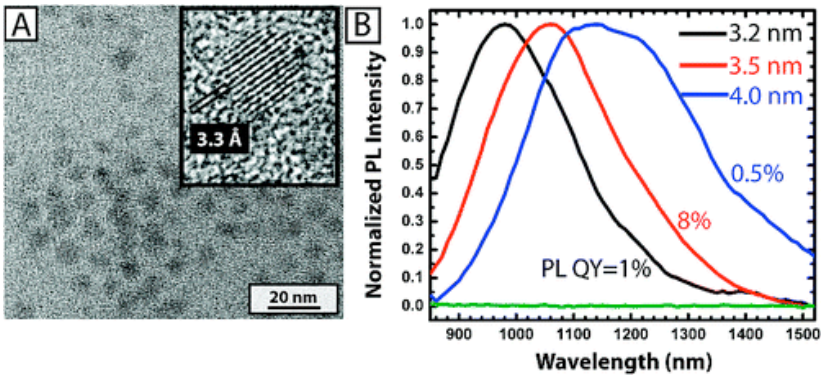

Figure 2.2. (A) Transmission electron micrograph (inset: high-resolution TEM) of Ge-NC 4 ± 1.7 nm in diameter. (B) NIR PL from Ge-NCs 3.2 – 4.0 nm in average diameter (reproduced from ref. 4).

2.1.1.3. Thermal decomposition

Scheme 2.3. Thermal decomposition of molecular germanes may form Ge-NCs.

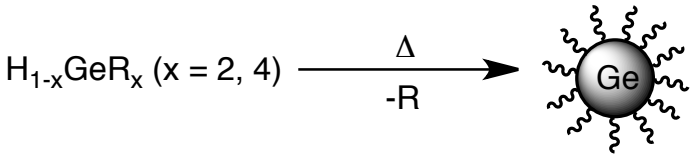

Another method for Ge-NC synthesis involves thermal decomposition of molecular germanes (Scheme 2.3). The Boyle group obtained Ge-NCs by hot injection of the amido-based precursor $Ge[N(SiMe_3)_2]_2$ in oleylamine into octadecene at 285 °C. A 5 min reaction yielded Ge-NCs of 7 ± 4 nm, showing relatively poor size-control. Excitation-wavelength dependent PL was explained by invoking different fractions of the nanocrystal size distribution. Since the

samples were handled purely in inert atmosphere, no information about oxidative stability is available for these samples.[33]

Thermal decomposition of organogermanes has also been investigated using tetraethyl-, diphenyl-, and tetrabutyl-germane.[34-36] Decomposition of tetraethylgermane at 450 °C in a mixture of supercritical hexane/octanol yielded polydisperse Ge-NCs with an average size of 4 nm and PL around 520 nm.[34] Using different amounts of diphenylgermane and tetraethylgermane at temperatures between 400 and 550 °C, this reaction provided control over NC size from an average of 2-70 nm, with low polydispersities.[35] Here, Ge-NCs of 3.1 ± 0.9 nm exhibited emission at ~390 nm, while Ge-NCs of 4.2 ± 0.4 nm emitted light ~530 nm.[35] The authors note this trend followed that expected for quantum confinement, but that the PL is very sensitive to surface chemistry, which is poorly controlled under the presented conditions.[35]

Zaitseva *et al*. investigated the synthesis of Ge-NCs from differently substituted precursors in hot injection.[36] Trichlorogermane was compared to tetramethyl-, tetraethyl- and tetrabutylgermane, though tetramethylgermane was excluded from further study based on having the highest decomposition temperature. In decomposition of the remaining precursors, the formation of amorphous Ge-NPs was observed below 400 °C. The alkylgermanes gave low yields of mixtures of Ge-NCs and Ge-NWs at higher temperatures, while $HGeCl_3$ yielded Ge-NCs 2-7 nm in diameter with PL at 540 nm.[36] The solvent was also found to influence crystallinity, with better results obtained in squalene than trioctylamine.[36]

2.1.1.4. Plasma pyrolysis

Scheme 2.4. Synthesis of mixed-surface Ge-NCs by plasma pyrolysis.

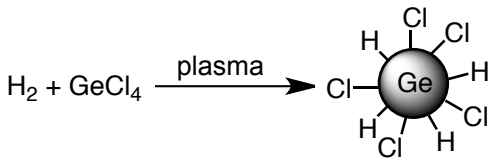

The Kortshagen group has shown Ge-NC formation in a nonthermal plasma (Scheme 2.4).[37] Here, $GeCl_4$ and H_2 are reacted in a nonthermal plasma flow reactor to yield Ge-NCs. Size control from 4 – 50 nm is given through the residence time of the forming NCs in the plasma. These NCs were not functionalized, and no PL was reported.[37]

2.1.1.5. Solid-state and physical methods

Solid-state approaches to freestanding Ge-NC synthesis are less common. Henderson *et al.* showed the synthesis of Ge-NCs from thermal reduction of a sol-gel copolymer of SiO_2 and GeO_2 in a hydrogen atmosphere (Scheme 2.5, Figure 2.3).[3] However, due to the dissimilar reaction rates of Ge and Si precursors in sol-gel reaction, and the diffusion of Ge to the material surface during thermal annealing, very low yields were obtained by this method, and no surface functionalization was demonstrated.[3]

Scheme 2.5. Sol-gel synthesis followed by solid-state reduction of GeO_2 nanodomains to Ge-NCs.

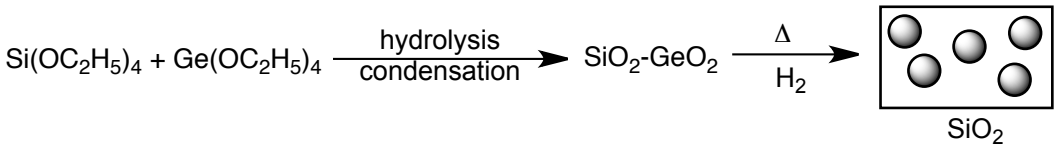

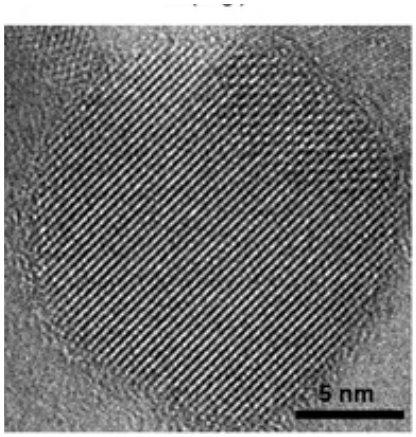

Figure 2.3. High-resolution transmission electron micrograph of Ge-NCs liberated from a silicon dioxide matrix. Adapted from ref. 3.

Sol-gel synthesis has also been explored for oxide-embedded Ge-NCs, using tetraethoxysilane (TEOS) in combination with tetraethoxy-, carboxyethyltrichloro- or tetrachlorogermane (TEOG, $EtAGeCl_3$ and $GeCl_4$).[38-40] Stoichiometric mixtures of TEOS and TEOG were combined in the sol-gel reaction and annealed in a hydrogen-containing atmosphere for different times at temperatures between 600-1000 °C, yielding Ge-NCs of different sizes, and with increased temperature also different shapes.[40] Evaporation of Ge from the oxide surface lead to the formation of bands of Ge-NCs within the oxide matrix.[40]

Similar results were obtained using $EtAGeCl_3$ and TEOS, with oxide-embedded Ge-NCs 1-13 nm in diameter. The nanocrystal size was found to increase with increased annealing time and temperature.[39] Reacting excess TEOS with $GeCl_4$ yielded a precursor that produced oxide-embedded Ge-NCs whose dimensions depend upon annealing temperature.[41] Low temperature (77K) PL was measured for samples with Ge-NCs obtained from this preparation with diameters smaller than 5 nm, no signal could be obtained for larger NCs.[41]

Oxide-embedded Ge-NCs have also further been generated in matrices including GeO_2, SiO_2, HfO_2 and ITO by radiofrequency sputtering, followed by annealing steps, as well as plasma-enhanced chemical vapour deposition (PECVD).[7-13,42,43]

While these materials are interesting they are prepared in relatively small quantities in thin film geometries and are hence beyond the scope of the present discussion.

Clearly, sol-gel derived materials are convenient precursors for preparing germanium oxide-embedded Ge-NCs. Sol-gel synthesis affords compositional tuning, thin film formation, as well as bulk material quantities; it is also substantially less infrastructure-intensive than physical techniques often used for the synthesis of oxide-embedded Ge-NCs.[44] While equivalent Si-rich oxides have been investigated and their thermal behaviour is well understood,[45,46] the corresponding chemistry of Ge-rich oxide sol-gel systems remains largely unexplored. Further, synthetic techniques such as scarce water addition enable the formation of solution processible oxides such as hydrogen silsesquioxane (HSQ),

a precursor to Si-NCs that is widely used as spin-on dielectric in microelectronics.[47,48] The HSQ molecule is a T_8 cage-structure, in which oxygen atoms bridge 8 HSi units in a cubic arrangement. Upon thermolysis, it crosslinks and decomposes to give oxide-embedded Si-NCs. Though structures such as the T_6 cage discussed in this work have been synthesized, HSQ-equivalent non-volatile structures of Ge providing a soluble oxide-embedded Ge-NC precursor have thus far not been demonstrated.

2.1.2. Background of the current study

Previously, our group reported the synthesis of Ge-NCs in a germanium oxide matrix via the thermolysis of a sol-gel derived precursor.[49,50] In this earlier study, phenyltrichlorogermane ($PhGeCl_3$) was used to prepare a $(PhGeO_{1.5})_n$ sol-gel polymer. Thermal processing of this polymer at appropriate temperatures (above 500 °C in 5% H_2/95% Ar, above 600 °C in 100% Ar) yielded a composite of Ge-NCs in GeO_2.

Mechanistically, the formation of Ge-NCs by thermolysis of the $(PhGeO_{1.5})_n$ polymer results from two different sources: disproportionation and reduction.[50] Upon thermal processing, the liberation of phenyl groups generates a substoichiometric oxide $(GeO_{1.5})_n$. This Ge-rich oxide undergoes a series of disproportionation reactions to form the thermodynamically favoured products (*i.e.*, elemental Ge and GeO_2). The contributing reactions are summarized in equation 2.1.

$$GeO_{3/2} + GeO_{3/2} \rightarrow GeO_{2/2} + GeO_{4/2}$$

$$GeO_{3/2} + GeO_{2/2} \rightarrow GeO_{1/2} + GeO_{4/2} \qquad (2.1)$$

$$GeO_{3/2} + GeO_{1/2} \rightarrow Ge + GeO_{4/2}$$

Since the processing temperature necessary for Ge-NC formation from $(PhGeO_{1.5})_n$ is high enough to afford hydrogen reduction of GeO_2,[51,52] reduction provides a second source of elemental Ge according to equation 2.2.[50]

$$GeO_x + x\ H_2 \rightarrow Ge + x\ H_2O \qquad (2.2)$$

Hydrogen reduction likely occurs preferentially at the surface of the oxide, leading to larger Ge deposits. In contrast, disproportionation reactions (eq. 2.1) are expected to occur uniformly throughout the oxide matrix, and Ge nanodomain growth from this source will be diffusion-limited. Hence, the additional reduction of GeO_2 may result in a NC product with wider size distribution, making it desirable to limit the source of Ge to a single pathway. While an inert processing atmosphere would remove the reduction pathway, it would also eliminate the well-established ability of hydrogen processing to improve NC optoelectronic properties by passivating crystal defects.[53,54] In the present study, the variation of organic substituents is shown to lower Ge-NC formation temperature below the thermal reduction threshold of GeO_2, effectively removing the reduction pathway.

Beyond the issue of competing reduction and disproportionation pathways, further drawbacks of the $PhGeCl_3$ precursor include its relatively high carbon

content and lack of solution processibility. First, decomposition of the organic group within the germanium oxide competes with Ge-C bond cleavage upon thermal processing, leading to carbonaceous residues within the composite that could alter Ge-NC/GeO_2 composite properties and present challenges in NC liberation. Second, the extended network structure precludes dissolution of the formed polymer for later application in thin-film coatings.

In the present contribution, the effect of the organic substituent R (R = H, C_2H_5, C_3H_5, n-C_4H_9, t-C_4H_9, C_7H_7, $C_3H_6O_2$) in $RGeY_3$ (Y = Cl, OC_2H_5) on sol-gel synthesis and thermally induced evolution of organogermanium oxides is discussed. Structural tailoring of the sol-gel polymer can reduce carbon impurities and lower the temperature of disproportionation below the threshold for hydrogen reduction of the oxide. In this way, the defect-passivating function of the hydrogen-containing atmosphere is retained,[53,54] while the Ge^0 formation is limited to a single source. This comprehensive study provides valuable insight into the thermolysis of sol-gel derived Ge-rich oxides and the mechanism of thermally induced Ge-NC formation.

2.2. Experimental Details

2.2.1. Material Preparation

2.2.1.1. Reagents and Materials

Allyltrichlorogermane ($C_3H_5GeCl_3$, >95%), benzyltrichlorogermane ($C_7H_7GeCl_3$, 95%), ethyltrichlorogermane ($C_2H_5GeCl_3$), ethyltriethoxygermane ($C_2H_5Ge(OC_2H_5)_3$), t-butyltrichlorogermane (t-$C_4H_9GeCl_3$), n-butyltrichlorogermane (n-$C_4H_9GeCl_3$), trichlorogermane ($HGeCl_3$) and carboxyethyltrichlorogermane ($HOOCC_2H_4GeCl_3$) were purchased from Gelest and stored in an argon-filled glovebox. Isopropyl alcohol (IPA) was obtained from Aldrich. All reagents were used as received. Ultrapure H_2O (18.2 MΩ/cm) purified in a Barnstead Nanopure Diamond purification system was used in all reactions.

2.2.1.2. Polymer preparation

In an argon-filled glovebox 5 g $RGeY_3$ (Y = Cl, OC_2H_5) were weighed into a three-neck round-bottom flask containing a stirbar and transferred to an argon charged Schlenk line. A mixture of 17 equiv. H_2O and 6.7 equiv. IPA was added dropwise while stirring. The flask was left opened to the atmosphere to vent HCl gas. After 1 hour, excess H_2O was added and the mixture was left to react over night. Heating for 3 hours at 70-80 °C promoted condensation, after which the polymer was cooled, filtered through a Büchner funnel with Fisher #1 filter paper and washed with H_2O until all acid was removed, followed by 100% ethanol. Prior to thermal processing, the white polymer was dried *in vacuo* for 2 days and

ground to a fine powder using an agate mortar and pestle. Individual conditions and yields are summarized in Table 2.1. Products were characterized by Fourier-transform infrared spectroscopy (FT-IR), X-ray diffraction (XRD), X-ray photoelectron spectroscopy (XPS), thermogravimetric analysis (TGA), elemental analysis (EA).

Table 2.1. Summary of sol-gel polymerization reactions.

Sample	Precursor (R-group)	pH	yield (%)[a)]	EA [%H]		EA [%C]	
				Calc.	Meas.	Calc.	Meas.
1	$C_2H_5Ge(OC_2H_5)_3$ (ethyl)	6	42	19.1	19.2	4.0	4.1
2	n-$C_4H_9GeCl_3$ (n-butyl)	1	88	31.2	30.7	5.9	4.6
3	$C_3H_5GeCl_3$ (allyl)	1	74	26.2	25.8	3.7	3.6
4	$C_7H_7GeCl_3$ (benzyl)	1	111	44.8	42.7	3.8	4.0
5	$HOOCC_2H_4GeCl_3$ (carboxyethyl)	1	35	21.1	20.5	3.5	2.9
6	t-$C_4H_9GeCl_3$ (t-butyl)	1	90	31.2	31.1	5.9	6.1

a) Yield calculations assume complete condensation (*i.e.*, product formula $RGeO_{1.5}$).

2.2.1.3. Composite preparation

Thermal processing was carried out in a Lindberg/Blue tube furnace using approximately 15 mL/min 100% Ar or 95% Ar / 5% H_2 as flow gas. $(RGeO_{1.5})_n$

polymer samples (100 mg or 500 mg) were transferred into a quartz boat, leaving 1 cm at both ends of the boat empty. For R = benzyl and n-butyl, powders were placed onto $(1.5\ cm)^2$ Si (100) n-doped wafer pieces. The boat was placed in a quartz tube and positioned at the furnace thermocouple. Thermal processing was performed at a heating rate of 18 °C/min to peak temperatures indicated in Table 2.3. The peak processing temperature was held for 1 h unless otherwise noted. It yielded composite powders of tan to black colour for all samples except R = benzyl, n-butyl, which formed black films. Powders of oxide-embedded Ge-NC composite were ground using an agate mortar and pestle prior to analysis. Characterization included XRD, XPS, FT-IR, EA, and for **7** transmission electron microscopy (TEM).

2.2.2. Material Characterization

2.2.2.1. Fourier-Transform Infrared Spectroscopy (FT-IR)

FT-IR was performed on a Nicolet Magna 750 IR spectrophotometer. Polymer and composite powders were pressed into KBr pellets, composite films were measured as-prepared in reflectance mode.

2.2.2.2. Thermogravimetric Analysis (TGA)

TGA was carried out using a Perkin-Elmer Pyris TGA equipped with Pyris Thermal Analysis 7.0 software. Samples were placed in a platinum pan and heated in a N_2 atmosphere from room temperature to 900 °C at 10 °C/min.

2.2.2.3. Matrix Assisted Laser Desorption Ionization Mass Spectrometry (MALDI-MS)

MALDI-MS was acquired using a Bruker 9.4T Apex-Qe FTICR spectrometer using an N_2 UV laser and a matrix of T-2-(3-(4-t-butyl-phenyl)-2-methyl-2-propenylidene)malononitrile (DCTB). The $(M+H)^+$ sample peak was evaluated in high-resolution with the instrument externally calibrated using the $(M+Na)^+$ peak of polyethylene glycol in a DCTB matrix.

2.2.2.4. X-Ray Crystallography

X-Ray Crystallography was performed at -100 °C on a Bruker D8/APEX II CCD diffractometer using Mo K_α radiation. The structure was solved using the direct methods program SHELXS-97, and refinements were completed using SHELXL-97. The absorption correction method used was face-indexed Gaussian integration. The solved structure was in accordance with a previous report.[55]

2.2.2.5. X-Ray Diffraction (XRD)

XRD was performed using an INEL XRG 3000 X-ray diffractometer equipped with a Cu K_α radiation source (λ = 1.54 Å). Crystallinity of all samples was evaluated for finely ground powders mounted on a low-intensity background Si (100) holder. Gaussian and Lorentzian line shapes were fit to (220) and (311) peaks of Ge to determine crystal size according to Scherrer's equation.[56]

2.2.2.6. X-Ray Photoelectron Spectroscopy (XPS)

XPS was performed on an AXIS-165 XPS spectrometer from Kratos Analytical. The base pressure and operating pressure in the chamber were

maintained at ≤ 10^{-7} Pa. A monochromatic Al K_α X-ray (λ = 8.34Å) was used to irradiate the samples, and the spectra were obtained with an electron take-off angle of 90°. Samples were pressed into carbon tape. To control sample charging, the charge neutralizer filament was used during the experiment. The pass energy for the survey and the high-resolution spectra were 160 and 20 eV, respectively. Spectra were calibrated to the C 1s emission at 284.8 eV attributed to adventitious carbon using CasaXPS (VAMAS) software. Following calibration, the background of each spectrum was subtracted using a Shirley-type background to remove most of the extrinsic loss structure. Fitting was carried out using Gaussian line shapes. Binding Energy values and orbital splitting were consistent with literature values obtained from the NIST database.[57]

2.2.2.7. Elemental Analysis (EA)

Carbon and hydrogen content were measured using a Carlo Erba (Thermo Scientific) EA1108 Elemental Analyzer CHNS-O equipped with Eager Xperience software. Composite films formed by R = benzyl, n-butyl $(RGeO_{1.5})_n$ polymer decomposition were mechanically scraped off the Si substrates for analysis.

2.2.2.8. Transmission Electron Microscopy (TEM)

TEM was performed using a JEOL 2010 Transmission Electron Microscope with a LaB_6 thermionic emission filament operated at an accelerating voltage of 200 kV. The instrument was fitted with an Energy Dispersive X-Ray (EDX) detector for elemental analysis. TEM samples were prepared by drop-coating ethanolic powder suspensions onto carbon-coated, 200-mesh Cu grids

(SPI Supplies). High-resolution TEM (HRTEM) was performed at the Canadian Centre for Electron Microscopy (CCEM) at McMaster University using a FEI TITAN 80-300 field-emission gun instrument operating at 300 kV.

2.3. Results and Discussion

Oxide-embedded Ge-NCs may be synthesized by thermal processing of Ge-rich oxides (GROs) derived from sol-gel reaction of organogermanium precursors ($RGeY_3$, Y = Cl, OC_2H_5). The following discussion outlines how the choice of organic substituent, R, affects sol-gel polymerization and thermal processing, giving access to GROs and Ge-NC composites with different physical properties (*e.g.*, melting temperatures, decomposition temperatures, volatility). This structural tailoring offered by the organic substituent enables Ge-NC formation at substantially lower temperatures (*i.e.*, R = ethyl: 400 °C *vs.* R = phenyl: 525 °C)[49,57] and provides mechanistic insight into the formation of Ge-NCs in these systems.

2.3.1. Synthesis of GROs by sol-gel polymerization

The initial aim of this study was to synthesize HSQ-analogues of Ge. HSQ (hydrogen silsesquioxane, $(HSiO_{1.5})_8$) is a solution-processible precursor to oxide-embedded Si-NCs synthesized by scarce water addition to $HSiCl_3$.[47] The synthetic method was adapted in an attempt to induce the formation of $(HGeO_{1.5})_8$ and

$(C_6H_5GeO_{1.5})_8$. Briefly, 9.4 mmol $RGeCl_3$ (R = H, C_6H_5) in 45 mL dry benzene were added dropwise by cannula to a biphasic mixture of 55 mL dry benzene, 13 mL concentrated sulphuric acid and 9.5 mL oleum (15%) under vigorous stirring over a period of two hours. The final mixture was extracted with conc. H_2SO_4 (2 x 30 mL), then water (3 x 20 mL). Upon addition of water to the reaction mixture, an insoluble white precipitate of $(PhGeO_{1.5})_n$ formed. Similar observations were made upon dilution of the synthetic procedure described in Section 2.2.1 with ethanol. We propose the complicating factor in the dilute synthesis of $GeO_{1.5}$ sol-gel structures is the lower propensity for condensation of Ge-OH in comparison to Si-OH, based on the lower thermodynamic stability of GeO_2 in comparison to SiO_2.

Extended-network GROs bearing different organic substituents were obtained using a sol-gel approach. Hydrolysis of the organogermanium precursor $RGeY_3$ (Y = Cl, OC_2H_5) with an ethanol/water mixture yields the trihydroxyorganogermane, which undergoes condensation to cage, ladder, or extended network structure GROs. The sol-gel reaction was acid-catalyzed for Y = Cl (*vide supra*) and at neutral pH for Y = OC_2H_5 (Scheme 2.6).[49*]

For R = H, these conditions did not yield the desired $(HGeO_{1.5})_n$ polymer. In this precursor, a competing auto-dissociation exists (eq. 2.3).

---

[*] Early in this study, Cl-substituted precursors were used exclusively. $C_2H_5GeCl_3$ did not yield the desired product under acid-catalyzed conditions. In the presence of base the NC-yielding polymer was only inconsistently obtained. The ethoxy-substituted precursor was then employed to avoid neutralization of 3 equiv. HCl during synthesis, which likely caused the reproducibility issues. pH studies of $C_2H_5Ge(OC_2H_5)_3$ sol-gel reaction showed no advantage of basic over neutral pH, leading to the neutral synthesis conditions described in this work.

$$HGeCl_3 \rightarrow HCl + GeCl_2 \qquad (2.3)$$

This side-reaction, coupled with the hydrolytic instability of the Ge-H bond, has in all instances lead to formation of GeO_2, not $(HGeO_{1.5})_n$.

Scheme 2.6. Formation of Ge-NC/GeO_2 composites from thermolysis of $(RGeO_{1.5})_n$ formed by hydrolysis and condensation of chloride- or alkoxy-substituted molecular precursors.

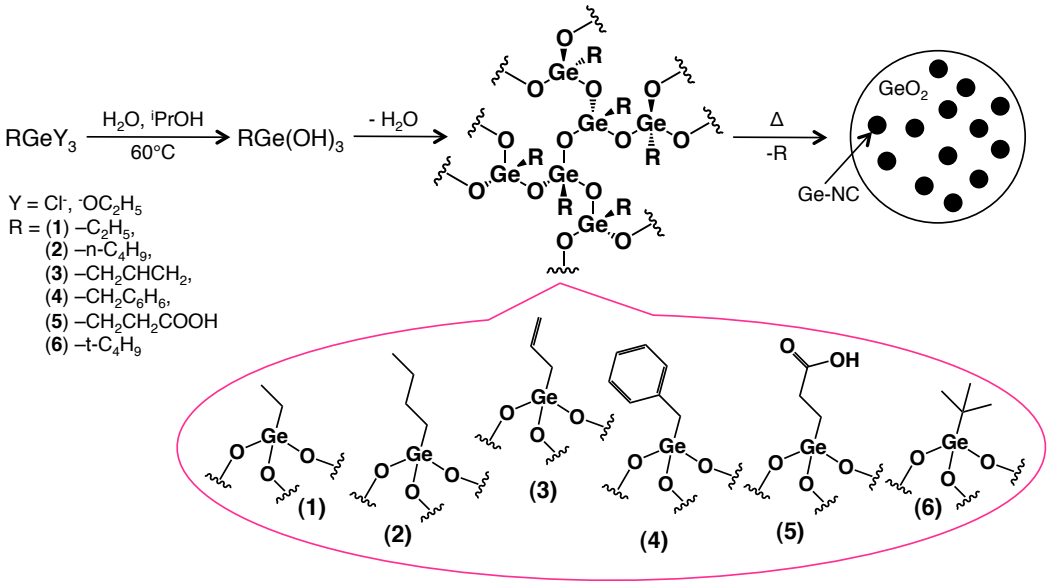

Characteristic, complex diffraction patterns in XRD (Figure 2.4), indicate long-range order in all GRO solids. Carbon and hydrogen contents probed by EA (Table 2.1) are largely consistent with the proposed $(RGeO_{1.5})_n$ stoichiometry. XPS (Figure 2.5) confirms the presence of Ge suboxides as evidenced by characteristic Ge 3d emissions ranging from 31.8 to 32.5 eV.[58] The degree of

condensation of the GROs can be evaluated indirectly using FT-IR (Figure 2.6) by examining the OH stretching region. **1**, **4** and **5** exhibit absorptions in the range of 3000-3700 cm^{-1}, suggesting the presence of uncondensed hydroxyl-groups. The FT-IR spectrum of **1** shows a weak, broad vibrational feature characteristic of a low concentration of hydroxyl-groups. For **4**, multiple relatively narrow features are observed in this spectral region, indicating OH groups in distinctly different environments with varying degrees of hydrogen bonding.[59,60] These narrow OH stretches may result from a GRO structure in which the steric bulk of the benzyl substituent has limited condensation of Ge-OH groups to form a complete Ge-O-Ge network (*vide infra*).[†] In the case of **5**, the broad OH stretch is shifted to lower frequencies associated with the carboxyl group of the organic substituent. As a result, no reliable information about the extent of condensation can be extracted for **5**.

[†] After extended storage (>1 year), NC formation at lower T (400 °C *vs.* 450 °C fresh) was noted: For the aged polymer, FTIR no longer showed OH stretching, suggesting these polymers are efflorescent or, more likely, completing condensation over time.

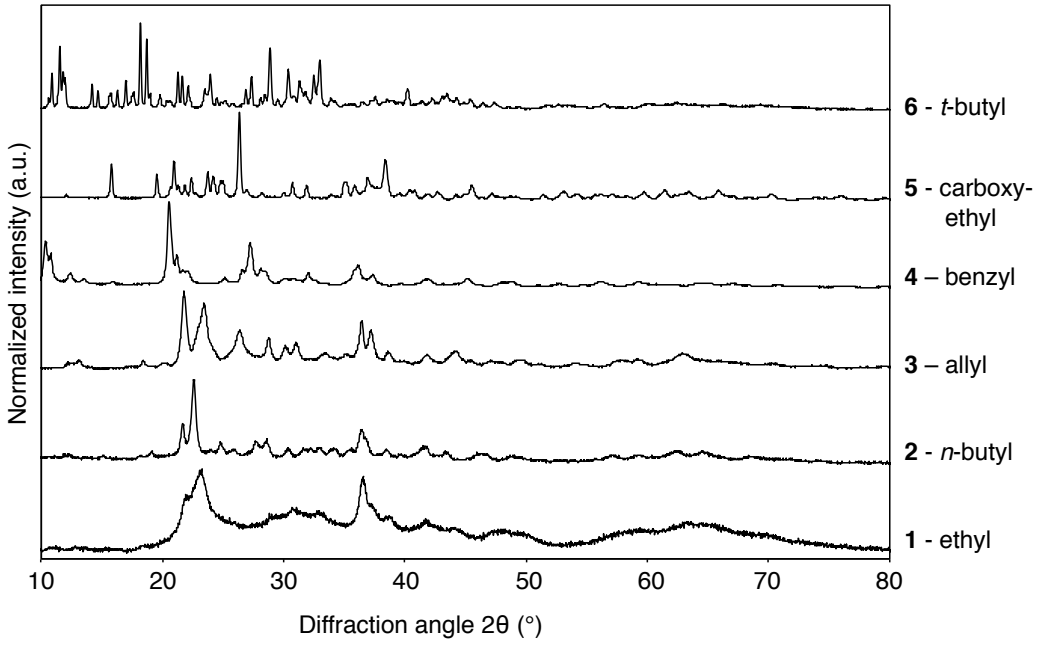

Figure 2.4. X-Ray Diffraction Patterns of GRO powders **1-6** before thermal processing.

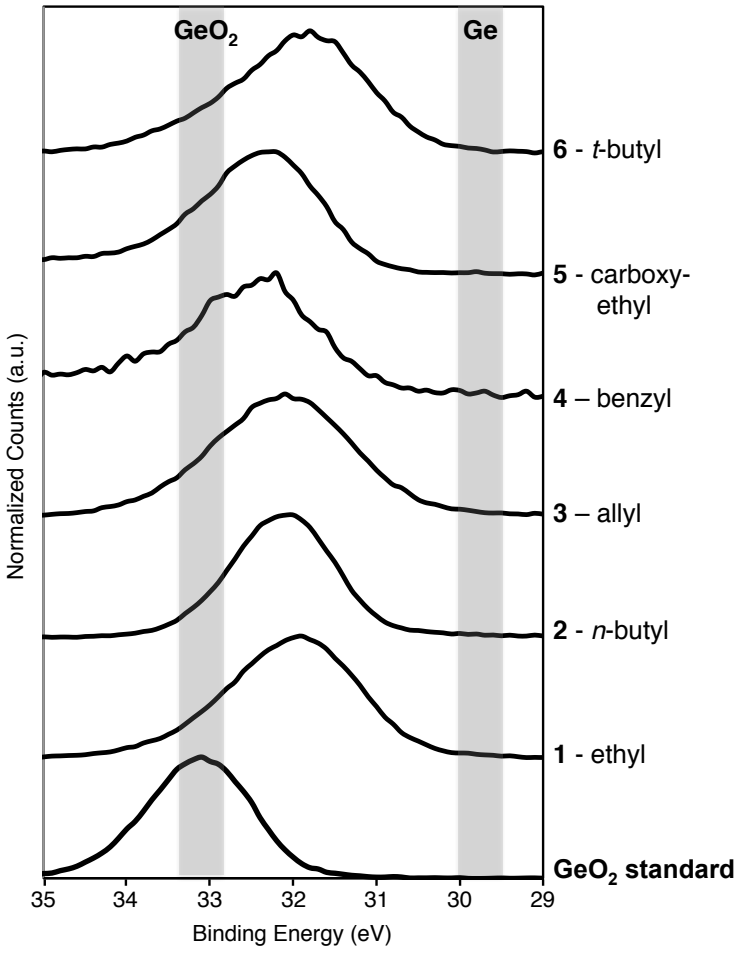

Figure 2.5. Ge 3d X-Ray Photoelectron Spectra of GROs **1-6** before thermal processing, and amorphous GeO_2 for reference.

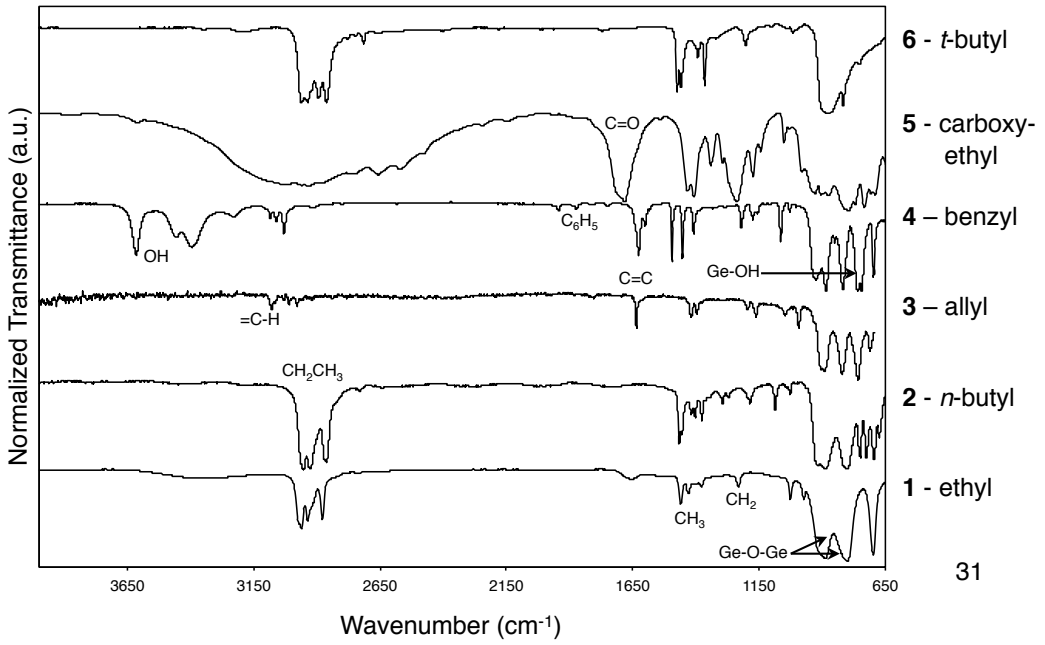

Figure 2.6. Fourier-Transform Infrared Spectra of GROs **1-6** before thermal processing.

Thermogravimetric analysis (TGA) of **1-6** provides insight into thermal decomposition (Figure 2.7). Of particular interest to the present study is a mass change associated with the loss of organic substituents. Removal of the organic substituent is expected to generate a "true" Ge-rich oxide $(GeO_{1.5})_n$ that can disproportionate to form elemental Ge according to equation 2.1. This simplistic view of the processes occurring during thermal processing does not consider factors such as incomplete condensation (*vide supra*) or precursor evaporation/sublimation arising from variation in GRO molecular weights (*e.g.*, cage *vs.* network structures). Still, TGA has proven useful in predicting substituent release as well as identifying appropriate processing temperatures for Ge-NC formation.

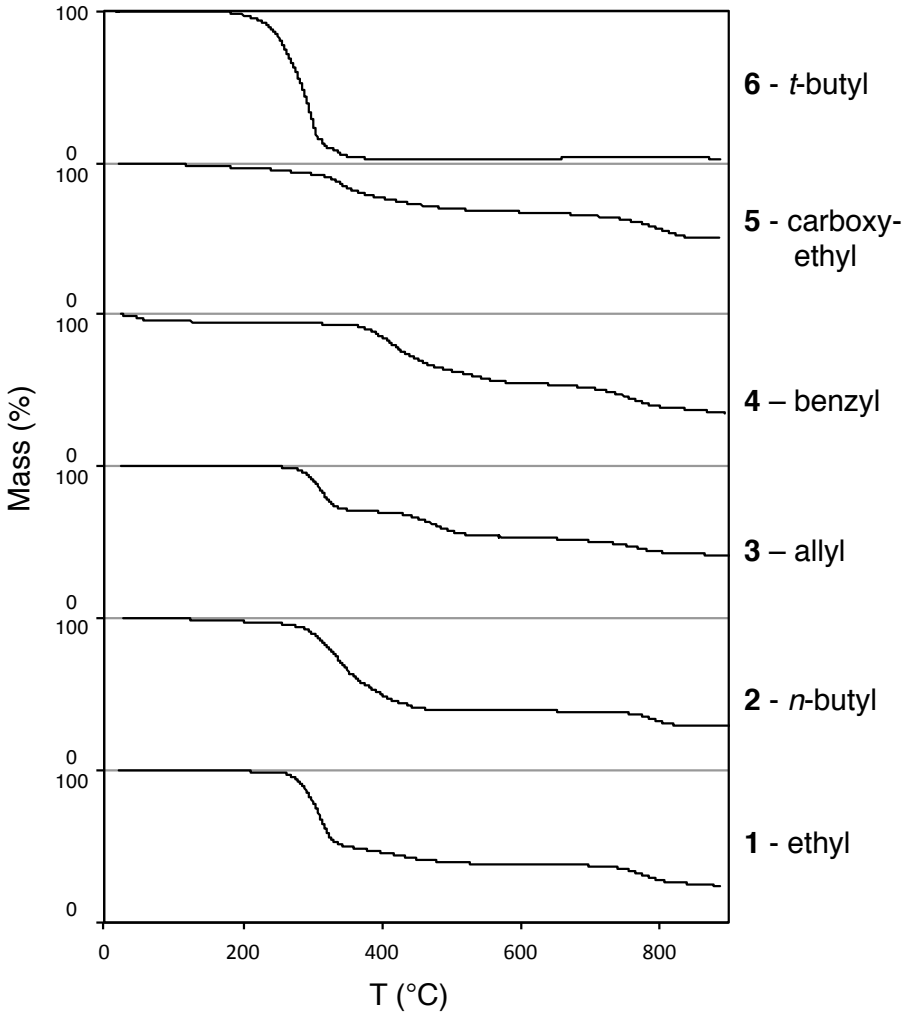

Figure 2.7. Thermogravimetric Analysis of GROs **1-6** before thermal processing.

Considering the mass loss presented in Table 2.2, three general observations were made: i) Complete mass loss at low temperatures (**6**), ii) Mass loss exceeding that associated with liberation of the organic substituents (**1-3**), and iii) Mass loss smaller than predicted for release of the organic substituent (**4, 5**). In cases (i) and (ii), the higher mass loss may be understood in the context of precursor evaporation due to the presence of low molecular weight GROs. This is likely the only reason for mass loss in the case of (i). In (ii), we expect contributions from elimination of the organic substituent as well as GRO evaporation; this is supported by the observation of different slopes within a mass transition and/or multiple loss events at different temperatures. Losses occurring at high temperatures (> 600 °C) are readily attributed to sublimation of Ge and/or GeO_x.[49,52]

Table 2.2. Mass loss observed in Thermogravimetric Analysis (TGA)

Sample #	R-Group (Formula)	Mass% of $(RGeO_{1.5})_n$	TGA Mass Loss[a)] [%]	T_{onset} [°C]
1	ethyl (C_2H_5)	23	62	276
2	n-butyl (n-C_4H_9)	37	61	293
3	allyl (C_3H_5)	30	46	284
4	Benzyl (C_7H_7)	49	45	372
5	carboxyethyl ($C_3H_5O_2$)	43	32	316
6	t-butyl (t-C_4H_9)	37	97	236

a) Mass loss is taken from TGA data at 600 °C.

Analysis of the only soluble sol-gel reaction product (*i.e.*, **6**) by matrix-assisted laser desorption ionization mass spectrometry (MALDI-MS) and X-ray crystallography supports the hypothesis concerning evaporation of low molecular weight fractions for cases (i) and (ii). These analyses show the formation of a low molecular weight germasesquioxane cage structure made up of six monomer units arranged in a trigonal prism bridged by oxygen atoms (Figure 2.8). The steric hindrance of the t-butyl substituent inhibits extended networking to the extent that cage structures are formed under both acid- and base-catalyzed conditions.[55,61] This precursor sublimes below 400 °C in TGA.

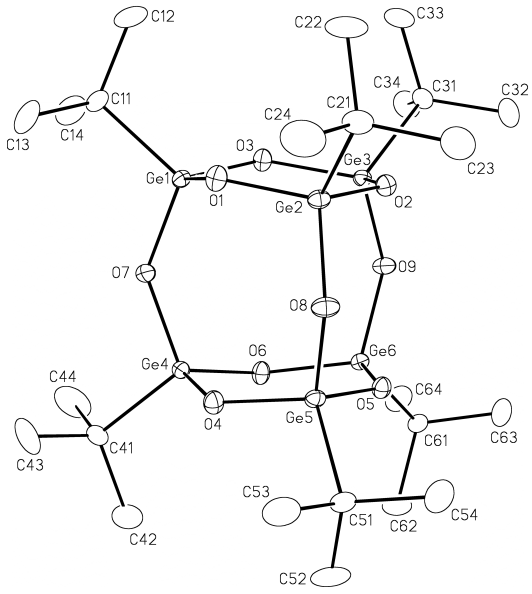

Figure 2.8. X-Ray crystal structure perspective view of the $[(tBuGe)_6O_9]$ molecule. Non-hydrogen atoms are represented by Gaussian ellipsoids at the 20% probability level. Hydrogen atoms are not shown. The full crystal structure report was published by Puff *et al.*[55]

From the data presented thus far, we propose the presence of bulky substituents on GROs leads to one of two arrangements: (i) cage structures, in which the bulky organic substituent inhibits network formation, or (ii) incompletely condensed network structures, in which bulky substituents hinder full condensation of hydroxyl groups. The former is observed for the bulky t-butyl substituent, while the latter is consistent with IR and EA data as well as synthetic yields exceeding 100% (calculated based upon complete condensation) for benzyl substituted precursors (see Table 2.1). The key difference between these two substituents is the CH_2-link in benzyl allows the bulky organic group to move about the Ge center, enabling network formation.

The temperature at which the organic substituent is lost is expected to determine the temperature of Ge-NC formation through disproportionation (*vide supra*). The temperature at which weight change begins decreases in the order **4, 5, 2, 3, 1** as seen in Table 2.2 (**6** is excluded from this discussion as it evaporates completely and does not undergo Ge-C bond cleavage). Assuming the weight change arises from loss of the organic substituents, this temperature should mark the beginning of $(GeO_{1.5})_n$ formation. The $(GeO_{1.5})_n$ can then undergo disproportionation to form elemental Ge. When the Ge-C bond is broken homolytically (as is likely the case for **3** and **4**, see Scheme 2.7a), the formed benzyl and allyl radicals are resonance-stabilized, while the unpaired electron of a phenyl radical resides perpendicular to the π-system, rendering its formation less energetically favourable and thus increasing the decomposition temperature. To rationalize the lower dissociation energy for **3** *vs*. **4**, we consider the respective

radical stabilities of the benzyl and allyl radical. Computations yielded a radical stability of 139.4 kJ/mol for benzyl and 126.2 kJ/mol for allyl.[62] In contrast, the phenyl radical had a theoretical stability of 247.5 kJ/mol (with larger values indicating lower stability).[62] Lastly, we have included substituents in our investigation that can be lost by the energetically less intensive bond rearrangement of β-H elimination (**1**, **2**, see Scheme 2.7b). As expected, these substituents yield Ge-NCs at the lowest temperatures that have thus far been recorded for these systems.

Scheme 2.7. Proposed elimination pathways for R-group cleavage.

(a) Homolytic bond cleavage

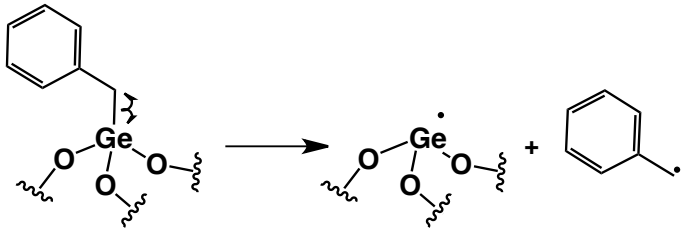

(b) β-Hydride elimination

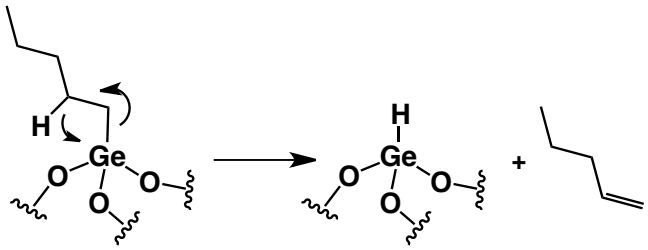

In an effort to establish which decomposition process is active, we investigated the gaseous decomposition products by TGA coupled with mass spectrometry (TGA-MS). For the different precursors, the mass spectra of molecular hydrogen, and the expected decomposition products from radical elimination were recorded. The setup was not capable of scanning the entire spectrum, limiting the amount of reliable information that could be extracted from the obtained data. For ethyl-substitution (**1**), m/z = 30 (C_2H_6) was observed in small quantities above 400 °C. Formation of hydrogen (m/z = 20) was apparent around 470 °C and plateaued at temperatures above 500 °C. The coupling product butane was not observed in this measurement. For benzyl-substitution (**4**), m/z corresponding to both C_7H_7 and C_7H_8 were observed above 300 °C. In contrast to TGA-MS of R = phenyl (previous work), where the coupling product biphenyl was observed, no coupling product ($(C_7H_7)_2$) was observed for R = benzyl. This may be attributable to the stability of the benzyl radical, as well as the harsh conditions in electron ionization mass spectrometry. Thus, the negative result of not observing the coupling product does not necessarily imply that radical cleavage is not the dominating mechanism of Ge-C bond cleavage.

2.3.2. Formation of Ge-NC/GeO_2 composites by thermal processing of GROs

GROs **1-5** were thermally processed to produce germanium oxide-embedded Ge-NC composites (see Table 2.3). Two general observations were made upon thermolysis: i) The formation of Ge-NCs in an oxide matrix maintaining the solid powder morphology (**7, 9, 11**) and ii) The formation of Ge-NCs in an oxide melt that solidifies to form films (**8, 10**). In the latter case, the

GROs are low melting (beginning at 200 °C for **2,** 320 °C for **4**) and likely undergo disproportionation in the solid and liquid state to yield black films of oxide-embedded Ge-NCs (Figure 2.9).

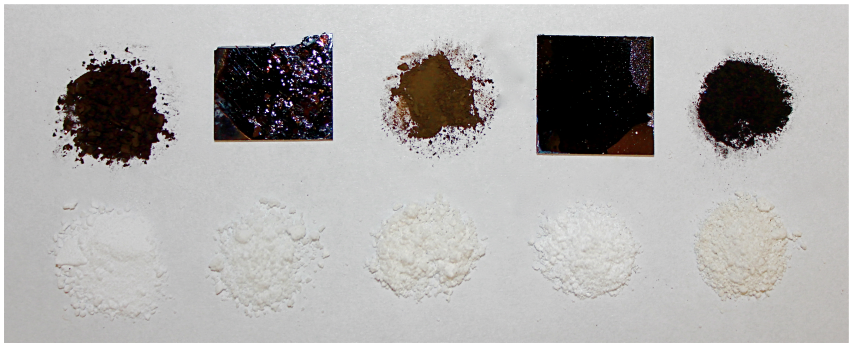

Figure 2.9. Photograph showing the physical appearance of GROs **1-5** (left to right, bottom) and corresponding Ge-NC/GeO_2 composites **7-11** (left to right, top). **8** and **10** are processed on Si wafer pieces.

The formation of Ge-NCs was confirmed by XRD. Figure 2.10 shows XRD patterns obtained for all GROs at the lowest processing temperatures at which Ge-NCs were detectable by XRD when processing for 1 h (see Table 2.3 for processing conditions). Broad reflections characteristic of diamond cubic crystalline Ge evidence Ge-NC formation in both composite melts (**2**, **4**) and powders (**1**, **3**, **5**). The background signal is attributed to the amorphous GeO_2 matrix. Notably, all substituents investigated in the present study form Ge-NCs at lower temperatures than the original phenyl-substituted GRO; we attribute this to their lower bond energies and more facile elimination pathways (*vide supra*). Scherrer analysis of the XRD reflections allows a first estimate of NC size,

though it offers no information about polydispersity of the present samples.[56] All samples appear to form similarly sized Ge-NCs at their lowest temperatures, except for **1**, for which Scherrer analysis suggests slightly larger NCs. More analysis is needed for definite size information, which is not the focus of the present study.

Table 2.3. Summary of sample processing showing lowest temperature at which Ge-NC formation was observed in XRD along with Scherrer analysis results for Ge-NC diameters. All samples were processed for 1 h in 5% H_2/95% Ar.

Sample #	R-group (GRO#)	Processing T [°C]	Mean NC diameter [nm]
7	ethyl (**1**)	400	22
8	n-butyl (**2**)	300	15
9	allyl (**3**)	400	12
10	benzyl (**4**)	450	11
11	carboxyethyl (**5**)	350	12

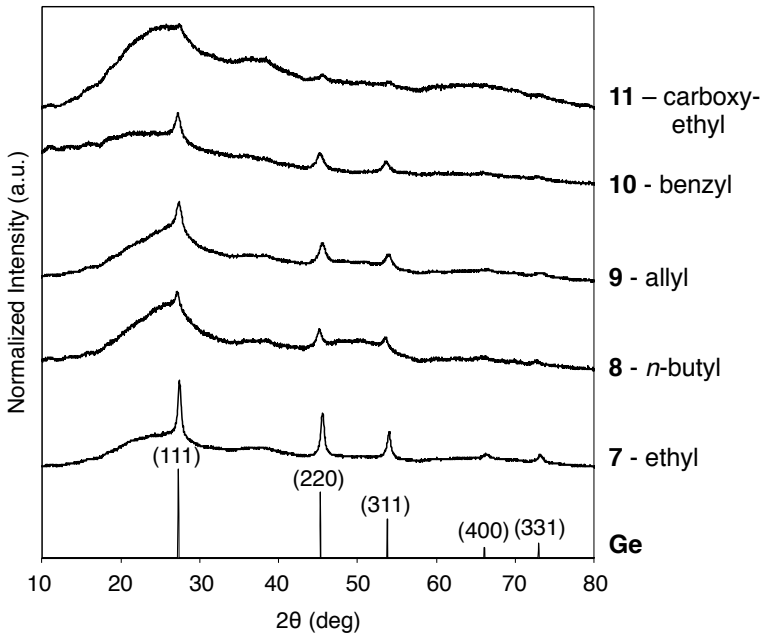

Figure 2.10. X-ray diffraction (XRD) patterns for GROs processed at the lowest Ge NC-forming temperature as indicated in Table 2.3. A standard bulk Ge pattern is included for comparison.

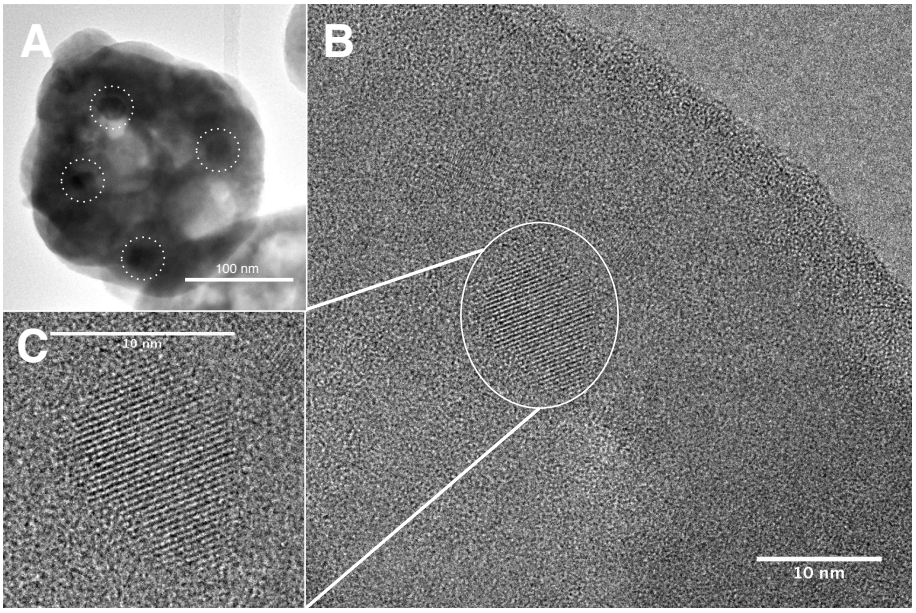

Figure 2.11. (A) Transmission electron micrograph of **7** (R = ethyl). Dotted lines highlight areas where the presence of Ge-NCs is suggested by a region of darker contrast. (B) High-resolution transmission electron micrograph of **7** showing lattice fringes of a Ge-NC embedded in amorphous oxide. (C) Close-up of the Ge(111) lattice fringes.

The presence of oxide-embedded Ge-NCs is suggested in transmission electron microscopy (TEM) imaging of composite **7**. The image presented in Figure 2.11A shows a microparticle of oxide-embedded Ge-NCs. Due to the different mass density of Ge and GeO_2, some mass contrast between Ge and its oxide is expected. The darker pseudospherical regions highlighted by white dotted circles on the image are consistent with Ge-NCs 20-25 nm in diameter, which corresponds well to Scherrer analysis results. High-resolution TEM (HRTEM) of **7** (Figure 2.11, B and C) confirms the formation of crystalline nanodomains with lattice spacings of 3.3 Å corresponding to Ge(111).[3] To make definitive conclusions about size and polydispersity of Ge-NCs liberation of freestanding Ge-NCs is required. Straightforward etching of the present GROs is complicated by carbon contamination and is the subject of ongoing studies.

XPS analyses, shown in Figure 2.12, are consistent with disproportionation occurring with thermal processing. A shift of the GRO intermediate oxide to higher binding energy, corresponding to Ge(IV), is observed. In some cases, the presence of elemental Ge is supported by an emission of low intensity at lower binding energy. This emission is expected to be of low intensity because Ge(IV) is formed in a ratio of 3:1 over Ge(0). For **7, 9,** and **11** the presence of zerovalent Ge is conclusively confirmed at the sensitivity of XPS. In the case of the film-forming composites **8** and **10**, Ge(0) is not observed under these processing conditions, but becomes apparent at higher processing temperatures (see Figures A5 and A7, Appendix A). The absence of emissions characteristic of elemental Ge may be due to the low concentration of

Ge-NCs as evidenced by low XRD intensities and/or the surface-sensitive nature of XPS.

FT-IR analysis of thermally processed Ge/GeO_2 composites gives further insight into the evolution from organically substituted GRO to Ge-NC containing oxide composite. FT-IR spectra shown in Figure 2.13 show a broadening of the Ge-O stretching at 880 cm^{-1}. This broadening is associated with restructuring of the organized GRO network to a disordered, amorphous GeO_2-like network in which Ge-NCs are embedded. OH stretching is observed in composites obtained from fully condensed, OH-free precursors. We propose the formation of hydroxyl groups occurs *via* H_2- or R-facilitated network opening (*vide infra*).

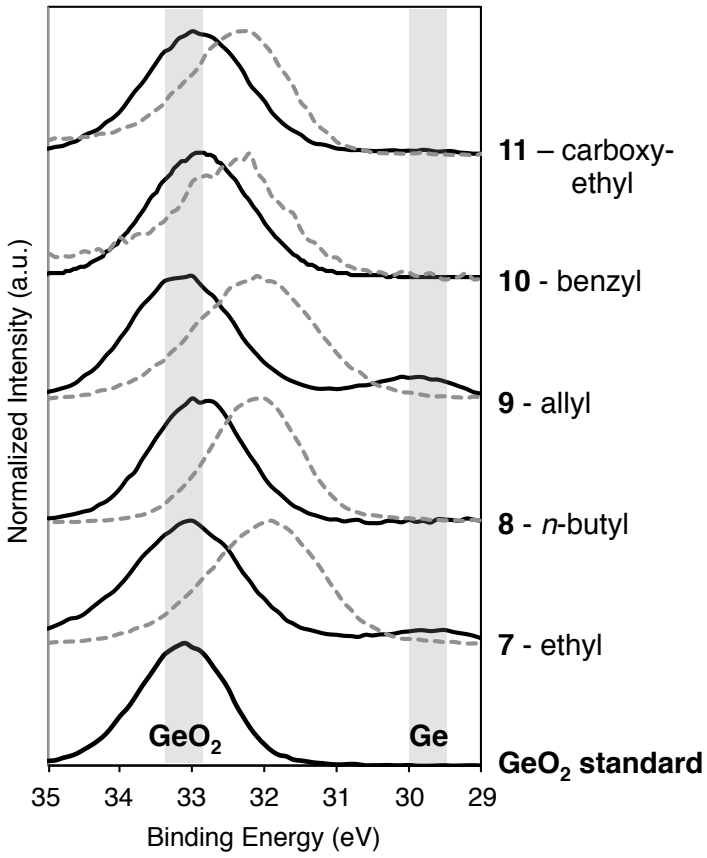

Figure 2.12. X-ray photoelectron (XP) spectra of the Ge 3d region for GROs (dashed lines) and their composites obtained from processing at the lowest Ge NC-forming temperature as indicated in Table 2.3 (solid lines). The XP spectrum of amorphous GeO_2 is included for comparison.

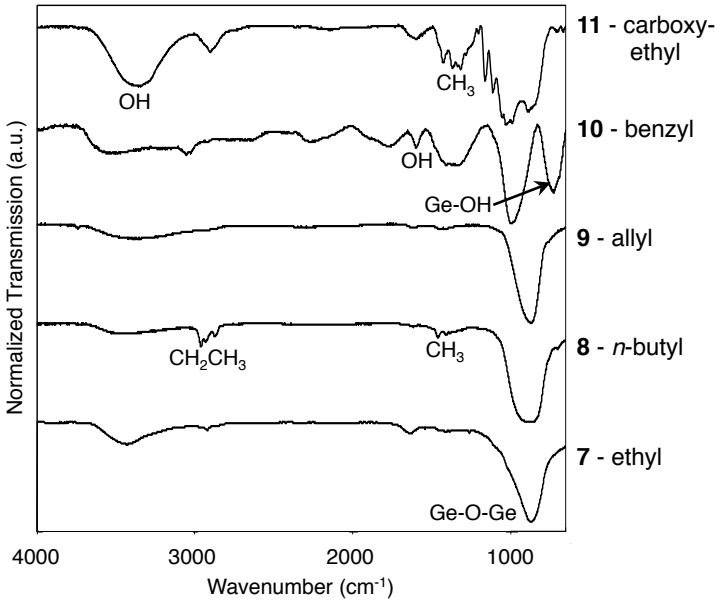

Figure 2.13. Fourier-transform infrared (FT-IR) spectra for GROs processed at the lowest Ge NC-forming temperature as indicated in Table 2.3.

Residual hydrogen and carbon content in **7-11** has been quantified by EA (Figure 2.14), confirming incomplete release of the organic substituent. Residual hydrocarbon content in Ge-NC/GeO_2 composites decreases from above 20% in **11** through the series **10, 9, 7** to less than 5% in **8**. Generally, less C remains for smaller R-groups, with the exception of **5**. Further, GROs with substituents capable of β-H elimination (**1**, **2**) have lower C content than those more likely to undergo radical elimination (**3**, **4**). We are currently investigating the nature of carbon impurities and their impact on oxide etching as well as the resulting Ge-NC properties.

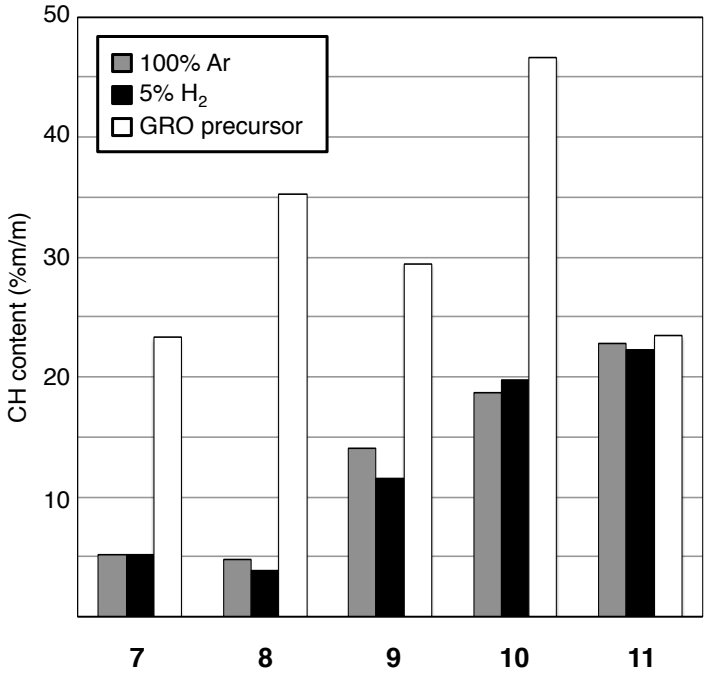

Figure 2.14. Elemental analysis (EA) of the hydrocarbon content of GROs processed at the lowest Ge NC-forming temperature as indicated in Table 2.3. The precursor GROs are included for comparison.

Quantum confined photoluminescence was not observed from the oxide-embedded materials in PL measurements from 350-800 nm (325 nm excitation), which is likely due to larger NC sizes as well as defect traps originating from the oxide surface or the carbon contaminations. PL studies would be of particular interest in the liberated products (freestanding Ge-NCs), which were not obtained for reasons previously discussed (*vide supra*).

2.3.3. Influence of processing temperature, time and atmosphere on Ge-NC formation

The analysis discussed in the previous section identifies GRO **1** as the precursor of choice for further study due to the lower initial Ge-NC formation temperature (400 °C for **7**), high melting point (powder morphology), and low residual carbon content (ca. 5%). Thus, the effect of peak processing temperature, processing time and atmosphere on GROs **1-5** will be illustrated with representative results for **1**.

As previously reported, XRD shows an evolution from the complex diffraction pattern of the GRO at room temperature to reflections characteristic of diamond cubic crystalline Ge upon increasing the peak processing temperature (Figure 2.15).[49] This transformation occurs via an amorphous germanium suboxide network that exhibits very broad reflections (*e.g.*, at 350 °C (1 h) for **1**). The Ge-NC reflections grow in and increase in intensity and sharpness upon increasing processing temperature and/or time. These observations are consistent with continued structural changes of the germanium oxide matrix.

When the peak processing temperature is held for 5 h, NC formation is consistently observed for all precursors at 50 °C below the minimum temperature needed to form Ge-NCs (as evidenced by XRD showing diamond Ge reflections) with a processing time of only 1 h. Ge-NC formation from these materials thus is not simply a function of temperature, but also of time. At lower temperature, the thermal energy provided is still sufficient to break Ge-C bonds, however Ge diffusion and NC nucleation and growth are slowed.

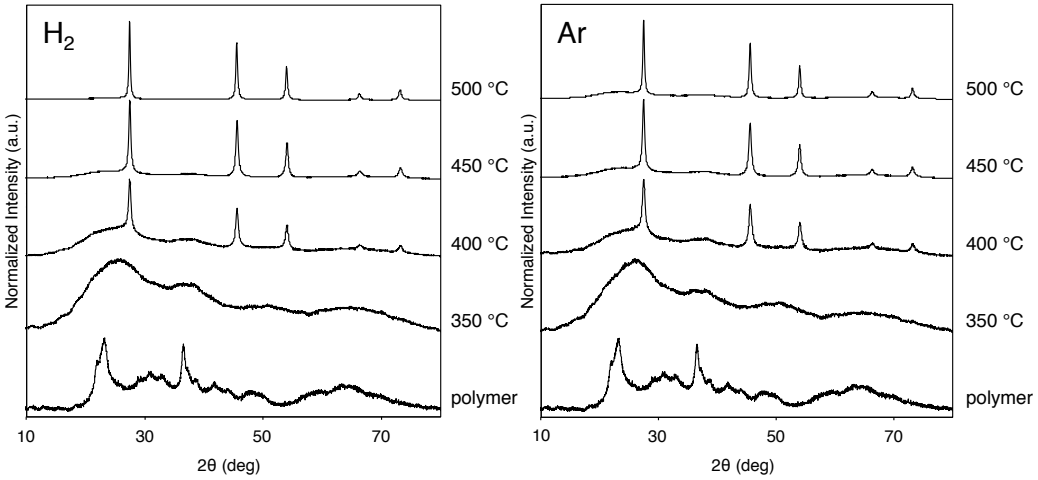

Figure 2.15. X-ray powder diffraction (XRD) patterns for **1** (R = ethyl) and its composites processed at indicated peak temperatures in 5% H_2/95% Ar (left) or 100% Ar atmosphere (right).

The contributions of reduction and disproportionation to elemental Ge formation were assessed by comparing composites processed at increasing temperature under a flow of 100% Ar or 5% H_2 (balance Ar). A comparison of the XRD patterns in Figure 2.15 as well as Figures A1-A4 (Appendix A) shows there are no substantial differences between inert and reducing atmospheres at temperatures below 500 °C. This is in stark contrast to observations in our original study of $(PhGeO_{1.5})_n$, for which Ge-NC formation below 600 °C was observed only in a reducing atmosphere.[50] The independence from processing atmosphere suggests formation of Ge-NCs from **1-5** proceeds only *via* disproportionation at low temperatures (< 500 °C). A comparison of XP spectra leads to the same conclusion. XP spectra of **1** processed at increasing temperatures show a shift of the intermediate oxide emission to higher binding energy (Figure 2.16). Concomitantly, a second emission at lower binding energy

associated with low- or zero valent Ge emerges. The observed shift of the oxide feature to higher binding energy and emergence of a shoulder at low binding energy are consistent with disproportionation (eq. 2.1). Since, at lower temperatures, all samples processed in inert and reducing atmosphere display comparable oxidation states within experimental variation, we conclude hydrogen reduction of oxides is not contributing substantially to the formation of elemental Ge. At temperatures of 450 °C and above, differences between XP spectra in inert and reducing atmosphere emerge. Hydrogen reduction of GeO_x is now evidenced by the presence of a more intense emission from lower-valent Ge in reducing *vs.* inert atmosphere. Since only a decreased background in XRD of H_2-processed composites is observed, and no substantial difference in Ge-NC size from Scherrer analysis is noted, we propose reduction is primarily leading to the nucleation of new Ge-NCs, not to increased growth of Ge-NCs formed from disproportionation. In summary, structural tailoring of the precursors provides a single-source Ge-NC synthesis that reaps the potential benefits of defect passivation in a hydrogen atmosphere without a substantial Ge contribution from reduction pathways.

First clues on the retention and nature of carbonaceous residues within the Ge-NC/GeO_2 composites are given by FT-IR and EA of composites processed at increasing temperatures. Upon increasing peak processing temperature, a decrease in intensity of vibrations associated with the organic substituents was observed in FT-IR (Figures 2.17, A9-12 (Appendix A)). Simultaneously, the narrow, strong absorptions for Ge-O-Ge stretching and bending of the sol-gel polymer merge into

one broad feature centered around 850 cm^{-1}. A broad, weak to medium-intensity feature in the OH-stretching region (3000-3500 cm^{-1}) is inconsistently observed in some samples that showed no OH-stretching in the precursor GRO (*vide supra*).

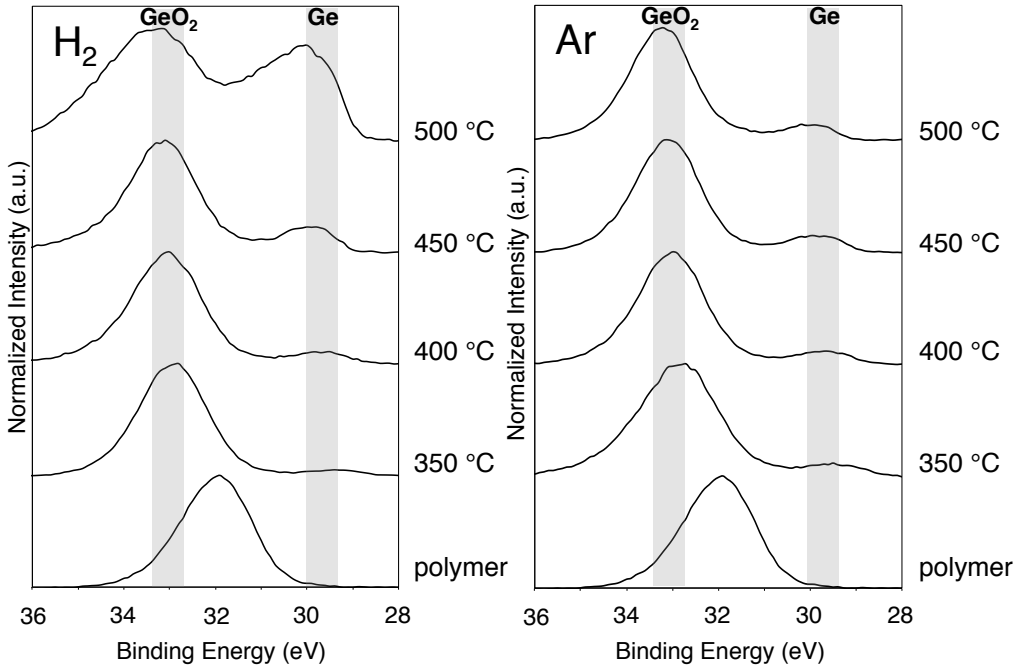

Figure 2.16. X-ray photoelectron (XP) spectra of the Ge 3d region for **1** (R = ethyl) and its composites processed at indicated peak temperatures in 5% H_2/95% Ar (left) or 100% Ar atmosphere (right).

In a reducing atmosphere, the breaking of Ge-O-Ge bonds may involve H_2, leading to the formation of OH-groups. In inert atmosphere however, the formation of OH-groups is proposed to result from the involvement of the organic substituent in breaking Ge-O-Ge bonds, since the organic substituent is the only source of hydrogen under these conditions. This reaction would lead to dehydrogenation of the organic substituent, which together with liberation of most organic substituents would explain the decreasing C-H stretching vibrations with increasing processing temperatures. This decomposition within the matrix would explain why EA results show sometimes-substantial amounts of carbonaceous materials within all oxide composites of **1-5**. The hydrocarbon content of composites decreases slightly with increasing processing temperature, except for composites of **5**, but complete removal is never achieved. The decreasing CH stretching intensity in FT-IR (as well as the loss of carbonyl according to FT-IR of processing of **5**) can thus be reasonably attributed to decomposition of the organic substituent within the Ge-NC/GeO_2 composite. The products of this decomposition are the subjects of ongoing study in our laboratory.

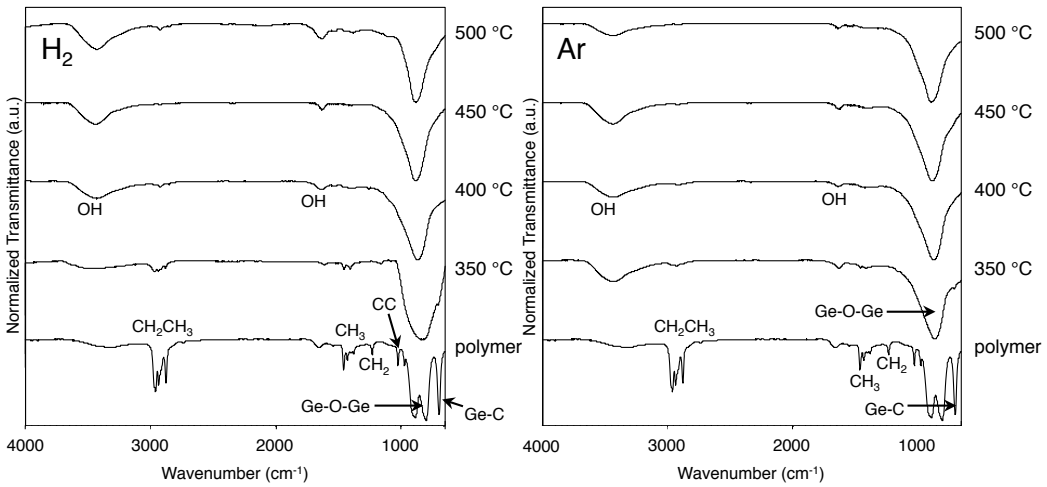

Figure 2.17. Fourier-transform infrared (FT-IR) spectra for **1** (R = ethyl) and its composites processed at indicated peak temperatures in 5% H_2/95% Ar (left) or 100% Ar atmosphere (right).

2.4. Conclusions and Future Work

By investigating the role of the organic substituent the temperature of Ge-NC formation has been decreased from 525 °C (R = phenyl) to 400 °C (R = ethyl) for Ge-NC containing composite powders and to 300 °C (R = n-butyl) for Ge-NC containing films. Notably, the lower temperature also leads to Ge formation from one source only: For a GRO processed in reducing atmosphere, the possible Ge sources are disproportionation, driven by the formation of the thermodynamic oxide, and reduction. Since oxide reduction only occurs at temperatures above 450 °C, the presented analysis supports the formation of Ge from only disproportionation. The disproportionation of a GRO is possible because the Ge-C bond to the organic substituent of the starting material can be thermally cleaved to generate a "true" GRO $(GeO_{1.5})_n$. Organic substituents that eliminate *via* β-H

elimination yield lower Ge-NC formation temperatures compared to substituents limited to radical elimination. Though retention of carbonaceous material in the composite is reduced in alkyl-substituted GROs, it remains an area of study to conclusively identify nature and location of the impurity. Attempts to remove remaining hydrocarbon impurities by processing in air or oxidative etching with H_2O_2 or HNO_3 have been unsuccessful due to the lower oxidation potential of Ge. A possible route for the future could be to introduce a pre-processing step where the sol-gel polymer is held at a lower T to promote Ge-C bond scission before heating to higher temperatures for Ge-NC formation. Preliminary TGA data shows this to be a promising route. Similarly, reliable liberation and functionalization of Ge-NCs from their oxide matrix is being actively pursued in our group.

2.5. References

(1) Canham, L. T. *Appl. Phys. Lett.* **1990**, *57*, 1046–1048.
(2) Fan, J.; Chu, P. K. *Small* **2010**, *6*, 2080–2098.
(3) Henderson, E. J.; Seino, M.; Puzzo, D. P.; Ozin, G. A. *ACS Nano* **2010**, *4*, 7683–7691.
(4) Lee, D. C.; Pietryga, J. M.; Robel, I.; Werder, D. J.; Schaller, R. D.; Klimov, V. I. *J. Am. Chem. Soc.* **2009**, *131*, 3436–3437.
(5) Prabakar, S.; Shiohara, A.; Hanada, S.; Fujioka, K.; Yamamoto, K.; Tilley, R. D. *Chem. Mater.* **2010**, *22*, 482–486.
(6) Lambert, T. N.; Andrews, N. L.; Gerung, H.; Boyle, T. J.; Oliver, J. M.; Wilson, B. S.; Han, S. M. *Small* **2007**, *3*, 691–699.
(7) Das, S.; Manna, S.; Singha, R.; Anopchenko, A.; Daldosso, N.; Pavesi, L.; Dhar, A.; Ray, S. K. *Phys. Status Solidi A* **2011**, *208*, 635–638.
(8) Shih, G. H.; Allen, C. G.; Potter, B. G. *Sol. Energy Mater. Sol. Cells* **2010**, *94*, 797–802.
(9) Razzari, L.; Gnoli, A.; Righini, M.; Dana, A.; Aydinli, A. *Appl. Phys. Lett.* **2006**, *88*, 181901.
(10) Maeda, Y. *Phys. Rev. B* **1995**, *51*, 1658–1670.
(11) Maeda, Y.; Tsukamoto, N.; Yazawa, Y.; Kanemitsu, Y.; Masumoto, Y. *Appl. Phys. Lett.* **1991**, *59*, 3168–3170.
(12) Ray, S. K.; Das, K. *Opt. Mater.* **2005**, *27*, 948–952.
(13) Choi, W. K.; Chim, W. K.; Heng, C. L.; Teo, L. W.; Ho, V.; Ng, V.; Antoniadis, D. A.; Fitzgerald, E. A. *Appl. Phys. Lett.* **2002**, *80*, 2014–2016.
(14) Hsu, C.-H.; He, Y.-D.; Yang, S.-F. *Cryst. Res. Technol.* **2011**, *46*, 65–68.
(15) Phani, A.; Di Claudio, D.; Passacantando, M.; Santucci, S. *J. Non-Cryst. Solids* **2007**, *353*, 692–696.
(16) Takeuchi, H.; Wung, A.; Sun, X.; Howe, R. T.; King, T. J. *IEEE Trans. Electron Devices* **2005**, *52*, 2081–2086.
(17) Taylor, B. R.; Kauzlarich, S. M.; Lee, H. W. H.; Delgado, G. R. *Chem. Mater.* **1998**, *10*, 22–24.
(18) Taylor, B. R.; Kauzlarich, S. M.; Delgado, G. R.; Lee, H. W. H. *Chem. Mater.* **1999**, *11*, 2493–2500.
(19) Taylor, B. R.; Fox; Hope-Weeks, L. J.; Maxwell; Kauzlarich, S. M.; Lee *Mater. Sci. Eng., B* **2002**, *96*, 90–93.
(20) Tanke, R. S.; Kauzlarich, S. M.; Patten, T. E.; Pettigrew, K. A.; Murphy, D. L.; Thompson, M. E.; Lee, H. W. H. *Chem. Mater.* **2003**, *15*, 1682–1689.
(21) Wilcoxon, J.; Provencio, P.; Samara, G. *Phys. Rev. B* **2007**, *76*, 199904(E).
(22) Wilcoxon, J.; Provencio, P.; Samara, G. *Phys. Rev. B* **2001**, *64*, 035417.
(23) Wu, H. P.; Liu, J. F.; Wang, Y. W.; Zeng, Y. W.; Jiang, J. Z. *Mater. Lett.* **2006**, *60*, 986–989.
(24) Warner, J. H.; Tilley, R. D. *Nanotechnology* **2006**, *17*, 3745–3749.

(25) Hope-Weeks, L. J. *Chem. Commun.* **2003**, 2980–2981.
(26) Hope-Weeks, L. J. *Chem. Lett.* **2005**, *34*, 1526–1527.
(27) Chiu, H. W.; Kauzlarich, S. M. *Chem. Mater.* **2006**, *18*, 1023–1028.
(28) Chou, N. H.; Oyler, K. D.; Motl, N. E.; Schaak, R. E. *Chem. Mater.* **2009**, *21*, 4105–4107.
(29) Wu, J.; Sun, Y.; Zou, R.; Song, G.; Chen, Z.; Wang, C.; Hu, J. *Cryst. Eng. Comm.* **2011**, *13*, 3674–3677.
(30) Fok, E.; Shih, M.; Meldrum, A.; Veinot, J. G. C. *Chem. Commun.* **2004**, *1*, 386–387.
(31) Codoluto, S. C.; Baumgardner, W. J.; Hanrath, T. *Cryst. Eng. Comm.* **2010**, *12*, 2903–2909.
(32) Ruddy, D. A.; Johnson, J. C.; Smith, E. R. R.; Neale, N. R. *ACS Nano* **2010**, *4*, 7459–7466.
(33) Gerung, H.; Bunge, S. D.; Boyle, T. J.; Brinker, C. J. J.; Han, S. M. *Chem. Commun.* **2005**, 1914–1916.
(34) Myung, N.; Lu, X.; Johnston, K. P.; Bard, A. J. *Nano Lett.* **2004**, *4*, 183–185.
(35) Lu, X.; Ziegler, K. J.; Ghezelbash, A.; Johnston, K. P.; Korgel, B. A. *Nano Lett.* **2004**, *4*, 969–974.
(36) Zaitseva, N.; Dai, Z. R.; Grant, C. D.; Harper, J.; Saw, C. *Chem. Mater.* **2007**, *19*, 5174–5178.
(37) Holman, Z. C.; Kortshagen, U. R. *Nano Lett.* **2011**, *11*, 2133–2136.
(38) Sharp, I. D.; Xu, Q.; Liao, C. Y.; Yi, D. O.; Beeman, J. W.; Liliental-Weber, Z.; Yu, K. M.; Zakharov, D. N.; Ager, J. W., III; Chrzan, D. C.; Haller, E. E. *J. Appl. Phys.* **2005**, *97*, 124316.
(39) Yang, H.; Wang, X.; Shi, H.; Wang, F.; Gu, X.; Yao, X. *J. Cryst. Growth* **2002**, *236*, 371–375.
(40) Knebel, S.; Kyriakidou, A.; Bracht, H.; Roesner, H.; Wilde, G. *Appl. Phys. A* **2011**, *103*, 149–158.
(41) Nogami, M.; Abe, Y. *Appl. Phys. Lett.* **1994**, *65*, 2545–2547.
(42) Gao, F.; Green, M. A.; Conibeer, G.; Cho, E.-C.; Huang, Y.; Pere-Wurfl, I.; Flynn, C. *Nanotechnology* **2008**, *19*, 455611.
(43) Dana, A.; Akca, I.; Ergun, O.; Aydinli, A.; Turan, R.; Finstad, T. G. *Physica E* **2007**, *38*, 94–98.
(44) Kelly, J. A.; Henderson, E. J.; Veinot, J. G. C. *Chem. Commun.* **2010**, *46*, 8704–8718.
(45) Hessel, C. M.; Henderson, E. J.; Veinot, J. G. C. *J. Phys. Chem. C* **2007**, *111*, 6956–6961.
(46) Siew, Y. K.; Sarkar, G.; Hu, X.; Hui, J.; See, A.; Chua, C. T. *J. Electrochem. Soc.* **2000**, *147*, 335–339.
(47) Frye, C. L.; Collins, W. T. *J. Am. Chem. Soc.* **1970**, *92*, 5586–5588.
(48) Baney, R. H.; Itoh, M.; Sakakibara, A.; Suzuki, T. *Chem. Rev.* **1995**, *95*, 1409–1430.
(49) Henderson, E. J.; Hessel, C. M.; Veinot, J. G. C. *J. Am. Chem. Soc.* **2008**, *130*, 3624–3632.
(50) Henderson, E. J.; Hessel, C. M.; Cavell, R. G.; Veinot, J. G. C. *Chem.*

Mater. **2010**, *22*, 2653–2661.
(51) Baba, H. *Bull. Chem. Soc. Jpn.* **1956**, 789–793.
(52) Hasegawa, R.; Kurosawa, T.; Yagihashi, T. *J. Jpn. Inst. Met.* **1970**, 132–137.
(53) Withrow, S. P.; White, C. W.; Meldrum, A.; Budai, J. D.; Hembree, D. M.; Barbour, J. C. *J. Appl. Phys.* **1999**, *86*, 396–401.
(54) Cheylan, S.; Elliman, R. G. *Nucl. Instrum. Methods Phys. Res. B* **2001**, *175-177*, 422–425.
(55) Puff, H.; Franken, S.; Schuh, W. *J. Organomet. Chem.* **1983**, *256*, 23–30.
(56) Patterson, A. L. *Phys. Rev.* **1939**, *56*, 978–982.
(57) *http://srdata.nist.gov/xps*.
(58) Wang, P. W.; Qi, Y.; Henderson, D. O. *J. Non-Cryst. Solids* **1998**, *224*, 31–35.
(59) Friedmann, G.; Gandon, C.; Boiron, G.; Staveris, S.; Bouilloux, A. *Eur. Polym. J.* **1998**, *34*, 351–361.
(60) Dai, J.; Goh, S. H.; Lee, S. Y.; Siow, K. S. *J. Polym. Res.* **1995**, *2*, 209–215.
(61) Nanjo, M.; Sasage, T.; Mochida, K. *J. Organomet. Chem.* **2003**, *667*, 135–142.
(62) Vleeschouwer, F. D.; Speybroeck, V. V.; Waroquier, M.; Geerlings, P.; Proft, F. D. *J. Org. Chem.* **2008**, *73*, 9109–9120.

Chapter 3:

The influence of substitution on thermal decomposition of molecular *n*-butylgermanes to germanium nanoparticles

3.1 Introduction

After 20 years of research effort in this field, Ge nanocrystal (Ge-NC) synthesis is still a challenging undertaking. Generally, the goal of Group 14 semiconductor synthesis at the nanoscale is to generate materials with well-defined optical and electronic properties governed by their size. Nanoscale materials represent the transition from molecules to bulk materials, and as such lie at the interface of molecular and solid-state chemistry. Nanomaterials will generally adopt bulk material structures, but their properties are strongly impacted by dimension. One reason for this behaviour lies in the drastically reduced number of bonding and antibonding orbitals that combine to form valence and conduction bands, the bulk equivalents of HOMO (highest occupied molecular orbital) and LUMO (lowest unoccupied molecular orbital). Comparing this decrease in atomic contributions to a molecular example, the HOMO-LUMO gap (which, in a bulk material, is just the band gap) shows the same dependence on atomic orbital contribution. Progressing, for example, from pentacene to benzene, an increase in HOMO-LUMO separation is observed due to the decreasing number of atomic orbitals contributing to its MOs (Scheme 3.1). Analogously, the band gap of semiconductor nanocrystals will increase with decreasing size.

An additional factor is the quantum confinement effect. Quantum confinement is understood to occur at nanomaterial sizes below the Bohr exciton radius (*e.g.*, 24.3 nm for Ge),[1] where the electron-hole pair formed upon excitation is confined to a closer distance than it would assume in a bulk material

(Scheme 3.2). This also leads to size-dependence of electronic and optical properties.

Scheme 3.1. Band gap energy decrease from benzene to pentacene.[2,3]

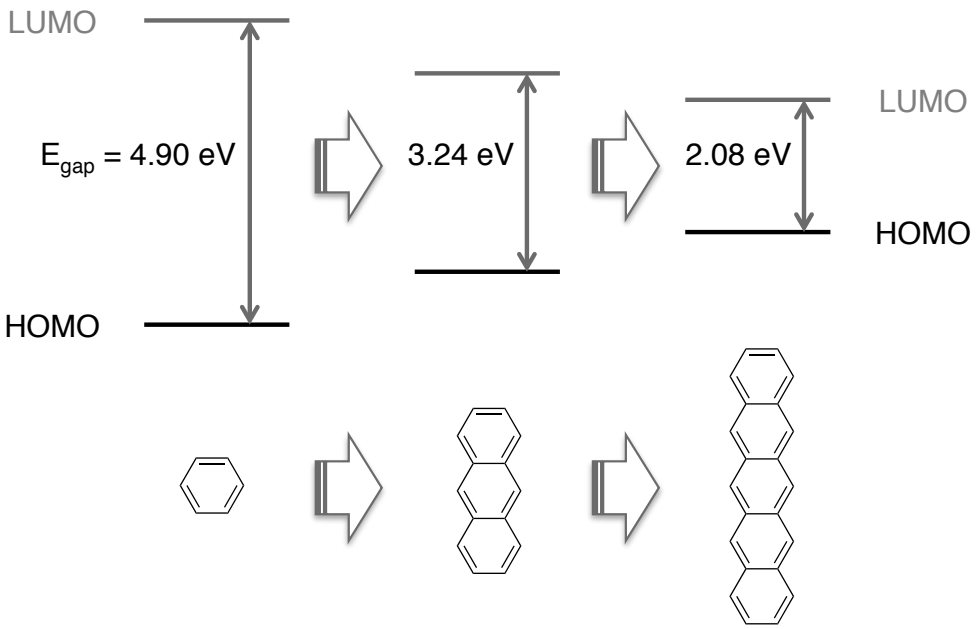

Scheme 3.2. Pictorial representation of exciton quantum confinement.

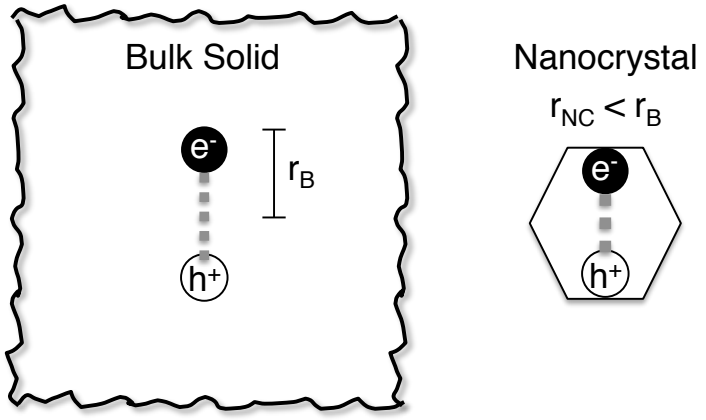

The energy of quantum confined photoluminescence, dictated by the NC band gap, can be predicted for a given material at a certain size using the effective mass approximation (EMA, equation 3.1).[4]

$$E(d) = E_g + \frac{\hbar^2 \pi^2}{2d^2}\left(\frac{1}{m_e^*} + \frac{1}{m_h^*}\right) - \frac{1.786e^2}{\varepsilon_r d} \qquad (3.1)$$

This equation is an approximation for a spherical particle where d is the particle diameter, E_g is the bulk band gap (0.66 eV at 300K)[5], $\hbar$ is the reduced Planck's constant, m_e^* and m_h^* are the lightest effective masses of electron and hole ($m_e^* = 0.082m_o$ and $m_h^* = 0.043m_o$)[1], e is the charge of an electron, and ε_r is the relative permittivity of Ge (ε_r (bulk Ge) = 15.8)[1]. As d decreases, the second term (zero point energy for particle in a box) increases faster than the third (effective Coulomb interaction between electron and hole), leading to an overall increase in band gap E(d).[6]

However, quantum confinement is only observed in near-ideal materials that are crystalline, defect-free and pure. Factors such as surface termination, impurities and defects will otherwise dominate the material properties. Addressing these issues is among the greatest challenges associated with Group 14 nanomaterial synthesis. After surveying the existing Ge-NC literature, it becomes apparent that many reports concerning Ge-NC luminescence are not consistent with predictions from EMA (Figure 3.1).[7-11] Reports detailing the synthesis of similarly sized Ge-NCs sometimes show very different luminescence

properties, while different sizes have been found to luminesce at very similar energy.

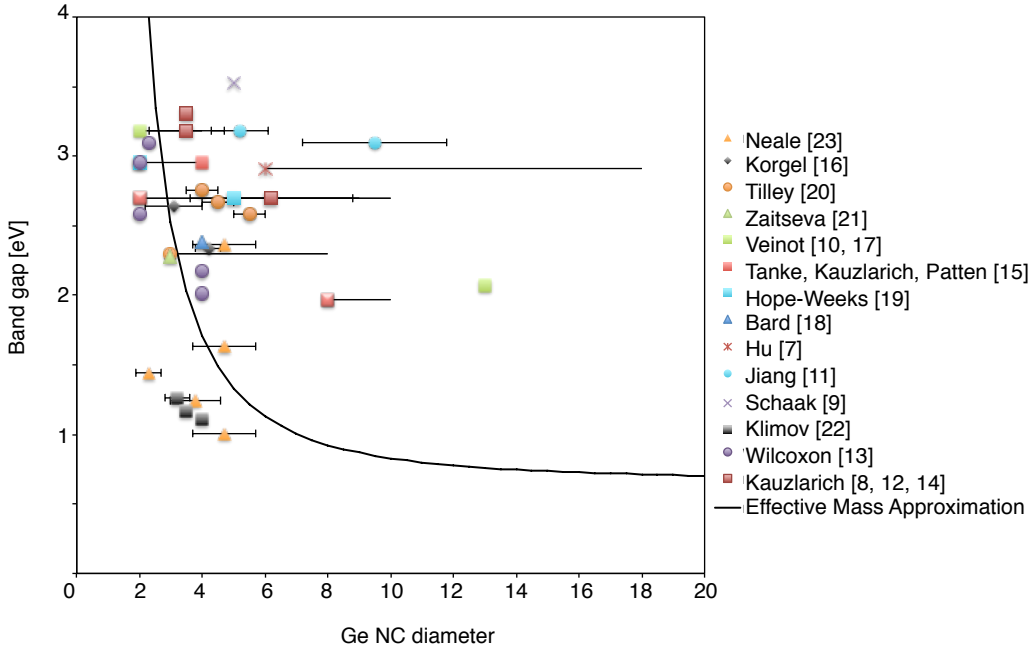

Figure 3.1. Graph comparing literature reports of Ge PL with predictions based on the effective mass approximation.[7-24] Data points represent reported Ge-NC diameters, plotted with error bars to represent either standard deviation (where available) or particle diameter ranges where average and standard deviation were not reported.

This discrepancy between theory and experimental observation is likely related to difficulties associated with synthesizing nanocrystals of covalent materials.[25] It is widely appreciated that Si and Ge, with their directional bonding, are more challenging to obtain in crystalline, defect-free form than ionic solid nanomaterials such as II-VI and III-V nanocrystals. Other issues that exist are the

influence of heteroatoms, difficulties with reliable surface passivation, and a generally poor understanding of the processes underlying Ge-NC formation.[22,26] This study aims to elucidate some of the factors influencing Ge-NC formation in solution synthesis.

In our previous investigation of the formation of Ge-NCs within an oxide matrix (See Chapter 2), we shed light on processes underlying the formation of elemental Ge from organically substituted precursors in the solid state.[27] In the seminal work, a phenyl-substituted germanium oxide polymer $(PhGeO_{1.5})_n$ was thermally decomposed above 500 °C to yield GeO_2-embedded Ge-NCs.[10,28] The loss of the phenyl group was postulated to occur *via* homolytic bond-cleavage, generating relatively unstable radicals. When the organic substituent was changed to a group that could eliminate as a more stable radical or *via* β-hydride elimination, we noted a substantial decrease in Ge-NC formation temperature (as low as 300 °C, for R= *n*-butyl). As an extension of our solid-state work, we are now interested in investigating molecular precursors of Ge-NCs containing *n*-butyl groups ($(n\text{-}C_4H_9)_xGeH_{4-x}$, with x = 1-4). The purpose of this study is to establish the influence of the substituents on decomposition temperature in solution synthesis. In the nBu_xGeH_{4-x} series, the presence of hydride substituents is proposed to decrease the thermal decomposition temperature by enabling decomposition pathways not accessible in the solid-state, in particular reductive elimination. Examples of Ge nanomaterial synthesis based upon decomposition of molecular organogermanes can be found in the literature, however, to the best of our knowledge, there are no systematic studies concerning the impact of

substitution on the decomposition process.[11,16,21,29-33] In particular, diphenylgermane and tetraethylgermane have been used in germanium nanomaterial synthesis, without providing a deeper understanding of the utility of the different organogermanes. Studies of organogermane decomposition in the gas phase support our hypothesis with regard to β-hydride elimination, with the observation of ethene in gas-phase tetraethylgermane decomposition.[34] Laser-induced photolysis of organogermanes in solution has been shown to be facilitated by hydride (and vinyl) substituents on Ge, though no mechanism was inferred in this work.[35] In a recent study regarding the synthesis of Ge nanowires, tetraethyl-, n-butyl-, and diphenylgermane were compared, and more favourable gas-phase decomposition was observed for diphenylgermane.[36] The arylgermane in this study appears to have more favourable decomposition kinetics originating from the redistribution chemistry it undergoes.[37,38] The decomposition of this compound (and possibly other organogermanes) is believed to proceed through redistribution reactions yielding tetraphenylgermane and germane, which then decomposes to elemental germanium and hydrogen gas. This process is supported by the observation of mono- and triphenylgermane in mass spectrometry of the products.[36]

In the context of bond strengths of differently substituted germanes, thermochemical and theoretical studies investigating homolytic cleavage have shown Ge-C bond dissociation energies depend on the nature of the organic substituent itself as well as the nature of the remaining substituents. Considering first the influence of the organic substituent on the Ge-C bond energy, a decrease

in bond energy from 346 kJ/mol to 306 kJ/mol has been noted with increasing carbon-substitution at the β-position of the alkyl chain, going from methyl to ethyl, isopropyl and *t*-butyl (Table 3.1, entries 1-4).[39] A similar trend is observed in Si-C bond energies of organosilanes, along with a dependence on chain length, which has not been investigated in detail for germanium.[40] Luo and Pacey describe the interaction of the β-carbon atom with germanium (Ge-C_α-C_β) as a strong electrostatic, non-bonding interaction, leading to weakening of the Ge-C bond analogous to weakening of C-C bonds in alkanes in the progression from ethane to propane to butane.[39] A comparable trend of decreasing bond energy is observed in bond dissociation energies of methyl-Ge and ethyl-Ge in tetraalkylgermanes determined by combustion (Table 3.1, entries 5, 6).[41,42] Interestingly, the phenyl-Ge bond dissociation energy of 324 kJ/mol is markedly higher than the bond dissociation energies of methyl- and ethyl-Ge bonds, indicating the observed differences cannot simply be regarded as β-substitution effects.[43] The electronic effects of the substituent as well as the nature and stability of the decomposition products can be expected to play into the observed bond energies.

Comparing the values obtained for methyl-Ge and ethyl-Ge bond energy in tetraalkylgermanes, 264 kJ/mol and 243 kJ/mol respectively, with the predicted values for the same bonds in monoalkylgermanes, 346 kJ/mol and 329 kJ/mol, a marked decrease in Ge-C bond energy is evident in the presence of further alkyl substituents. This may also be related to β-substituent effects, or inductive effects of the alkyl substituents. However, the trend in bond energy does not compare

well with the observation of substantially lowered decomposition temperatures with decreasing number of alkyl-substituents, as we observed in the current study. This suggests the trend of decreasing decomposition temperatures in the series $n\text{Bu}_x\text{GeH}_{4-x}$ (x = 4→1) is more likely related to the different available decomposition mechanisms than to the bond dissociation energies of Ge-C bonds based on radical formation.

Table 3.1. Ge-C bond strengths for different organic substituents in mono- and tetraalkylgermanes.

Entry	Ge-C Bond	BDE [kJ/mol]	Reference number
1	CH_3-GeH_3	346	[39]
2	C_2H_5-GeH_3	329	[39]
3	$^{i}C_3H_7$-GeH_3	317	[39]
4	$^{t}C_4H_9$-GeH_3	306	[39]
5	CH_3-$Ge(CH_3)_3$	264	[41]
6	C_2H_5-$Ge(C_2H_5)_3$	243	[42]
7	C_6H_5-$Ge(C_6H_5)_3$	324	[43]

Considering the understanding of R-group elimination pathways in more detail, the processes most applicable to our system are homolysis, β-hydride elimination, and reductive elimination (*vide supra*).[45] Homolysis generally leads to a complex mixture of products. According to Davidson, it is the predominating decomposition pathway in gas phase reactions at low pressures.[45] However,

homolysis has also been reported as the dominant process in surface decomposition of trialkylgallium compounds. In this case, the gas phase decomposition was observed to occur mainly by β-hydride elimination.[46] Characteristics of the organic substituent found to influence the decomposition process were the alkyl chain length, as well as the substitution at α-C. An increase in either weakens the M-R bond and stabilizes the formed radical. Higher substitution at the α-C also improves β-hydride elimination by providing a larger number of available hydrides.[46] Theoretical calculations by Maejima *et al.* indicate a lower activation barrier for β-hydride elimination of ethyl groups from diethylzinc in comparison to their homolytic cleavage.[47] Supporting the possibility of homolytic cleavage of R-groups from Ge, the generation of germyl radicals has been reported, even as stable amidometal-centered s^1 or s^2 complex $[(Me_3Si)_2N]_xGe\cdot$ (x = 2, 3).[45,48]

β-hydride elimination requires a vacant coordination site on the central metal atom.[45] The initial thought may be that a four-coordinate germanium compound will be unable to undergo this type of elimination, since it is coordinatively saturated with a full octet of electrons. However, coordination complexes of Ge have been synthesized with coordination of up to 6 ligands.[49,50] Though the bonding of these complexes is debated, we know that Ge has the ability to coordinate further species, making β-hydride elimination a possible decomposition pathway. In a comparison of Group 13 alkyl decomposition, B, Al and Ga alkyls preferentially decompose by β-hydride elimination, while In alkyls decompose both *via* homolysis and β-hydride elimination, with long chain alkyls

preferring radical elimination.[46] In surface reaction of ethylgermane on Si, ethane is observed and attributed to β-hydride elimination. However, this occurs following dissociative adsorption of the ethylgermane on the Si surface, and is thus actually elimination from Si, not Ge.[51] In Pd complexes, β-hydride elimination has been shown to have a lower activation barrier for C-N bond formation than reductive elimination, the third process raised as a possible elimination pathway in this study.[52]

Reductive elimination is generally understood to be confined to metals with stable oxidation states differing by two.[45] Arguably, Ge(II) is generally not a stable oxidation state, however, Ge(II) compounds including Ge(II) dialkyls are known.[45] Reductive elimination is sensitive to the electronic environment of the atoms combining to form a new bond, as well as the general electronic and steric environment of the compound or complex. Regarding the complex environment, reductive elimination from Ir has a lower activation barrier when steric demands of the remaining ligands decrease.[53] This was explained by a need of the alkyl or aryl groups to orient appropriately before elimination could proceed. For Pd on the other hand, the opposite has been reported.[54] Here, "steric relief" was believed to be a driving force for reductive elimination from sterically encumbered environments.[54] More importantly for our systems, the activation barrier of reductive elimination also depends on the electronic structure of the eliminating atoms. In C-C bond formation, $C(sp^3)$-$C(sp^3)$ reductive elimination is generally understood to be more difficult than $C(sp^2)$-$C(sp^2)$.[55] [Note: This dependence is, for example, not observed in the case of Ir][53] The directionality of the sp^3 orbital

doubles the activation barrier for C-C coupling compared to C-H coupling,[56,57] while the spherical nature of the H 1s orbital leads to there being virtually no activation barrier for H-H elimination.[56]

Once the molecular precursor is decomposing and atoms of elemental Ge are being formed, conditions such as Ge concentration, temperature, and coordinating solvents will influence nucleation and growth of Ge NPs. Nucleation and growth have been described by different theories that are increasingly able to give quantitative descriptions of the underlying processes.[58-60] For the purpose of this work, qualitative descriptions – along with their implications for experimental design – shall be sufficient. Classical nucleation theory (CNT) originally describes vapour-phase condensation, but has been extended to the nucleation of colloidal particles in solution.[61,62] The fundamental consideration in CNT is the interplay between Gibbs free energy involved in creating a new surface and Gibbs free energy of formation of the solid volume. Since the creation of a new surface is an unfavourable process, while the formation of the volume is favourable, nucleation will proceed when the volume-term is just large enough to cause an overall negative change in free energy. The nucleus size at which this criterion is met is referred to as the critical cluster size. Since this theory was originally developed for microscale particles, the critical cluster size is on the order of nanometers and is as such too large to accurately describe nanoparticle nucleation.[58] Further, the assumption of a uniform rate of attachment and detachment of atoms throughout the nucleation and growth process does not reflect size dependence of growth rates, or the local change in monomer

concentration as atoms are depleted by nucleation and growth.[59] Essentially, the CNT theory does not effectively describe the early stages of growth.[60]

An improved theory, which takes into account the local depletion of monomer upon burst nucleation of nanoparticles, as well as the changes in rate, is known as the LaMer model of burst nucleation.[63] This model describes the nucleation and growth processes from a starting point of strong supersaturation (C_S), which is followed by rapid nucleation of particles once the minimum concentration for nucleation C_0 is reached. After the maximum concentration for nucleation, C_N, is reached, the ongoing burst nucleation locally depletes the monomer, instantly decreasing the rate of nucleation and transitioning into a growth phase below C_0, during which diffusing matter is adsorbed onto the nucleus surface (Figure 3.2). This separation of nucleation and growth processes is projected to yield narrow size distributions, and has recently been quantitatively described by Privman and coworkers.[59] It does not, however, take into account phenomena such as Ostwald ripening and aggregation of particles.

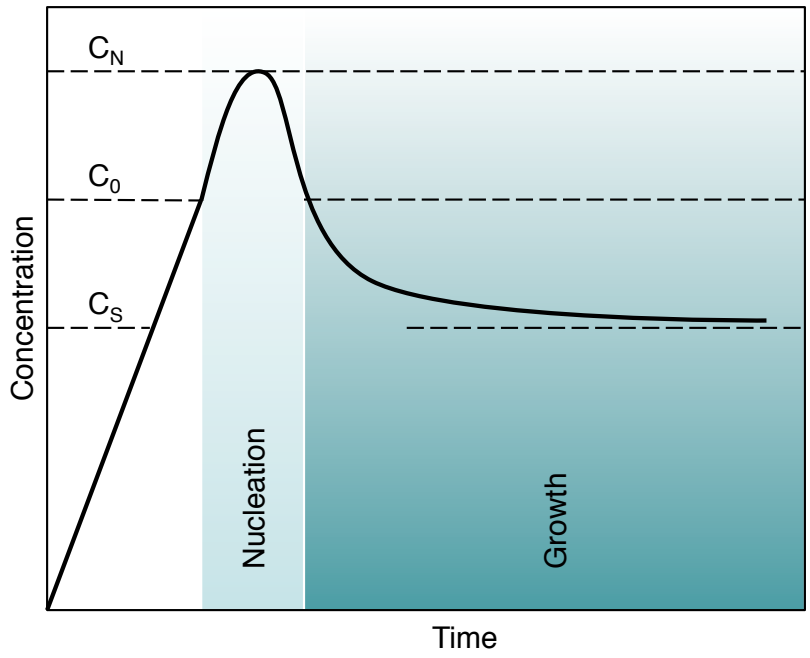

Figure 3.2. Nucleation and Growth as a function of monomer concentration as proposed by the LaMer theory of burst nucleation (adapted from ref. 63).

Ostwald ripening (also known as LSW theory, named after Lifshitz, Slyozov and Wagner) is a growth process in which small particles (with high energy due to high surface-to-volume ratio) dissolve, and release monomer that feeds the growth of larger particles (decreasing energy by decreasing their surface-to-volume ratio).[64-66] In their quantitative treatment of Ostwald ripening combined with CNT, Weller and coworkers conclude nanoparticle size distributions will 'focus' (narrow) when nucleation is suppressed early, and growth happens separately (analogous to LaMer burst nucleation, and achieved experimentally, *e.g.*, by hot injection).[60] This 'focusing' is achieved because small NCs will have a higher growth rate than their large counterparts. However, after a

certain period of growth, 'defocusing' (widening) of the size distribution is observed. In Bawendi's recent treatment of compound semiconductor nanocrystal nucleation and growth, the influence of temperature and additives is also investigated in some detail.[58] However, their conclusions likely cannot be reasonably directly extended to Group 14 semiconductor nanocrystal synthesis, because the strongly covalent character of Group 14 semiconductor bonding (in contrast to the significant ionic character of compound semiconductor bonding) influences their nucleation and growth behaviour.[26] So far, only one detailed experimental study of solution-phase nucleation and growth of Group 14 semiconductors has been published. Hanrath and coworkers have investigated these processes for the reduction of GeI_2, taking into consideration the influence of reducing agents, coordinating solvents, surface ligands, time and temperature.[26] Their results are not readily transferable to high temperature decomposition of organogermanes, thus the call for detailed understanding of the mechanistic processes underlying precursor activation chemistry, nucleation and growth of Ge nanoparticles by hot injection remains unanswered.

In this chapter, we describe a study of the influence of hydride-substitution on thermal decomposition of molecular *n*-butylgermanes to form Ge nanoparticles. The thermal decomposition of $n\text{Bu}_x\text{GeH}_{4-x}$ (x = 1-4) was investigated in hot injection experiments. In these experiments, the liquid precursor at room temperature is introduced by injection into a solvent heated to the desired temperature of reaction (285 – 400 °C). The solvents used in this study were octacosane ($C_{28}H_{58}$) and tri-*n*-octylamine. No additional surface capping

agent was employed to control surface passivation, primarily in order to keep the reaction conditions simple and avoid contamination. The decomposition temperatures of $n\text{Bu}_x\text{GeH}_{4-x}$ (x = 1-3) were determined by a series of experiments in which the reaction temperature was sequentially lowered by 10 °C until a colour change of the solution was no longer observed. The colour change, which at higher temperatures was accompanied by the formation of a black precipitate, suggests the formation of elemental Ge, and progresses from yellow just above the thermal decomposition temperature through orange, red-brown, and brown to black at higher temperatures. Thermal decomposition was compared for the different precursors at 400 °C in octacosane as well as 325 °C in octacosane and tri-*n*-octylamine. Products were analyzed for their sizes, shapes, crystallinity, oxidative stability and photoluminescence. No photoluminescence was measurable in the wavelength range from 350 – 800 nm with excitation at 325 nm.

3.2 Experimental Details

3.2.1 Material Preparation

3.2.1.1 Reagents and Materials

n-butylgermane (*n*-$C_4H_9GeH_3$), di-*n*-butylgermane ((*n*-$C_4H_9)_2GeH_2$), tri-*n*-butylgermane ((*n*-$C_4H_9)_3GeH$, 99%), and tetra-*n*-butylgermane ((*n*-$C_4H_9)_4Ge$) were purchased from Gelest and stored in an argon-filled glovebox. Octacosane ($C_{28}H_{58}$, 99%) and trioctylamine (TOA, $[C_8H_{17}]_3N$, 98%) were obtained from Aldrich. All reagents were used as received.

3.2.1.2 Identification of a suitable solvent

The literature report detailing Ge NP synthesis from tetra-*n*-butylgermane used trioctylamine, squalene and octacosane as solvents.[21] The reported respective boiling points are 384 °C, 412 °C, and 429 °C. Since tetra-*n*-butylgermane was reported to decompose at 390 °C, we wanted to investigate all compounds in the series nBu_xGeH_{4-x} (x = 1-4) at 400 °C. This ruled out trioctylamine as a suitable solvent for the high temperature reaction, but it was later used in hot injection experiments at 325 °C. Octacosane (mp 57-62 °C) is a solid at room temperature, which made squalene (mp -75 °C) our solvent of choice. Squalene has the added advantage of alkene functionality, which makes it amenable to surface protection through thermally initiated hydrogermylation if a Ge-H surface forms.[17] However, in our experiments, the maximum temperatures we could achieve in squalene were 308 °C and 325 °C, in two different batches of the solvent. Since the local

pressure in Edmonton varies between 700-704 mmHg (93.3-93.6 kPa) throughout the year,[67] a boiling point depression no larger than 3 °C would be expected (boiling point correction factor: $\left(\frac{760mmHg - p}{10}\right) \cdot 0.5°C$). We currently have no explanation for this stark discrepancy in observed boiling points. (NB: the boiling point stated on the solvent bottle is 284 °C at 25 mmHg, which corresponds to 420 °C at atmospheric pressure.) Thus, octacosane was chosen as the initial solvent for this study.

3.2.1.3 Hot injection synthesis of Ge NPs

9 g octacosane or trioctylamine (TOA) were weighed into a 25 mL three-neck round-bottom flask containing a glass-coated magnetic stirbar. The glass-coated magnetic stirbar was necessary, since polytetrafluoroethylene (PTFE, Teflon) melts at 327 °C. It is produced by stripping a Teflon-coated stirbar and coating the magnet with borosilicate glass. No surface capping agent was added to the reaction, though there is a possibility of butyl groups remaining on the nanoparticle surface, radical reactions of octacosane or its thermal decomposition products with the nanoparticle surface or Ge-N bonding with TOA. The three-neck round-bottom flask was equipped with a gas adapter, a condenser with gas adapter, and a thin glass sleeve with 14/20 ground glass joint to hold the thermocouple “in solution” (Figure 3.3.A). The three-neck round-bottom flask was placed in a sand bath contained in a metal bowl and covered with glass wool. The solvent was degassed above 110 °C under vacuum through the sidearm for 30

min. The flask was then refilled thrice with argon, the side gas line replaced with a septum (see Figure 3.3.B), and the solution heated to the desired temperature of reaction. The temperature was left to equilibrate for one hour before injection. In an argon-filled glovebox, 1.4 mmol $(n\text{-}C_4H_9)_xGeH_{4-x}$ were weighed into a vial with septum and transferred to an argon-charged Schlenk line. Using Schlenk techniques, the precursor was injected from a 1 mL glass syringe with 25 cm needle (18 gauge). The point of injection was at the bottom of the flask at each injection (Figure 3.3, pink area). The solution temperature was measured immediately after injection and was monitored throughout the reaction. After 30 min, the sand bath was removed, and the solution or suspension left to cool. When the solution had cooled below 110 °C, it was poured into ~75 mL toluene[‡] to avoid solidification of octacosane.[68] Reactions in TOA did not require addition of a second solvent. In the case of reactions performed at 400 °C in octacosane, black or grey suspensions were obtained, and the product was isolated by filtration through a Millipore hydrophobic Durapore membrane (type VVHP, 0.1 μm pore diameter). The black or grey powder was washed thoroughly with toluene and pentane to remove octacosane. At lower temperatures (280-350 °C) in octacosane, yellow to dark brown solutions were obtained, discounting filtration as a means of isolating Ge NPs. Instead, the majority of the octacosane solvent was removed as white, flaky crystals by recrystallizing briefly in an ice-bath and filtering through a Büchner funnel with 7 cm diameter Whatman #2 filter paper. Subsequently, toluene was removed by rotary evaporation, and the solid was

[‡] Determined by octacosane solubility, $x(C_{28}H_{58}) = 0.062$ in toluene at 306.5 K

dissolved in pentane. After centrifugation for 30 min at 14 krpm, brown precipitate was collected, and further purified by repeating centrifugation with pentane thrice. Reactions using TOA as solvent were worked up by centrifugation with ethanol:methanol (3:1) as antisolvent at 17 krpm for 10 min. Products were purified by centrifuging thrice with pure ethanol. Individual conditions are summarized in Table 3.2. Products were characterized by FT-IR, XRD, XPS, TGA, EA, Raman, and TEM.

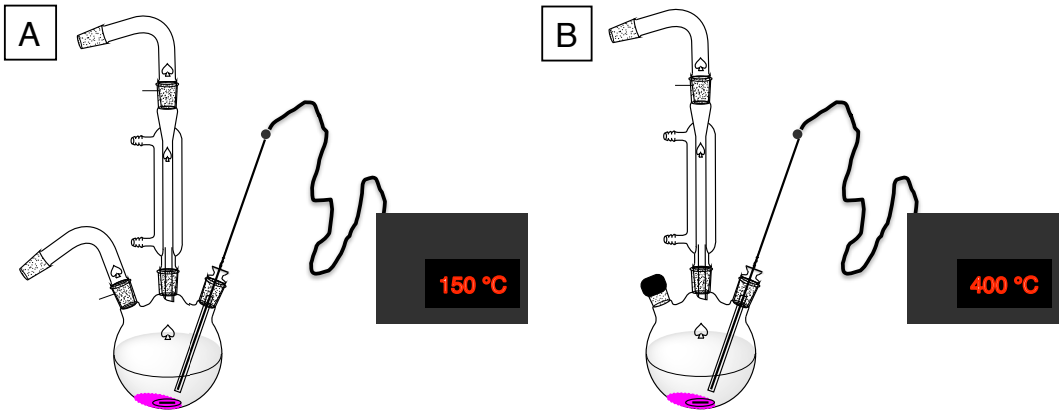

Figure 3.3. (A) Experimental setup for solvent degassing, (B) Experimental setup for hot injection, with the area of injection indicated in pink.

Table 3.2. Reaction conditions for hot injection of $n\text{Bu}_x\text{GeH}_{4-x}$.

Entry	Precursor	m($n\text{Bu}_x\text{GeH}_{4-x}$) [mg]	Solvent	T [°C]
1	$n\text{BuGeH}_3$	186	octacosane	400
2	$n\text{Bu}_2\text{GeH}_2$	264	octacosane	400
3	$n\text{Bu}_3\text{GeH}$	344	octacosane	400
4	$n\text{Bu}_4\text{Ge}$	422	octacosane	400
5	$n\text{BuGeH}_3$	186	octacosane	325
6	$n\text{Bu}_2\text{GeH}_2$	264	octacosane	325
7	$n\text{Bu}_3\text{GeH}$	344	octacosane	325
8	$n\text{BuGeH}_3$	186	trioctylamine	325
9	$n\text{Bu}_2\text{GeH}_2$	264	trioctylamine	325
10	$n\text{Bu}_3\text{GeH}$	186	trioctylamine	325

3.2.2 Material Characterization

3.2.2.1 Fourier-Transform Infrared Spectroscopy (FT-IR)

FT-IR was performed on a Nicolet Magna 750 IR spectrophotometer. Powders were pressed into KBr pellets (**1-3**) or measured under the microscope on reflective substrates (**4-10**).

3.2.2.2 Thermogravimetric Analysis (TGA)

TGA was carried out using a Perkin-Elmer Pyris TGA equipped with Pyris Thermal Analysis 7.0 software. Samples were placed in a platinum pan and heated in a N_2 atmosphere from room temperature to 600 °C at 10 °C/min.

3.2.2.3 X-Ray Diffraction (XRD)

XRD was performed using an INEL XRG 3000 X-ray diffractometer equipped with a Cu K_α radiation source (λ = 1.54 Å). Crystallinity was evaluated for powders mounted on a low-intensity background Si (100) holder.

3.2.2.4 X-Ray Photoelectron Spectroscopy (XPS)

XPS was performed on an AXIS-165 XPS spectrometer from Kratos Analytical. The base pressure and operating pressure in the chamber were maintained at $\leq 10^{-7}$ Pa. A monochromatic Al K_α X-ray (λ = 8.34Å) was used to irradiate the samples, and the spectra were obtained with an electron take-off angle of 90°. Samples were pressed into carbon tape. To control sample charging, the charge neutralizer filament was used during the experiment. The pass energy for the survey and the high-resolution spectra were 160 and 20 eV, respectively. Spectra were calibrated to the C 1s emission at 284.8 eV attributed to adventitious carbon using CasaXPS (VAMAS) software. Following calibration, the background of each spectrum was subtracted using a Shirley-type background to remove most of the extrinsic loss structure.

3.2.2.5 Elemental Analysis (EA)

Carbon and hydrogen content were measured using a Carlo Erba (Thermo Scientific) EA1108 Elemental Analyzer CHNS-O equipped with Eager Xperience software.

3.2.2.6 Transmission Electron Microscopy (TEM)

TEM was performed using a JEOL 2010 Transmission Electron Microscope with a LaB_6 thermionic emission filament operated at an accelerating voltage of 200 kV. The instrument was fitted with an Energy Dispersive X-Ray Spectroscopy (EDS) detector for elemental analysis. TEM samples were prepared by dip-coating carbon-coated, 200-mesh Cu grids (SPI Supplies) in DMF or ethanol suspensions.

3.2.2.7 Raman Spectroscopy

Raman spectra were measured on samples drop-coated from ethanol suspension on gold-coated glass slides. Spectra were acquired using a Renishaw In Via Raman Miscoscope equipped with an Argon ion laser (514 nm, 1800 l/mm (vis)) and a CCD detector (laser power 4.32 mW at 20x magnification). The spectral range was set static around 300 cm^{-1}, acquisition time was 10 s with 3 accumulations.

3.3 Results and Discussion

In this study, we investigated the influence of hydride-substituents on the thermal decomposition of molecular *n*-butylgermanes (nBu$_x$GeH$_{4-x}$ (x = 1-4)). Under appropriate conditions, hot injection of *n*-butylgermanes is expected to yield Ge-NCs, as has been previously shown for tetra-*n*-butylgermane.[21] Thermal decomposition forms elemental Ge, which nucleates and grows. Growth may be terminated by limiting the precursor supply, capping the surface with a ligand or decreasing the supplied (thermal) energy below a certain threshold. For tetra-*n*-butylgermane, elimination of the butyl-groups may proceed through radical or β-hydride elimination (*vide supra*). When hydride substituents are introduced (x = 1-3), reductive elimination also becomes possible. In this regard, as the number of hydride substituents increases, this process is expected to become more facile. Thus, we expect to see a decrease in decomposition temperature with decreasing x as we move through the nBu$_x$GeH$_{4-x}$ series.

3.3.1 Qualitative Determination of Decomposition Temperatures

The hypothesis regarding the decrease of decomposition temperatures through the series nBu$_x$GeH$_{4-x}$ (x = 1-4) with decreasing x was investigated by performing hot injection studies of nBu$_x$GeH$_{4-x}$ (x = 1-3). The precursors were injected into octacosane at different reaction temperatures, and reacted for 30 min. The first set of experiments yielded qualitative information about the

decomposition temperatures of nBu$_x$GeH$_{4-x}$ (x = 1-3). In our previous solid-state studies (see Chapter 2), we determined decomposition temperatures of $(RGeO_{1.5})_n$ through thermogravimetric analysis (TGA), however nBu$_x$GeH$_{4-x}$ (x = 1-3) are volatile liquids at room temperature, precluding this type of analysis. For nBu$_4$Ge, a decomposition temperature of 390 °C has been previously reported.[21] Expecting lower decomposition temperatures for nBu$_x$GeH$_{4-x}$ (x = 1-3), we began our investigation at 350 °C. The change from colourless to dark brown solutions during reaction indicated precursor decomposition. In further experiments, the injection temperature was consecutively decreased by 10 °C until a colourless solution was obtained (Figure 3.4). This allowed us to place the decomposition temperatures of nBu$_x$GeH$_{4-x}$ (x = 1-3) within 10 °C intervals centered around 285 °C for nBuGeH$_3$, 305 °C for nBu$_2$GeH$_2$ and 325 °C for nBu$_3$GeH (Figure 3.5).

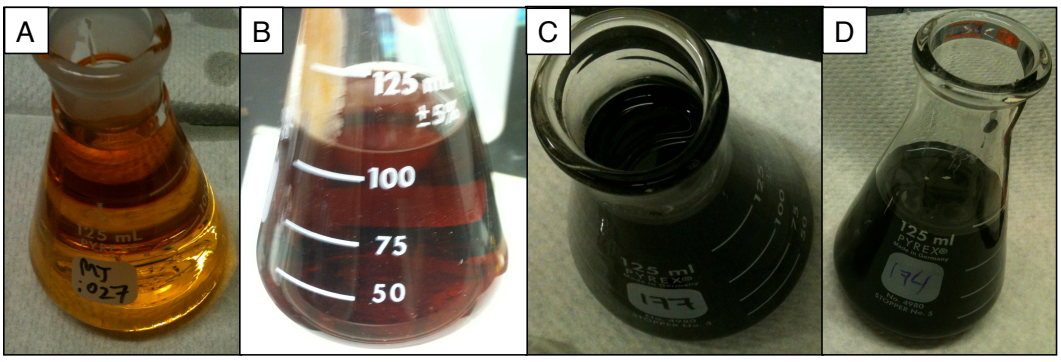

Figure 3.4. Photographs of hot injection products in octacosane and toluene from reactions of nBu$_2$GeH$_2$ at (A) 325 °C, (B) 340 °C, (C) 350 °C, and (D) 400 °C.

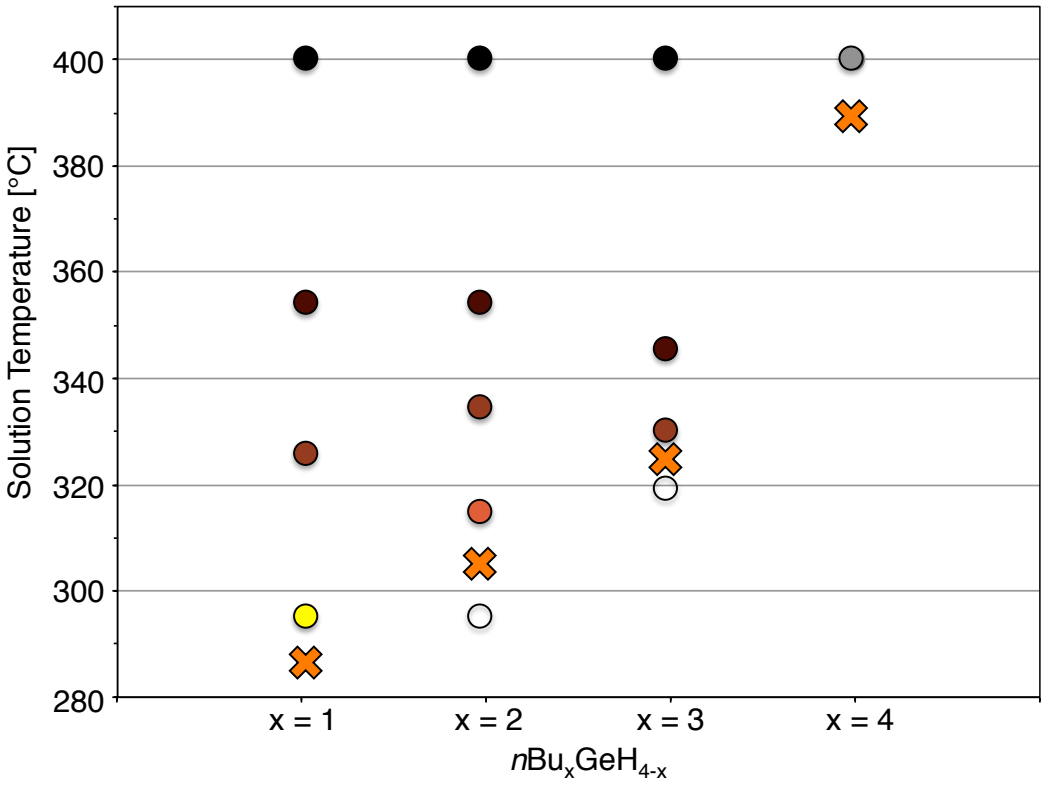

Figure 3.5. Experimental series qualitatively estimating nBu$_x$GeH$_{4-x}$ (x = 1, 2, 3) decomposition temperatures (marked by orange ×) in hot injection experiments. nBu$_4$Ge was placed according to ref. 21. The coloured dots indicate the colour of solutions or suspensions obtained at the indicated temperatures.

3.3.2 Hot Injection at High Temperature (400 °C)

The decomposition of nBu$_x$GeH$_{4-x}$ (x = 1-4) was then investigated at high temperature (400 °C) for 30 min. In this set of experiments, we were interested in differences in morphology and size of the obtained nanomaterials based on their different precursor decomposition temperatures. Based on the magnitude of Δ (Δ = $T_{experiment}$ - $T_{decomposition}$), decomposition is expected to proceed at different rates, affecting the solution concentration of Ge and thus nucleation and growth of Ge nanoparticles. The experiment yielded black suspensions for nBu$_x$GeH$_{4-x}$ (x = 1

(**1**), x = 2 (**2**), x = 3 (**3**)), and a grey suspension with substantially less precipitate for *n*Bu_4Ge (**4**) (Figure 3.6).

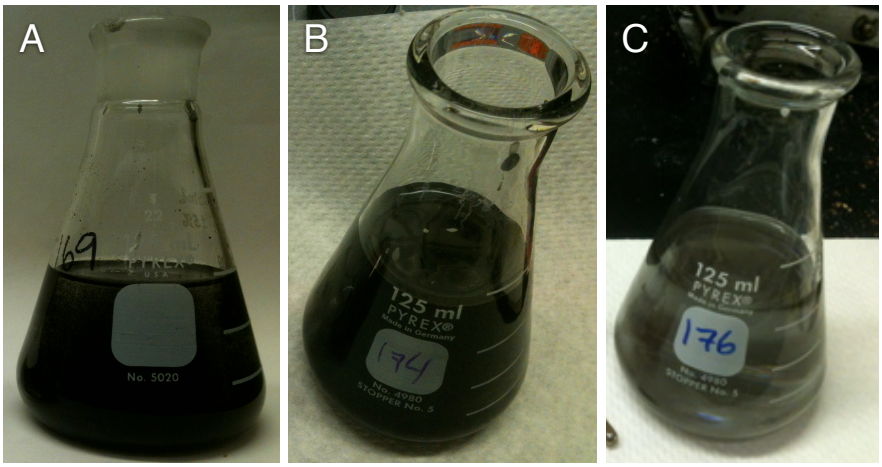

Figure 3.6. Photographs of products (A) **1**, (B) **3**, and (C) **4** obtained from hot injection of (A) *n*$BuGeH_3$, (B) *n*Bu_3GeH, and (C) *n*Bu_4Ge in octacosane at 400 °C and dispersed in toluene (prior to workup). **2** was macroscopically comparable to **1** and **3**.

Transmission electron microscopy (TEM) together with energy-dispersive X-ray spectroscopy (EDS) confirmed the formation of nanoparticles of germanium. The majority of the products were observed in large agglomerates or aggregates, not as freestanding particles (Figure 3.7). This lack of particle dispersibility is an indication of no (or insufficient) surface functionalization. Radical reactions of octacosane or butane with the Ge surface at the high reaction temperature, as well as incomplete removal of butyl-groups could lead to surface functionalization, however we did not purposefully add a surface capping agent to

the reaction. Surface functionalization would impart solubility and possibly oxidative stability to Ge-NPs, and should be investigated in the future.

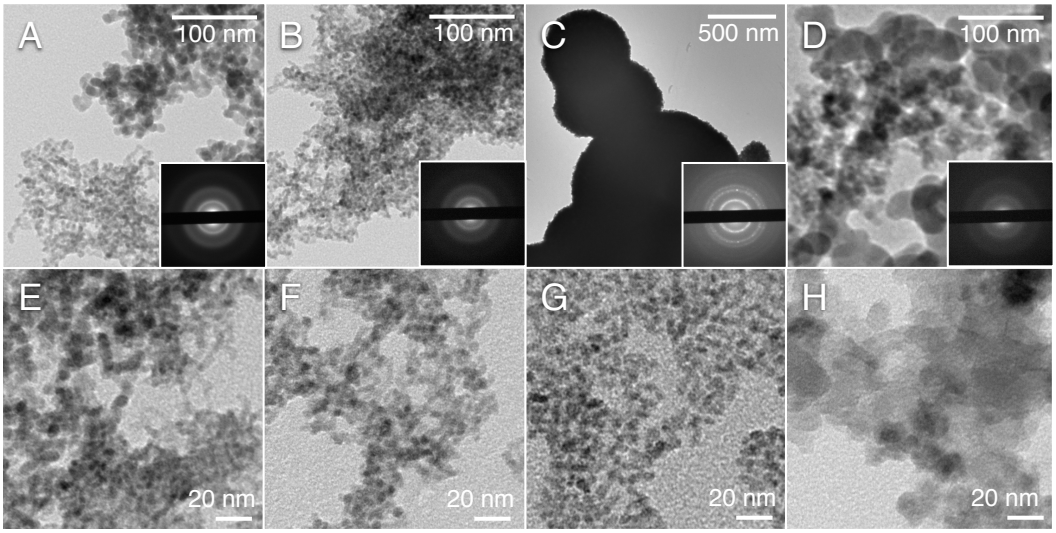

Figure 3.7. Transmission electron micrographs of **1** (A, E), **2** (B, F), **3** (C, G), and **4** (D, H), from thermal decomposition of (A, E) nBuGeH$_3$, (B, F) nBu$_2$GeH$_2$, (C, G) nBu$_3$GeH, and (D, H) nBu$_4$Ge at 400 °C. The insets in images A-D are selected area electron diffraction (SAED) patterns of **1-4**, respectively.

Further, the sizes observed in TEM are of interest to us. We observe a decrease in average nanoparticle size when Δ is large (x = 1-3, Figure 3.7, A, B, E-G). In the LaMer model, it is established that smaller, less polydisperse nanoparticles are obtained from burst nucleation, in which all particles nucleate at the same time and the precursor remaining for growth is limited. This condition is more easily met when Δ is large, and decomposition occurs quickly. In the case of nBu$_4$Ge (**4**), for which Δ = 10 °C, very little precipitate was recovered, suggesting incomplete decomposition. Aggregates appear to be made up of poorly defined

particles with varying sizes and shapes, and it was not possible to carry out detailed size analysis of this sample (Figure 3.7.D, H). Figure 3.7.H shows more clearly the presence of very large, oblong, and curved particles. These may be formed due to growth occurring for an extended period of time, as the precursor slowly decomposes. For nBu$_3$GeH (**3**), for which $\Delta \approx 75$ °C, we observed very large aggregates (Figure 3.7.C). The strong contrast suggests the aggregates are made up of large spheres, in contrast to the seemingly flat particle assemblies with low thickness contrast shown in the other images. When taking a closer look at the edges of the aggregates in Figure 3.7.C, roughness becomes apparent. This roughness may suggest the aggregates are composed of smaller particles (Figure 3.7.G). Particle sizes were determined for aggregates such as shown in Figure 3.7.G, and have an average diameter of 5.2 nm, with a reasonably narrow size distribution and standard deviation of 1.5 nm (Figure 3.8.C). However, aggregation made size analysis challenging and results are given as comparative values, not as absolute measurements. As we increase Δ further, we observe a slight increase in the width of particle size distributions. For nBu$_2$GeH$_2$ (**2**), for which $\Delta \approx 95$ °C, all aggregates appear to consist of nanoparticles with an average size of 7 nm (Figure 3.7.B, Figure 3.8.B). In contrast to **3**, there is a larger number of small as well as large NPs, broadening the size distribution (Figure 3.7.F, Figure 3.8.B). For the largest Δ of 115 °C, *i.e.,* the decomposition of nBuGeH$_3$ (**1**), the aggregate shown in Figure 3.7.A suggests larger particles are present in the top half of the image, while the bottom half of the image shows an aggregate of substantially smaller nanoparticles. Size analysis of particles in these

aggregates does not yield a bimodal size distribution, as was initially expected from Figure 3.7.A. Rather, just as in **2**, larger numbers of both smaller and larger NPs are observed in contrast to **3** (Figure 3.8.A). Ostwald ripening (*vide supra*) may be the cause of the broader size distributions in **1** and **2**. It is possible that Δ is now so large that the initial growth period is very fast. At 30 min reaction time, this may allow enough time for particle growth to proceed into the defocussing regime, which follows the initial size distribution focussing regime generally observed in particle growth.[60,69,70]

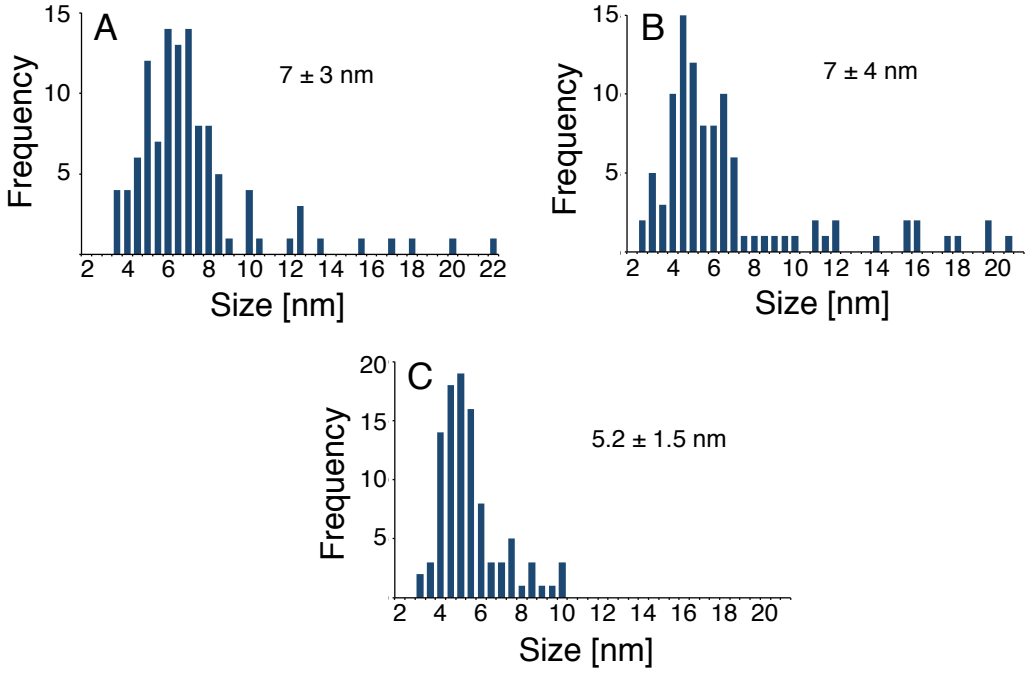

Figure 3.8. Size analysis of aggregated particles observed in TEM imaging of (A) **1**, (B) **2**, and (C) **3**. The analysis is based on measurement of ≥100 particles.

The crystallinity of materials was evaluated using selected area electron diffraction (SAED). For samples **1**, **2** and **4** only very diffuse rings matching the Ge diffraction pattern were observed, while **3** exhibited spots corresponding to different orientations of Ge-NCs (insets, Figure 3.7). In comparison to other work, the intensities of diffraction spots and rings are too weak and diffuse for the material to be crystalline,[71] which is confirmed by amorphous patterns in X-ray diffraction experiments (*vide infra*).

X-ray photoelectron spectroscopy (XPS) confirmed the formation of elemental Ge (~29 eV) for **1-3** (Figure 3.9).[72] The presence of a second signal at higher binding energies is attributed to oxidation, consistent with a broad, weak- to medium-intensity stretch at 760-800 cm^{-1} in FT-IR that may be assigned to Ge-O-Ge stretching.

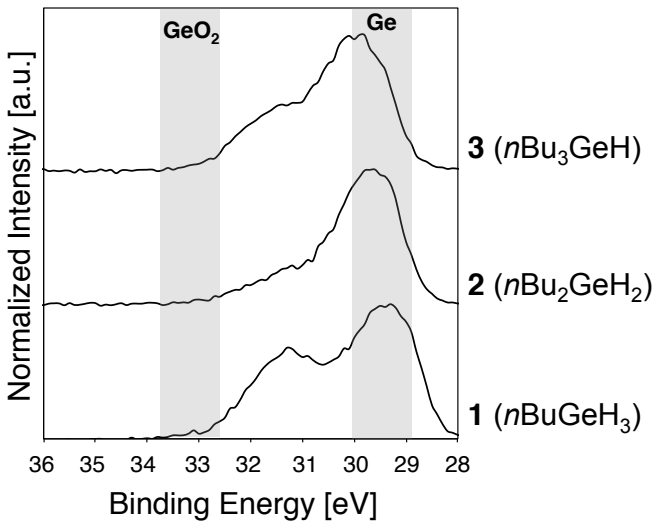

Figure 3.9. High-resolution X-ray Photoelectron Spectra of the Ge 3d region for samples **1-3**.

Bulk crystallinity of the materials obtained was investigated by X-ray powder diffraction (XRD). The patterns shown in Figure 3.10 show extremely broad reflections that are roughly centered on the angles at which diamond-structure Ge would appear (compare **1-3** to Ge standard, Figure 3.10). Broad peaks are an indication of nanocrystalline materials, however, the breadth of these peaks is so large that (220) and (311) are merged into one broad signal. This signal does not show the shoulder that would be expected for a broad signal made up from two underlying reflections. Comparing these patterns to previous literature reports, we conclude that the obtained materials are in fact not crystalline, but amorphous.[21,73] This is also confirmed by Scherrer analysis of the (111) reflection, which gives crystalline domain sizes of about 1.5 nm for these samples. Upon comparison with the sizes measured in TEM, this observation suggests that the particles are not single-crystalline.

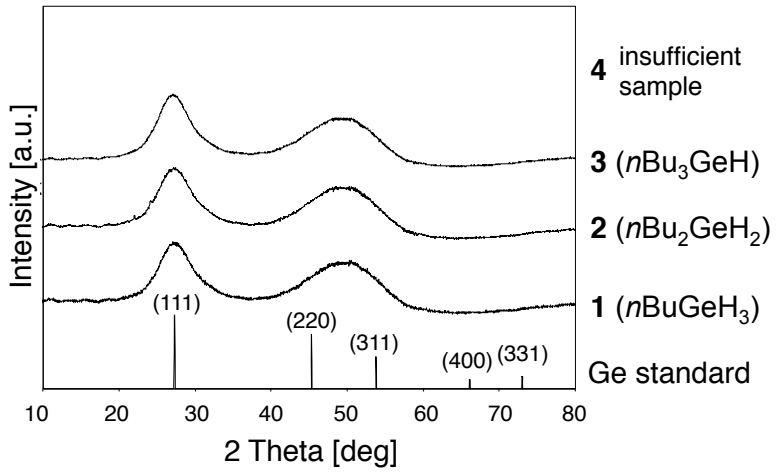

Figure 3.10. X-ray powder diffraction patterns of solids **1-3** obtained from hot injection at 400 °C. The yield of **4** (from nBu$_4$Ge) was insufficient for XRD.

Material purity and surface termination were assessed by infrared spectroscopy (FT-IR), elemental analysis (EA) and thermogravimetric analysis (TGA). The presence of alkyl-groups is apparent from C-H stretching vibrations around 2800-3000 cm^{-1} in FT-IR, consistent with the observation of a CH content of 12% (**1**), 13% (**2**), and 6% (**3**) in EA. In the case where these alkyl-groups would be bonded to the Ge surface, a difference in the onset temperature of mass loss in TGA compared to the parent alkane would be expected. Comparing the TGA data for **1-3** with that of octacosane, we note the onset temperature of mass loss is ~70-130 °C higher for **1-3** than for pure octacosane (Figure 3.11). The onset temperatures for **1-3** are in the same range as the onset temperatures for alkyl chain loss in TGA of $(RGeO_{1.5})_n$ (see Chapter 2, Table 2.2). However, this may also be an effect of mixing in solids, leading to a boiling point elevation.

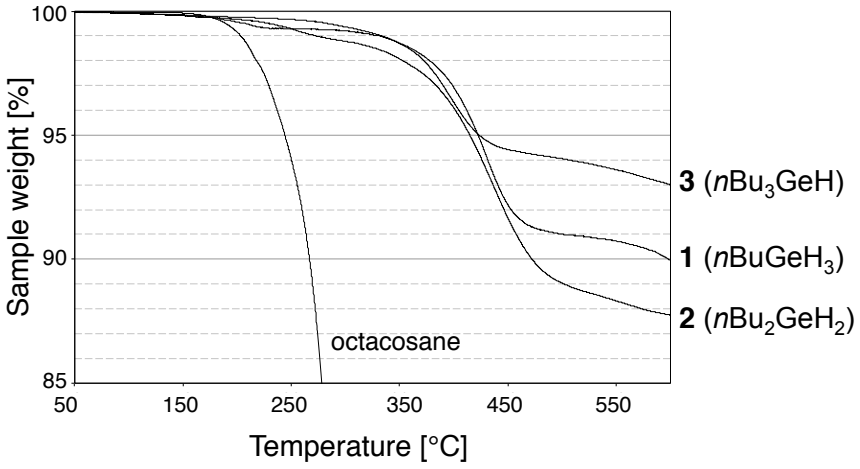

Figure 3.11. Thermogravimetric analysis (TGA) of pure octacosane and samples **1-3** from hot injection at 400 °C.

3.3.3 Hot Injection at Lower Temperature (325 °C)

The injection temperature of octacosane was reduced to 325 °C to investigate decomposition products formed closer to the decomposition temperatures of the $n\text{Bu}_x\text{GeH}_{4-x}$ (x = 1-3) precursors. Since the reaction temperature is well below the decomposition temperature of $n\text{Bu}_4\text{Ge}$ (390 °C), this precursor was excluded from further study. Also, lower reaction temperature enables the use of different solvents and additives, such as surfactants, with boiling points below 400 °C.

Though Δ was again of different magnitudes for the different precursors (~40 °C for x = 1, ~20 °C for x = 2, and ~0 °C for x = 3), the macroscopic appearance of products was similar (Figure 3.12). All precursors yielded deep red-brown colloidal solutions exhibiting a Tyndall effect when laser light was shone through the samples. Over a period of weeks, no precipitate settled out of solution, showing good colloidal stability.

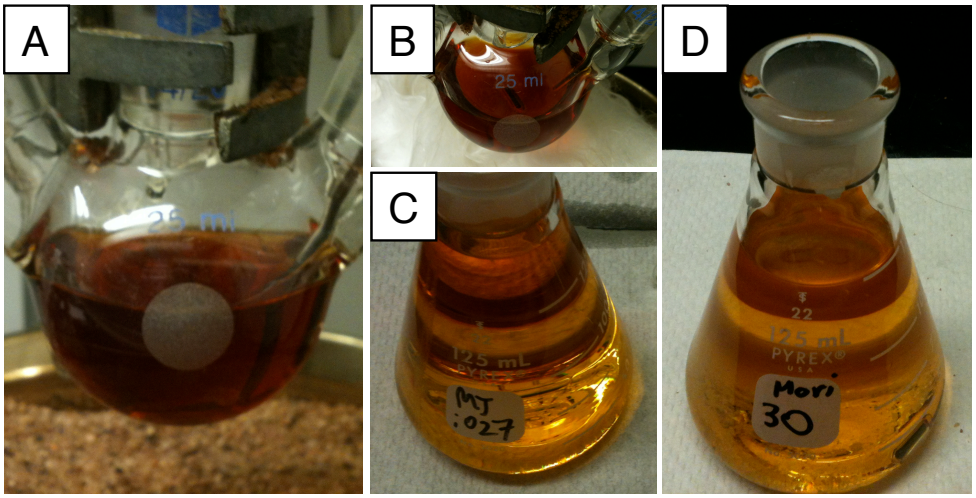

Figure 3.12. Photograph after hot injection in octacosane at 325 °C and 30 min reaction of (A) nBuGeH$_3$ (**5**), (B) nBu$_2$GeH$_2$ (**6**), (C) nBu$_2$GeH$_2$ reaction mixture in toluene (**6**), and (D) nBu$_3$GeH reaction mixture in toluene (**7**).

In TEM analysis of the isolated precipitates, differences between samples are not as pronounced as was observed at 400 °C injection temperature. All samples contain aggregates of larger Ge particles, with sizes of ~50-100 nm (Figure 3.13.A, B, C). However, the presence of small nanoparticles (<< 20 nm) is also noted (Figure 3.13.D, E, F). The poor contrast of these samples, which is attributed both to the small size of nanoparticles as well as to the presence of impurities (*e.g.*, octacosane), complicates rigorous size analysis. EDS confirmed the presence of Ge and O, next to Cu and C from the carbon-coated TEM grid. Sample sizes were insufficient for bulk XRD analysis, but SAED patterns consisted of diffuse rings characteristic of amorphous Ge. Since crystallinity was not consistently observed after injection at 400 °C, this result is in line with our expectations.

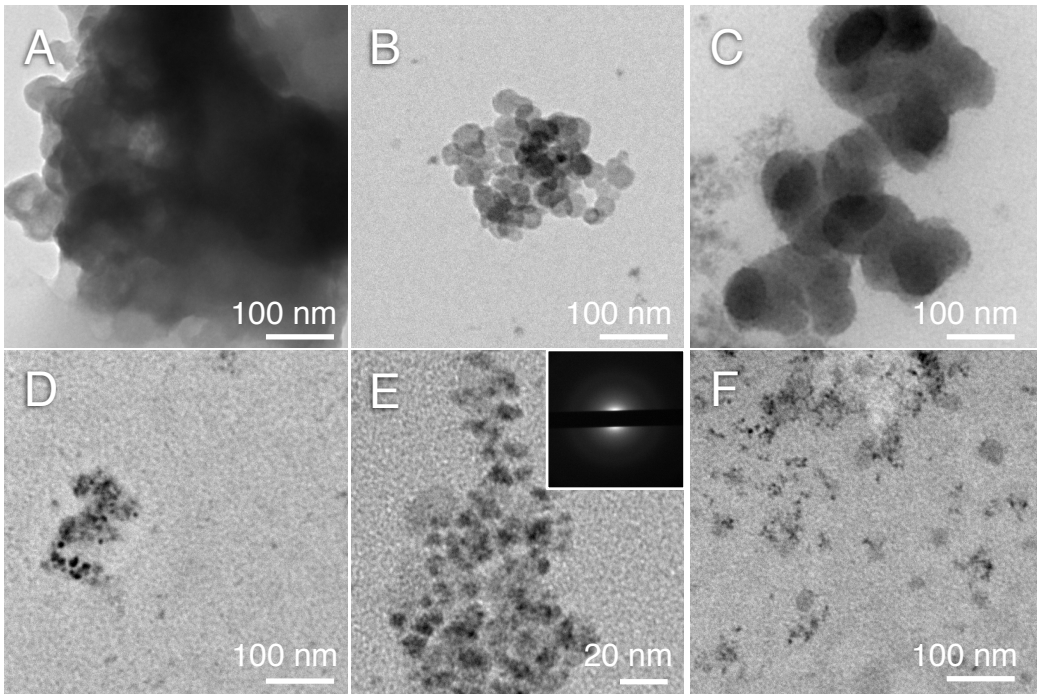

Figure 3.13. TEM images of samples **5** (A, D), **6** (B, E), and **7** (C, F) obtained from hot injection of (A, D) *n*$BuGeH_3$, (B, E) *n*Bu_2GeH_2, (C, F) *n*Bu_3GeH in octacosane at 325 °C.

XPS confirmed the presence of elemental Ge in samples that had been exposed to atmosphere for less than a day (Figure 3.14, **5**). Once samples are stored for a few days, substantial oxidation is observed (Figure 3.14, **6** and **7**). Along with the observation of aggregates in TEM, this is an indication of the instability of the particle surface.

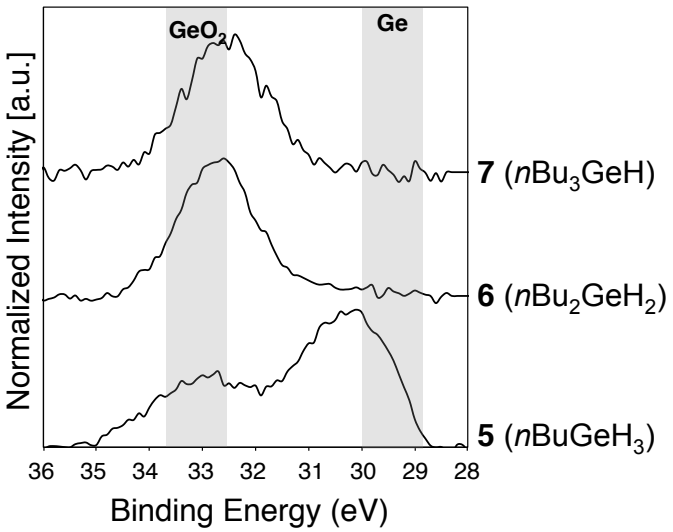

Figure 3.14. High-resolution XPS of the Ge 3d region for samples **5-7** synthesized by hot injection in octacosane at 325 °C. The absence of low-oxidation state Ge in **6** and **7** is attributed to exposure to air over a period of one week in contrast to sample **5**, which was only exposed to air for hours, showing the limited oxidative stability of the products.

Oxidation is also evident from FT-IR data showing Ge-O-Ge stretching at *ca.* 800 cm^{-1}, similar to that observed for **1**-**4**. Alkyl C-H stretching vibrations point towards remaining octacosane impurities, though sample sizes were insufficient to determine CH content and evaluate the thermogravimetric behaviour of these samples.

From this series of experiments, it is evident that Ge-NPs are also formed at these lower temperatures. As expected, the obtained material is also non-crystalline, and shows no evidence of surface protection. In a final set of experiments, we thus began investigating coordinating solvents for the purpose of surface stabilization.

3.3.4 Hot Injection at Lower Temperature (325 °C) in Trioctylamine (TOA)

To investigate if reaction in a coordinating solvent will improve the stability of Ge nanomaterials produced by hot injection of $n\text{Bu}_x\text{GeH}_{4-x}$ (x = 1-3), we examined hot injection in trioctylamine (TOA). To maintain comparability to the previous experiments in octacosane, reactions were carried out at 325 °C for 30 min.

Macroscopically, there are clear differences to the products obtained under identical conditions in octacosane (Figure 3.15). For the different precursors, different coloured suspensions or colloidal solution were obtained: **8** (from $n\text{BuGeH}_3$) formed a dark brown suspension, **9** (from $n\text{Bu}_2\text{GeH}_2$) a red-brown suspension, and **10** (from $n\text{Bu}_3\text{GeH}$) a faint yellow colloidal solution. The terms "suspension" and "colloidal solution" are used here to differentiate between a colloidal solution immediately settling out a precipitate (suspension) and a stable colloidal solution that requires centrifugation in the presence of an antisolvent to separate the colloid (*i.e.*, the nanoparticles). In a first set of experiments, the isolated precipitate was observed to lose colour and even turn white over a period of days, which was attributed to Ge-NP oxidation (GeO_2 is a white powder). Further reactions were treated as air-sensitive and stored in a glovebox immediately after centrifugation, and washing steps were completed with dry solvents.

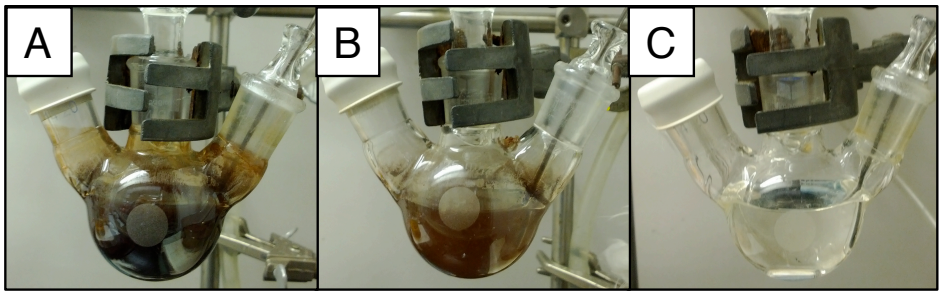

Figure 3.15. Photographs of samples **8** (A), **9** (B), and **10** (C) immediately after hot injection of (A) nBuGeH$_3$, (B) nBu$_2$GeH$_2$, (C) nBu$_3$GeH in trioctylamine at 325 °C.

In TEM analyses, residual TOA was still visibly present after washing the samples with ethanol thrice. The presence of TOA was evidenced by the observation of micelles that were unstable towards prolonged exposure to the electron beam. Micelles can be seen surrounding aggregates in Figure 3.16. B and C (some are indicated by white arrows), and TOA forms the background in Figure 3.16.A.

Very few large Ge particles were observed in all samples synthesized in TOA, so that these were deemed non-representative of the sample. Generally, an increase in particle size was observed with increasing x in nBu$_x$GeH$_{4-x}$ (corresponding to increasing decomposition temperature and decreasing Δ). Figure 3.16.A shows well dispersed, small nanoparticles (~2-5 nm) from decomposition of nBuGeH$_3$ (**8**). In contrast, samples from decomposition of both nBu$_2$GeH$_2$ (**9**) and nBu$_3$GeH (**10**) displayed Ge-NPs in aggregates, as was previously observed in octacosane. Taking a close look at Figure 3.16.B, many different particle sizes become evident in **9**. The aggregate at the bottom left is

made up of large, oblong particles (~20-35 nm) such as those observed in samples **4** and **7**. The aggregate at the bottom right consists of smaller, pseudospherical particles (~10-15 nm), while the faint aggregate at the top displays even smaller particles (~4-9 nm). Aggregates in **10** consist of pseudospherical particles of ~10-25 nm diameter (Figure 3.16.C).

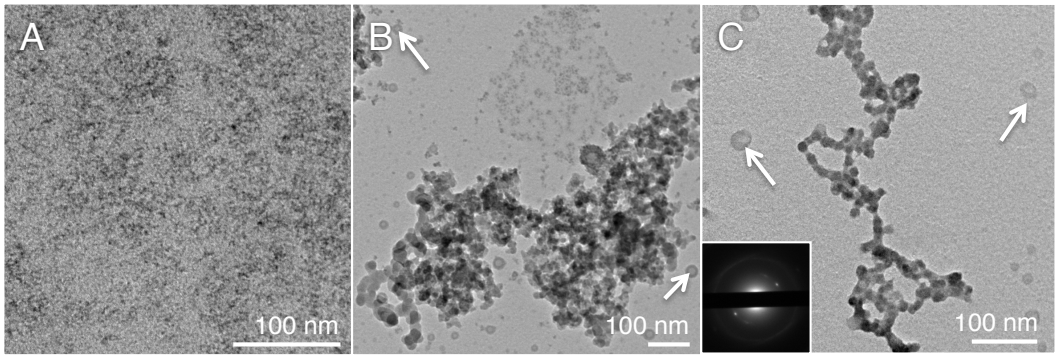

Figure 3.16. TEM images of (A) **8**, (B) **9**, and (C) **10** from hot injection of (A) nBuGeH$_3$, (B) nBu$_2$GeH$_2$, (C) nBu$_3$GeH in trioctylamine at 325 °C. White arrows indicate the observation of very beam-sensitive material, which is likely trioctylamine impurity.

XPS of samples exposed to air for two days confirmed the assumption that oxidation was taking place (*vide supra*, Figure 3.17, **8**). In line with this, we observe Ge-O-Ge stretching in FT-IR of samples after extended exposure to atmosphere. XPS of samples that were stored in a glovebox showed the presence of elemental Ge (Figure 3.17, **9**).

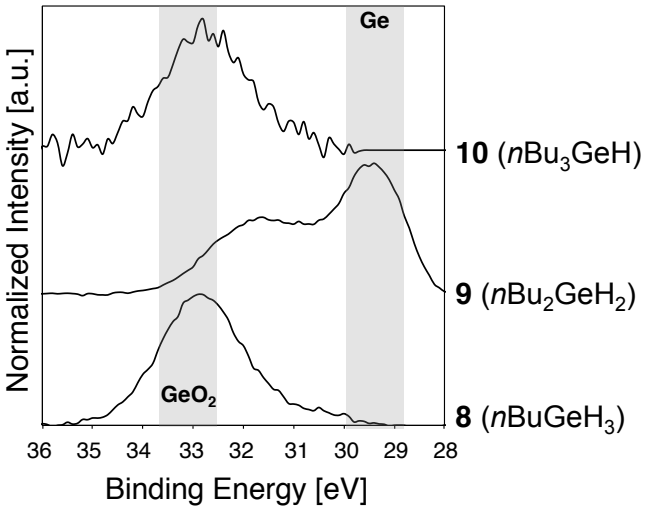

Figure 3.17. XPS of the Ge 3d region for samples **8**-**10** synthesized by thermal decomposition at 325 °C in trioctylamine.

Raman confirmed the presence of Ge-Ge bonding by the observation of the characteristic phonon signal at ~300 cm^{-1} (Figure 3.18). The broad, asymmetric base extending to lower wavenumbers can be attributed to strain, poor crystallinity and/or small particle size,[74,75] the latter two being in accordance with TEM and SAED analysis of **9**.

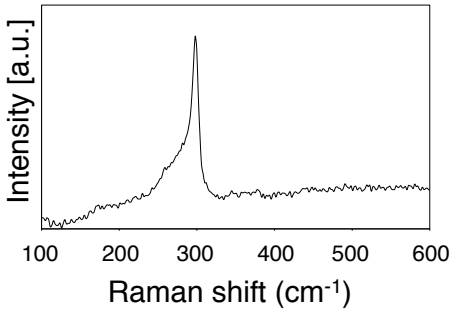

Figure 3.18. Representative Raman spectrum of sample **9**, showing the Ge-Ge phonon around 300 cm^{-1}.

In summary, the presence of a weakly coordinating tertiary amine is not sufficient to achieve surface termination that imparts size control and oxidative stability. However, size control may also be impacted by the relatively long reaction time, a factor that will be investigated in the future. TOA was able to impart better dispersibility in comparison to samples obtained from octacosane, though this may simply be due to the amphiphilic surfactant-like nature of the amine in contrast to hydrophobic octacosane.

3.4 Conclusions and Future Work

The substituent groups of compounds used in thermal decomposition influence their reactivity profoundly. In the series of $n\text{Bu}_x\text{GeH}_{4-x}$ (x = 1-4), we observe an overall change in decomposition temperature of ~100 °C from ~285 °C in $n\text{BuGeH}_3$ to 390 °C in $n\text{Bu}_4\text{Ge}$. All precursors form Ge-NPs upon decomposition, no growth of nanowires, as observed in other studies, was noted.[21]

Ge-NPs synthesized by hot injection of $n\text{Bu}_x\text{GeH}_{4-x}$ (x = 1-4) in octacosane show poor oxidative stability and poor solubility. Synthesis in the weakly coordinating solvent trioctylamine (TOA) was able to improve solubility, however, oxidation still occurs. None of the synthesized materials showed photoluminescence. $n\text{BuGeH}_3$, with its low decomposition temperature and small, well dispersed NPs (from synthesis in TOA) is the precursor of choice for further study.

Future work on hot injection of $n\text{BuGeH}_3$ should address stability of the Ge-NP surface as well as crystallinity of the obtained materials. Once these factors have been addressed, decomposition time and temperature should be studied in detail to explore the ability of size and shape tailoring of nanomaterials in this synthetic method.

3.5 References

(1) Maeda, Y.; Tsukamoto, N.; Yazawa, Y.; Kanemitsu, Y.; Masumoto, Y. *Appl. Phys. Lett.* **1991**, *59*, 3168–3170.

(2) Kaur, I.; Jia, W.; Kopreski, R. P.; Selvarasah, S.; Dokmeci, M. R.; Pramanik, C.; McGruer, N. E.; Miller, G. P. *J. Am. Chem. Soc.* **2008**, *130*, 16274–16286.

(3) Roos, B. O.; Andersson, K.; Fülscher, M. P. *Chem. Phys. Lett.* **1992**, *192*, 5–13.

(4) Brus, L. *IEEE J. Quantum Electron.* **1986**, *QE-22*, 1909–1914.

(5) Macfarlane, G.; McLean, T. P.; Quarrington, I. E.; Roberts, V. *Phys. Rev.* **1957**, *108*, 1377–1383.

(6) Gaponenko, S. V. *Optical Properties of Semiconductor Nanocrystals*; Cambridge University Press, 1998.

(7) Wu, J.; Sun, Y.; Zou, R.; Song, G.; Chen, Z.; Wang, C.; Hu, J. *Cryst. Eng. Comm.* **2011**, *13*, 3674–3677.

(8) Taylor, B. R.; Kauzlarich, S. M.; Delgado, G. R.; Lee, H. W. H. *Chem. Mater.* **1999**, *11*, 2493–2500.

(9) Chou, N. H.; Oyler, K. D.; Motl, N. E.; Schaak, R. E. *Chem. Mater.* **2009**, *21*, 4105–4107.

(10) Henderson, E. J.; Hessel, C. M.; Veinot, J. G. C. *J. Am. Chem. Soc.* **2008**, *130*, 3624–3632.

(11) Wu, H. P.; Ge, M. Y.; Yao, C. W.; Wang, Y. W.; Zeng, Y. W.; Wang, L. N.; Zhang, G. Q.; Jiang, J. Z. *Nanotechnology* **2006**, *17*, 5339–5343.

(12) Taylor, B. R.; Kauzlarich, S. M.; Lee, H. W. H.; Delgado, G. R. *Chem. Mater.* **1998**, *10*, 22–24.

(13) Wilcoxon, J.; Provencio, P.; Samara, G. *Phys. Rev. B* **2001**, *64*, 035417.

(14) Taylor, B. R.; Fox; Hope-Weeks, L. J.; Maxwell; Kauzlarich, S. M.; Lee *Mater. Sci. Eng., B* **2002**, *96*, 90–93.

(15) Tanke, R. S.; Kauzlarich, S. M.; Patten, T. E.; Pettigrew, K. A.; Murphy, D. L.; Thompson, M. E.; Lee, H. W. H. *Chem. Mater.* **2003**, *15*, 1682–1689.

(16) Lu, X.; Ziegler, K. J.; Ghezelbash, A.; Johnston, K. P.; Korgel, B. A. *Nano Lett.* **2004**, *4*, 969–974.

(17) Fok, E.; Shih, M.; Meldrum, A.; Veinot, J. G. C. *Chem. Commun.* **2004**, *1*, 386–387.

(18) Myung, N.; Lu, X.; Johnston, K. P.; Bard, A. J. *Nano Lett.* **2004**, *4*, 183–185.

(19) Hope-Weeks, L. J. *Chem. Lett.* **2005**, *34*, 1526–1527.

(20) Warner, J. H.; Tilley, R. D. *Nanotechnology* **2006**, *17*, 3745–3749.

(21) Zaitseva, N.; Dai, Z. R.; Grant, C. D.; Harper, J.; Saw, C. *Chem. Mater.* **2007**, *19*, 5174–5178.

(22) Lee, D. C.; Pietryga, J. M.; Robel, I.; Werder, D. J.; Schaller, R. D.; Klimov, V. I. *J. Am. Chem. Soc.* **2009**, *131*, 3436–3437.

(23) Ruddy, D. A.; Johnson, J. C.; Smith, E. R. R.; Neale, N. R. *ACS Nano*

2010, *4*, 7459–7466.
(24) Prabakar, S.; Shiohara, A.; Hanada, S.; Fujioka, K.; Yamamoto, K.; Tilley, R. D. *Chem. Mater.* **2010**, *22*, 482–486.
(25) Heath, J. R.; Shiang, J. J. *Chem. Soc. Rev.* **1998**, *27*, 65–71.
(26) Codoluto, S. C.; Baumgardner, W. J.; Hanrath, T. *Cryst. Eng. Comm.* **2010**, *12*, 2903–2909.
(27) Hoffman, M.; Veinot, J. G. C. *Chem. Mater.* **2012**, *24*, 1283–1291.
(28) Henderson, E. J.; Hessel, C. M.; Cavell, R. G.; Veinot, J. G. C. *Chem. Mater.* **2010**, *22*, 2653–2661.
(29) Hanrath, T.; Korgel, B. A. *J. Am. Chem. Soc.* **2002**, *124*, 1424–1429.
(30) Gerion, D.; Zaitseva, N.; Saw, C.; Casula, M. F.; Fakra, S.; Van Tony, B.; Galli, G. *Nano Lett.* **2004**, *4*, 597–602.
(31) Lu, X.; Korgel, B. A.; Johnston, K. P. *Nanotechnology* **2005**, *16*, S389–S394.
(32) Wang, W.; Poudel, B.; Huang, J. Y.; Wang, D. Z.; Kunwar, S.; Ren, Z. F. *Nanotechnology* **2005**, *16*, 1126–1129.
(33) Warner, J. H. *Nanotechnology* **2006**, *17*, 5613–5619.
(34) Boucham, J. E.; Maury, F.; Morancho, R. *J. Anal. Appl. Pyrolysis* **1998**, *44*, 153–165.
(35) Pola, J.; Parsons, J. P.; Taylor, R. *J. Chem. Soc. Faraday Trans.* **1992**, *88*, 1637–1641.
(36) Yang, H.-J.; Tuan, H.-Y. *J. Mater. Chem.* **2012**, *22*, 2215–2225.
(37) Glockling, F.; Hooton, K. A. *J. Chem. Soc.* **1963**, 1849–1854.
(38) Johnson, O. H.; Harris, D. M. *J. Am. Chem. Soc.* **1950**, *72*, 5564–5566.
(39) Luo, Y.-R.; Pacey, P. D. *Can. J. Chem.* **1993**, *71*, 572–577.
(40) Tannenbaum, S. *J. Am. Chem. Soc.* **1954**, *76*, 1027.
(41) Long, L. H.; Pulford, C. I. *J. Chem. Soc., Faraday Trans. 2* **1986**, *82*, 567–572.
(42) Bills, J. L.; Cotton, F. A. *J. Phys. Chem.* **1964**, *68*, 806–810.
(43) Carson, A. S.; Carson, E. M.; Laye, P. G.; Spencer, J. A.; Steele, W. V. *Trans. Faraday Soc.* **1970**, *66*, 2459–2463.
(44) Clark, K. B.; Griller, D. *Organometallics* **1991**, *10*, 746–750.
(45) Davidson, P. J.; Lappert, M. F.; Pearce, R. *Chem. Rev.* **1976**, *76*, 219–242.
(46) Wong, K.; McBurnett, B.; Culp, R.; Cowley, A.; Ekerdt, J. *Surf. Sci.* **1998**, *416*, 480–487.
(47) Maejima, K.; Kawabata, H.; Fujita, S. *Jpn. J. Appl. Phys.* **2008**, *47*, 1098–1100.
(48) Gordon, C.; Long, C. In *PATAI's Chemistry of Functional Groups*; John Wiley & Sons, Ltd, 2009.
(49) Levason, W.; Reid, G.; Zhang, W. *Coord. Chem. Rev.* **2011**, *255*, 1319–1341.
(50) Sergienko, V. S.; Minacheva, L. K.; Churakov, A. V. *Russ. J. Inorg. Chem.* **2010**, *55*, 2001–2030.
(51) Keeling, L.; Chen, L.; Greenlief, C. *Surf. Sci.* **1998**, *400*, 1–10.
(52) Ryan, C.; Lewis, A. K. de K.; Caddick, S.; Kaltsoyannis, N. *Theor.*

Chem. Acc. **2011**, *129*, 303–312.
(53) Ghosh, R.; Emge, T. J.; Krogh-Jespersen, K.; Goldman, A. S. *J. Am. Chem. Soc.* **2008**, *130*, 11317–11327.
(54) Culkin, D.; Hartwig, J. *Organometallics* **2004**, *23*, 3398–3416.
(55) Pérez-Rodríguez, M.; Braga, A. A. C.; Garcia-Melchor, M.; Pérez-Temprano, M. H.; Casares, J. A.; Ujaque, G.; de Lera, A. R.; Álvarez, R.; Maseras, F.; Espinet, P. *J. Am. Chem. Soc.* **2009**, *131*, 3650–3657.
(56) Low, J. J.; Goddard, W. A. *Organometallics* **1986**, *5*, 609–622.
(57) Bartlett, K.; Goldberg, K.; Borden, W. *J. Am. Chem. Soc.* **2000**, *122*, 1456–1465.
(58) Rempel, J. Y.; Bawendi, M. G.; Jensen, K. F. *J. Am. Chem. Soc.* **2009**, *131*, 4479–4489.
(59) Robb, D. T.; Privman, V. *Langmuir* **2008**, *24*, 26–35.
(60) Talapin, D. V.; Rogach, A. L.; Haase, M.; Weller, H. *J Phys Chem B* **2001**, *105*, 12278–12285.
(61) Volmer, M.; Weber, A. *Z. Phys. Chem.* **1926**, *119*, 277–301.
(62) Becker, R.; Döring, W. *Ann. Phys.* **1935**, *416*, 719–752.
(63) LaMer, V. K.; Dinegar, R. H. *J. Am. Chem. Soc.* **1950**, *72*, 4847–4854.
(64) Ostwald, W. *Z. Phys. Chem.* **1901**, *37*, 385–390.
(65) Lifshitz, I. M.; Slyozov, V. V. *J. Phys. Chem. Solids* **1961**, *19*, 35–50.
(66) Wagner, C. *Z. Elektrochem.* **1961**, *65*, 581–591.
(67) (null) Canadian Climate Normals 1971-2000, Edmonton City Centre http://www.climate.weatheroffice.gc.ca (accessed Jul. 2012).
(68) Provost, E.; Chevallier, V.; Bouroukba, M.; Petitjean, D.; Dirand, M. *J. Chem. Eng. Data* **1998**, *43*, 745–749.
(69) Park, J.; Joo, J.; Kwon, S. G.; Jang, Y.; Hyeon, T. *Angew. Chem. Int. Ed.* **2007**, *46*, 4630–4660.
(70) Peng, X.; Wickham, J.; Alivisatos, A. P. *J. Am. Chem. Soc.* **1998**, *120*, 5343–5344.
(71) Vaughn, D. D., II; Bondi, J. F.; Schaak, R. E. *Chem. Mater.* **2010**, *22*, 6103–6108.
(72) *http://srdata.nist.gov/xps*.
(73) Ma, X.; Wu, F.; Kauzlarich, S. M. *J. Solid State Chem.* **2008**, *181*, 1628–1633.
(74) Das, S.; Singha, R. K.; Manna, S.; Gangopadhyay, S.; Dhar, A.; Ray, S. K. *J. Nanopart. Res.* **2011**, *13*, 587–595.
(75) Bottani, C. E.; Mantini, C.; Milani, P.; Manfredini, M.; Stella, A.; Tognini, P.; Cheyssac, P.; Kofman, R. *Appl. Phys. Lett.* **1996**, *69*, 2409–2411.

Chapter 4:

Metal-decorated iron/iron oxide core-shell nanoparticles as recoverable catalyst systems

A version of this chapter has been published:

Zhou, S.; Johnson[§], M.; Veinot, J. G. C. Chem. Commun. ***2010*** *46, 2411-2413.*

The author's contribution to this work includes all samples of Heck and some Suzuki chemistry reported here, as well as X-ray photoelectron spectroscopy data analysis and transmission electron microscopy of all samples.

[§] Thesis author's maiden name

4.1. Introduction

Nanoparticle (NP) catalysis is a burgeoning field of research, demonstrated by the exponential growth of publications pertaining to this field over the last decade (Figure 4.1).[1] NP catalysis is particularly promising with respect to industrial applications: NP catalysts may combine the recoverability of heterogeneous catalysts with high activity and selectivity that are usually associated with homogeneous catalyst systems.[1,2]

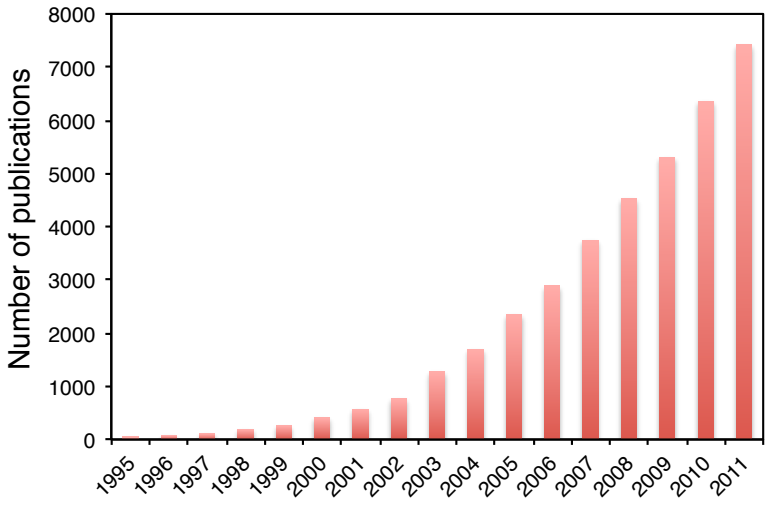

Figure 4.1. Publications on nanoparticle catalysis from 1995 to 2011, adapted from ref. 1. (SciFinder search "nanoparticle and catalysis", duplicates removed.)

The term "NP catalyst" encompasses a gamut of very different materials, ranging from unsupported metal NPs to NPs dispersed on a support material (*e.g.*, carbon nanomaterials, oxide surfaces) to homogeneous catalyst complexes tethered to a solid support (*e.g.*, Rh or Pd complexes tethered to magnetic NPs).[3-6]

As such, their recoverability, catalytic activity and selectivity arise from different structural features. Generally, recoverability of NP catalysts originates from their heterogeneous nature, rendering them amenable to filtration. Additionally, magnetic NP supports have been widely studied for improved recovery of catalysts using a magnet for catalyst separation.[7-10] For NP-supported homogeneous catalysts, high activity and selectivity are caused by the homogeneous nature of the catalytic metal surrounded by traditional organic ligands tethered to a NP surface. However, in the case of metal NPs or NP-supported metal clusters high catalytic activity and selectivity are frequently connected to their high surface-to-volume ratio.[3,6,11] Nanomaterials have a higher proportion of atoms residing at their surface, where catalysis may occur through adsorption of a substrate molecule. Beyond particle composition and oxidation states, particle shape, faceting, and the high surface curvature of NPs are also often credited as causes of high catalytic activity and selectivity.[2,12] The high surface energy, different facets and many step edges generate many more reactive sites than observed on a bulk surface.

Researchers are also investigating cooperative catalysis between two different metals or metal and support material, leading to the development of multimetallic catalyst systems in which reactivity is dictated by different adsorptive or reactive properties of adjacent metals.[13,14] For example, Cu-Pd-Ru was found through a combinatorial approach to be a good catalyst for Heck reactions.[15] The most commonly studied reactions in NP catalysis include simple

redox processes and cross-couplings such as the Heck and Suzuki reaction, however more complex reactions are increasingly under investigation.[1,2,15]

4.1.2. Heck and Suzuki Reactions

Carbon-carbon bond formation reactions such as Heck and Suzuki cross-couplings are very useful for the production of pharmaceuticals, agrochemicals, natural products and new optical and electronic materials.[16,17] The Nobel Prize in Chemistry 2010 honoured Richard F. Heck and Akira Suzuki, as well as Ei-ichi Negishi, for their work on palladium-catalyzed cross-coupling reactions.[18] The Heck (or Mizoroki-Heck) reaction, involves C-C bond formation by coupling of an alkene with an alkyl or aryl halide in the presence of a base (Scheme 4.1.A).[19,20] In the Suzuki (or Suzuki-Miyaura) reaction, a C-C bond is formed through coupling of an arylboronic acid with an aryl halide in the presence of a base (Scheme 4.1.B).[21]

Scheme 4.1. General Scheme for (A) Heck and (B) Suzuki coupling reactions.

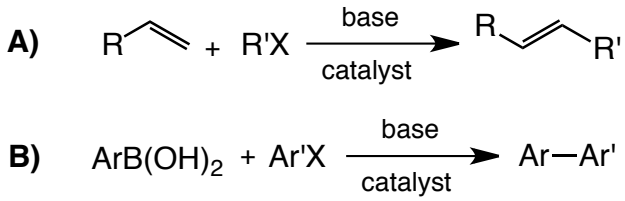

Though Pd is the most commonly used catalytic metal in these processes, other metals, such as Ru and Ni, also show activity towards cross-coupling reactions.[22,23] The proposed mechanisms for homogeneous catalysis of these cross-coupling reactions are closely related (Figure 4.2). Both mechanisms begin with oxidative addition of an aryl halide to the catalytic metal. In a Heck reaction (Figure 4.2.A), the coordinated alkene then undergoes migratory insertion into the M-Ar bond. Finally, the product is released through β-hydride elimination. Regeneration of the catalyst is achieved by neutralization of the coordinated hydrogen halide with an added base. In the case of the Suzuki reaction (Figure 4.2.B), the initial oxidative addition is followed by transmetallation. Reductive elimination then releases the product and regenerates the catalyst.

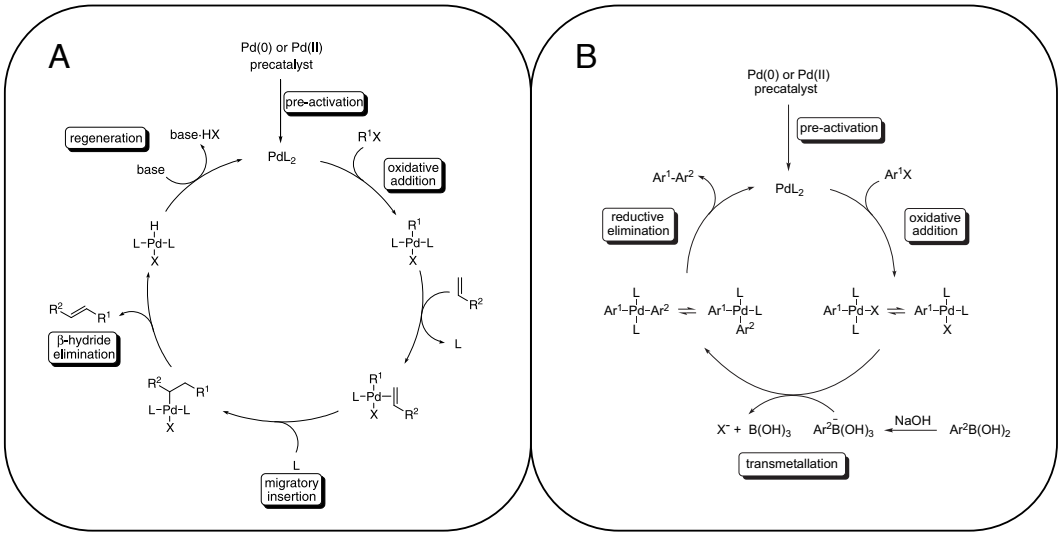

Figure 4.2. Homogeneous catalytic mechanisms for (A) Heck and (B) Suzuki couplings, adapted from refs. 22 and 23.

For heterogeneous catalytic systems, a variety of mechanisms have been proposed. One involves conversion of reactants to products while adsorbed on the solid surface.[5,24] However, catalytic metals in heterogeneous systems often leach into products, a process that explains the observed reactivity and is referred to as quasi-homogeneous catalysis.[12,24] This product contamination must be minimized to ensure product purity but also reusability of the catalyst.[25] In experiments using membrane-isolated chambers, both catalytic metal atoms and ions have been observed to leach from the support.[24] The leaching of Pd(II) is understood to occur through oxidative addition of the aryl halide.[12] However, if the catalytic reaction proceeds to completion, it is believed metal is redeposited onto the support.[26,27] This deposition reduces product contamination but can lead to coarsening of the catalytic metal particles, deactivating the catalyst. In summary, the "ideal" catalyst will be facile and cost-effective to synthesize, easily recovered, resistant to deactivation with low metal leaching, and exhibit excellent catalytic activity with a broad scope of substrates, characterized by both high turnover number (TON) and frequency (TOF). TON and TOF, generally not reported in nanoparticle catalysis, are key characteristic measures of catalytic efficiency that facilitate comparison of different catalytic systems. These values quantify the number of reactions catalyzed per unit time, as well as the total number of reactions catalyzed before deactivation.

4.1.3. Iron/Iron Oxide Core-Shell Nanoparticles

The support materials investigated in this chapter are iron/iron oxide core-shell NPs, also known as nano-scale zero-valent iron (nZVI or $Fe@Fe_xO_y$). nZVI have been of substantial research interest for environmental remediation purposes since the early 1990s.[28] Pseudospherical, size polydisperse $Fe@Fe_xO_y$ may be synthesized by sodium borohydride reduction of iron (III) salts (equation 4.1).[29,30] Oxidation under ambient conditions then leads to the formation of an oxide surface.

$$4\ Fe^{3+} + 3\ BH_4^- + 9\ H_2O \rightarrow 4\ Fe^0 + 3\ H_2BO_3^- + 12\ H^+ + 6\ H_2 \qquad (4.1)$$

The structure of $Fe@Fe_xO_y$ has been spectroscopically identified as a zero-valent (metallic) iron core protected by a mixed-valent iron (II, III) oxide shell (Fe_xO_y) that forms an iron oxyhydroxide (FeOOH) surface in aqueous solution.[28,31] The combined properties of this core-shell structure impart the ability to adsorb ions and molecules on the hydroxylated surface, and use the electron-donating ability of the zerovalent core to reduce chemical species of appropriate electrochemical potential ($E°(Fe/Fe^{2+}) = -0.447$ V).[32] This ability of sorption and reduction has lead to the application of $Fe@Fe_xO_y$ in environmental remediation of halogenated organic compounds and heavy metals, for example (Figure 4.3).[28,33,34]

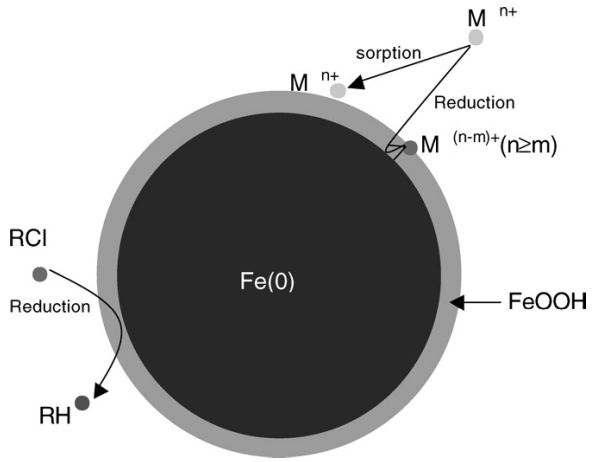

Figure 4.3. Remediation capacity of nZVI imparted by the complex formation capacity of the hydroxylated oxide surface and the reductive capacity of the zerovalent iron core, adapted from ref. 28.

Our group has previously investigated the use of $Fe@Fe_xO_y$ to remove metal ions from organic solution and coordinating environments, establishing it as a useful tool to remove catalytic metals from reaction mixtures.[30,35] Since the remediation process generates metal-decorated $Fe@Fe_xO_y$ ($Fe@Fe_xO_y$/M), and such materials have demonstrated improved catalysis of reductive dechlorination, among others, we were interested in exploring the catalytic activity of $Fe@Fe_xO_y$/M in common catalytic processes such as C-C bond formation by Heck and Suzuki couplings.[33,36] Iron and iron oxide NPs have been investigated in catalysis both as active sites and as magnetic supports. Fe NPs show good activity in hydrogenation of alkenes and alkynes, as well as dehydrogenation of ammonia borane, and C-C bond formation between alkyl halides and aryl Grignard reagents.[37-40] As catalyst supports, magnetic iron oxides have been used with or without protective coatings such as silica or polymer shells to support both

homogeneous catalysts and metal NPs.[3,7] Pd NPs supported on dopamine-stabilized $NiFe_2O_4$ or Fe_3O_4 NPs showed 100% conversion in hydrogenation of nitro and azide compounds to amines, and alkenes and alkynes to alkanes, at a catalyst loading of 1.2 mol% Pd.[41] Similarly, Pd NPs reduced onto silica-coated Fe_2O_3 are useful catalysts in nitrobenzene hydrogenation.[42] Asymmetric catalysis has also been achieved using an iron oxide-tethered catalyst. The Ru(II) complex [Ru(BINAP-PO_3)(DPEN)Cl_2] (BINAP-PO_3H_2: (R)-2,2′-bis(diphenylphosphino)-1,1′-binaphthyl-4-phosphonic acid, DPEN: (R,R)-1,2-diphenylethylenediamine) was attached to the surface of Fe_3O_4 through the phosphonate group, and yielded up to 98% enantiomeric excess in asymmetric hydrogenation of aromatic ketones. It was also shown to have a negligible loss of activity over 14 cycles.[43] Numerous studies have shown the application of iron oxide-supported Pd to C-C bond forming reactions such as the Heck, Suzuki, and Sonogashira couplings. Homogeneous complexes of Pd have been tethered to γ-Fe_2O_3 with N-heterocyclic carbenes attached to the surface through a siloxane group or a crosslinked polymer shell. At 7.3 mol% Pd loading, yields in the range of 70% to 93% were obtained in Suzuki, Heck and Sonogashira couplings of bromo- and iodobenzene with differently substituted alkenes. Only a slight reduction in catalytic activity was observed over the course of five reactions.[44,45] Pd NPs supported on Fe_3O_4 have also been shown to catalyze Heck reactions, however the yield decreased from 81% to 53% over the course of five reactions.[10] When tethered to $NiFe_2O_4$ through dopamine, yields in the range of 76% to 98% were observed with aryl halides (X = Cl, Br, I) for Heck and Suzuki reactions at high

temperatures. The system displayed good reusability after 3 runs.[9] Pd NPs on Fe_3O_4 were also shown to produce yields of up to 98% in Sonogashira reactions, where the catalyst could be reused without significant loss of activity in seven consecutive reactions.[8]

In this chapter, the synthesis and characterization of $Fe@Fe_xO_y/M$ (M = Pd, Ru, Au) and their application as catalysts in Heck and Suzuki couplings is described. We also present the dependence of M oxidation state on $Fe@Fe_xO_y$:M ratio ("M loading") for the case of Pd.

4.2. Experimental Details

4.2.1. Material Preparation

4.2.1.1. Reagents and Materials

Ferric chloride ($FeCl_3$, 97%), sodium borohydride ($NaBH_4$, 99%), gold chloride ($HAuCl_4 \cdot 3H_2O$, ACS reagent), palladium, 10 wt% on activated carbon (Pd/C), palladium black (Pd), triethylamine ($(C_2H_5)_3N$, ≥99%), styrene (C_8H_8, ≥99%), phenylboronic acid ($C_6H_7BO_2$, 95%) bromobenzene (C_6H_5Br, 99%), chlorobenzene (C_6H_5Cl, 99%), iodobenzene (C_6H_5I, 98%) and $CDCl_3$ were purchased from Sigma-Aldrich. Palladium nitrate ($Pd(NO_3)_2 \cdot xH_2O$, ~40% Pd, 99.9%) was purchased from Strem Chemicals. Ruthenium chloride ($RuCl_3 \cdot xH_2O$, 99.9%) was purchased from Alfa Aesar. Potassium hydroxide (KOH, ACS grade), magnesium sulfate ($MgSO_4$, anhydrous), and N-N-dimethylformamide (DMF, anhydrous, 99.8%) were purchased from Caledon. Potassium carbonate (K_2CO_3, analytical reagent) was purchased from Mallinckrodt. Nitric acid (HNO_3, ACS grade) was purchased from EMD Chemicals. Ethanol was purchased from Commercial Alcohols Inc. All reagents were used as received.

4.2.1.2. Synthesis of iron/iron oxide core-shell nanoparticles (Fe@Fe_xO_y)

Fe@Fe_xO_y were prepared using a modified literature procedure.[29,30] Ferric chloride (3.24 g, 20 mmol) was dissolved in 400 mL distilled water in a 2 L three-necked round-bottom flask with a large stirbar. The orange solution was stirred vigorously while 3 equiv. sodium borohydride (2.50 g, 66 mmol) in 30 mL

distilled water were added dropwise from an addition funnel. A black precipitate formed. The solution was left to stir until hydrogen evolution subsided (*ca.* 30 min). After allowing the precipitate to settle, most of the solution was decanted. The particles were filtered through a 7 cm diameter Büchner funnel with Whatman #2 filter paper, and washed with 500 mL distilled water followed by 100 mL 100% ethanol. WARNING: dry Fe NPs are pyrophoric upon reaction with oxygen, do not filter to dryness. The precipitate was reduced to a black paste by filtration and transferred with a spatula to a 50 mL round-bottom flask. The particles were dried *in vacuo* for two days, shaking up large aggregates after the first day, and ground into a fine powder in a glovebox (H_2O, O_2 < 2 ppm) using a ceramic mortar and pestle. Yield: 1.11 g.

4.2.1.3. Metal deposition on Fe@Fe_xO_y

For metal deposition, 25 mg Fe@Fe_xO_y were removed from the glovebox in a test tube with a septum and connected to an argon-charged Schlenk line via needle. The metal salt was dissolved in pH 10.5 KOH and added to the dry particles (see Table 4.1 for details). The amount of metal that can be deposited was determined from previous work.[35] After 15 min sonication, the product was centrifuge-washed thrice with 5 mL portions of pure water. A final wash was done with the solvent used in catalysis (see Tables 4.2 and 4.3 for details).

To investigate the influence of metal loading on metal oxidation states, 20 mg portions of Fe@Fe_xO_y were sonicated for 30 min in 10.0, 6.69 and 3.34 mL pH 10.5 KOH containing 15.7 μM $Pd(NO_3)_2$. The resulting Fe@Fe_xO_y/Pd were centrifuge-washed thrice with pure water, once with ethanol and dried *in vacuo*.

Pd^{2+} remaining in solution was detected by Inductively-Coupled Plasma Mass Spectrometry (ICP-MS), $Fe@Fe_xO_y/Pd$ were characterized by X-Ray Photoelectron Spectroscopy (XPS).

Table 4.1. Metal loading of $Fe@Fe_xO_y$.[**]

Metal	Precursor	Loading capacity [μmol/mg $Fe@Fe_xO_y$]
Pd	$Pd(NO_3)_2 \cdot xH_2O$	7.87
Ru	$RuCl_3 \cdot xH_2O$	5.20
Au	$HAuCl_4 \cdot 3H_2O$	7.75

4.2.1.4. Heck reaction

Styrene (6 mmol) and aryl halide (5 mmol) were mixed with potassium carbonate (6 mmol) in a three-necked round-bottom flask under an argon atmosphere. The catalyst was added in solvent, and the reaction was carried out for 20 h. Detailed reaction conditions are given in Table 4.2. After reaction, particles were removed by filtration and washed with diethyl ether. The remaining organic solution was washed with three 15 mL portions of distilled water followed by brine to remove DMF. The organic phase was dried over magnesium sulfate. Diethyl ether was removed using a rotary evaporator. The products were identified by Gas Chromatography coupled with Mass Spectrometry (GC-MS).

[**] personal communication with Janet Macdonald

To study reusability of the catalyst, particles were washed with dichloromethane and DMF after reaction, and redispersed in DMF for a second run.

Table 4.2. Heck reaction conditions.

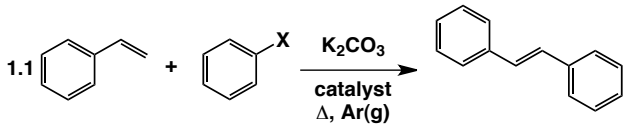

Entry	X	Solvent	T [°C]	Catalyst	mol% M	%yield
1	Br	DMF	65	Fe@Fe_xO_y/Ru	2	0
2	Br	DMF	85	Fe@Fe_xO_y/Au	20	0
3	Br	DMF	85	Fe@Fe_xO_y/Pd	0.2	0
4	Br	DMF	85	Fe@Fe_xO_y/Pd	2	13
5	Br	DMF	85	Fe@Fe_xO_y/Pd	20	8
6	Br	C_2H_5OH	83	Fe@Fe_xO_y/Pd	3	1.4
7	Br	DMF	83	Fe@Fe_xO_y/Pd	3	1.6
8	Cl	DMF	130	Fe@Fe_xO_y/Pd	2	0
9	Br	DMF	130	Fe@Fe_xO_y/Pd	2	6
10	Br	DMF	130	Fe@Fe_xO_y/Pd	2	0.3
11	I	DMF	130	Fe@Fe_xO_y/Pd	2	79
12	I	DMF	130	Fe@Fe_xO_y/Pd	2	72
13	Br	DMF	85	Fe@Fe_xO_y	0	0
14	Br	DMF	95	Pd/C	2	0.7
15	Br	DMF	95	Pd black	2	1.0

4.2.1.5. Suzuki reaction

A modified literature procedure was employed for entries 16-19.[46] Briefly, phenylboronic acid (6 mmol) and potassium carbonate (10 mmol) were mixed in a

three-necked round-bottom flask. The different catalysts (see Table 4.3, 5 mol% Pd) were dispersed in 15 mL DMF by sonication and added to the flask. Bromobenzene (5 mmol) was finally added, and the flask evacuated and refilled thrice with argon. The reaction mixture was stirred at 80 °C for 20 h. After reaction, particles were removed by gravity filtration (Whatman #2 filter paper) and washed with diethyl ether. The remaining organic solution was washed with three 30 mL portions of distilled water followed by brine to remove DMF. The organic phase was dried over magnesium sulfate. Diethyl ether was removed on a rotary evaporator, and the products were analyzed by GC-MS.

For entries 20-29, bromobenzene (2.0 mmol) and phenylboronic acid (2.4 mmol) were dissolved in 5 mL ethanol in a three-necked round-bottom flask. Potassium carbonate (5 mmol) in 2 mL distilled water and catalyst, sonicated in 3 mL distilled water, were added to the solution. The reaction mixture was stirred at the indicated temperature in air for the indicated time (see Table 4.3). After reaction, the catalyst was separated by gravity filtration (Whatman #2 filter paper) and the mixture was extracted with diethyl ether (4 × 25 mL). The organic layers were combined, dried with anhydrous $MgSO_4$ and the solvent was removed on a rotary evaporator to yield the crude product. Products were identified by GC-MS.

While these reactions were performed in air, the catalyst may undergo slow oxidation in solution upon prolonged (*i.e.*, >>48 hours) exposure to air, and should not be exposed to air when dry.

Table 4.3. Suzuki reaction conditions.

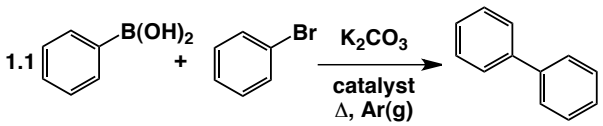

Entry	Solvent	T [°C]	t [h]	Catalyst	mol%	%yield
16	DMF/H_2O[††]	80	20	Fe@Fe_xO_y/Pd	5	96.5[‡‡]
17	DMF/H_2O	80	20	Pd/C	5	100
18	DMF/H_2O	80	20	Pd black	5	100
19	DMF/H_2O	80	20	Fe@Fe_xO_y	N/A	0[§§]
20	H_2O	25	4	Fe@Fe_xO_y/Pd	0.1	0
21	C_2H_5OH	25	4	Fe@Fe_xO_y/Pd	0.1	15
22	H_2O	80	4	Fe@Fe_xO_y/Pd	0.1	81
23	H_2O/C_2H_5OH[***]	25	4	Fe@Fe_xO_y/Pd	0.1	80
24	H_2O/C_2H_5OH	80	4	Fe@Fe_xO_y/Pd	0.1	96
25	H_2O/C_2H_5OH	25	4	Fe@Fe_xO_y/Pd	0.5	97
26	H_2O/C_2H_5OH	80	4	Fe@Fe_xO_y/Pd	0.5	99
27	H_2O/C_2H_5OH	25	4	Fe@Fe_xO_y/Pd	1	83
28	H_2O/C_2H_5OH	25	4	Fe@Fe_xO_y/Pd	2	36
29	H_2O/C_2H_5OH	25	4	Pd/C	0.5	90

[††] 30 mL DMF, 1.5 mL H_2O
[‡‡] and 2.7% triphenylboroxin
[§§] and 15.8% triphenylboroxin
[***] 1:1 ratio

4.2.2. Material Characterization

4.2.2.1. Transmission Electron Microscopy (TEM)

TEM was performed using a JEOL 2010 Transmission Electron Microscope with a LaB_6 thermionic emission filament operated at an accelerating voltage of 200 kV. The instrument was fitted with an Energy Dispersive X-Ray (EDX) detector for elemental analysis. TEM samples were prepared by drop-coating ethanolic powder suspensions onto carbon-coated, 200-mesh Cu grids (SPI Supplies).

4.2.2.2. X-Ray Photoelectron Spectroscopy (XPS)

XPS was performed on an AXIS-165 XPS spectrometer from Kratos Analytical. The base pressure and operating pressure in the chamber were maintained at $\leq 10^{-7}$ Pa. A monochromatic Al K_α X-ray ($\lambda = 8.34$Å) was used to irradiate the samples, and the spectra were obtained with an electron take-off angle of 90°. Samples were pressed into carbon tape. To control sample charging, the charge neutralizer filament was used during the experiment. The pass energy for the survey and the high-resolution spectra were 160 and 20 eV, respectively. Spectra were calibrated to the C 1s emission at 284.8 eV attributed to adventitious carbon using CasaXPS (VAMAS) software. Following calibration, the background of each spectrum was subtracted using a Shirley-type background to remove most of the extrinsic loss structure. Fitting was carried out using 70% Lorentzian/30% Gaussian line shapes for metal zero-oxidation states, and Gaussian line shapes for higher oxidation states. Binding Energy values and

orbital splitting were consistent with literature values obtained from the NIST database.[47]

4.2.2.3. Inductively coupled plasma mass spectrometry (ICP-MS)

ICP-MS was performed on a Perkin Elmer Elan 6000 ICP-MS. Sample solvents were evaporated and the organic components were removed by heating at 625 °C for several hours. The residues were dissolved in concentrated nitric acid and analyzed by ICP-MS. The flow rate on the instrument was 1 mL/min and dual detector mode was employed. A blank was subtracted after internal standard correction and the values reported are an average of three readings (35 sweeps per reading).

4.2.2.4. Gas chromatography-mass spectrometry (GC-MS)

Gas chromatography-mass spectrometry (GC-MS) was performed on a HP 5890 with a 5970 MSD using electron ionization. 1 μL of an acetone solution of the product was injected into a DB-5MS column with a 0.25 μm film. The carrier gas was helium at 1 mL/min. The injection port was at 280 °C and a linear temperature profile (50 °C – 280 °C at 10 °C /minute) was employed. For quantitative analysis, standards of 5 mg/mL biphenyl or *trans*-stilbene, were analyzed under identical conditions.

4.3. Results and Discussion

Metal-decorated iron/iron-oxide core-shell nanoparticles ($Fe@Fe_xO_y/M$) are easily synthesized by spontaneous electroless deposition of metal ions on $Fe@Fe_xO_y$ (*vide supra*). In previous work by our group, $Fe@Fe_xO_y$ was shown to remove catalytic metal impurities from organic mixtures by this mechanism.[30,35] Since nanomaterials are of interest as catalysts due to their high surface area-to-volume ratio, we have in turn investigated the use of the heterogeneous product $Fe@Fe_xO_y/M$ in catalytic applications. [6,48]

$Fe@Fe_xO_y/M$ was synthesized by electroless deposition of metal ions in solution on $Fe@Fe_xO_y$ prepared by borohydride reduction of iron (III) chloride. To improve coordination of metal ions to the $Fe@Fe_xO_y$ surface, deposition was carried out in basic solution. Under these conditions, deprotonated surface hydroxyl groups readily coordinate metal ions.[29] The presence and oxidation states of various metals in $Fe@Fe_xO_y/M$ samples was confirmed by X-ray photoelectron spectroscopy (XPS). Figure 4.4 confirms the presence of palladium in the zero oxidation state (Pd $3d_{5/2}$: 335 eV, Pd $3d_{3/2}$: 341 eV)[47], but notably higher oxidation states are also present. This observation prompted us to investigate the influence of metal loading on metal oxidation states, a study which is discussed later in this Chapter. Sample morphologies were analyzed using bright-field transmission electron microscopy (TEM). In Figure 4.5, representative TEM images of $Fe@Fe_xO_y$ as well as $Fe@Fe_xO_y/Pd$ before and after catalysis are presented. $Fe@Fe_xO_y$ assemble into larger aggregates presumably due to the magnetic attractions between individual NPs (Figure

4.5.A). Metal deposition alters interparticle interactions, possibly due to charging or changes in magnetic properties, and individual NPs are more readily discerned (Figure 4.5.B-C). Due to the difficulty of differentiating phase and mass contrast in TEM images, we cannot definitively identify areas of Pd and Fe "richness". We propose the mechanism of Pd reduction likely leads to atomic clusters or islands of Pd forming on the Fe@Fe_xO_y surface, which are microscopically challenging to detect.

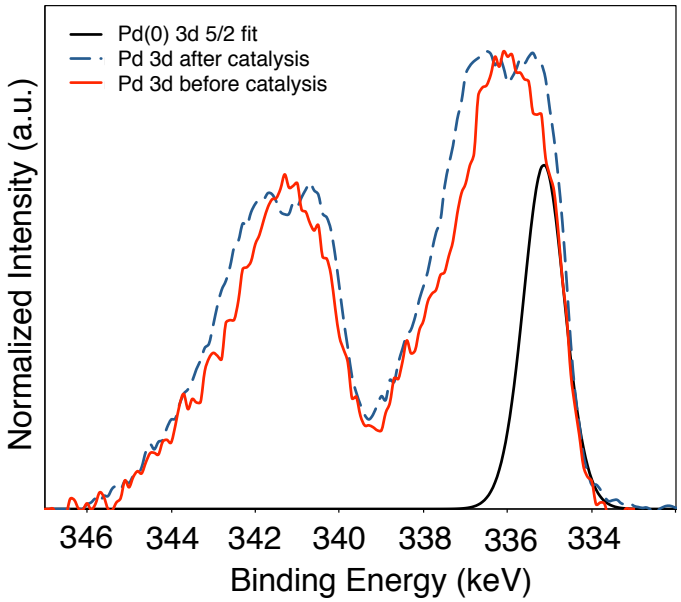

Figure 4.4. X-ray photoelectron (XP) spectrum of the Pd 3d region for Fe@Fe_xO_y/Pd before (red/solid trace) and after catalysis (blue/dashed trace). The location of the zero-oxidation state fit for the Pd $3d_{5/2}$ signal is shown to illustrate the presence of multiple metal oxidation states.

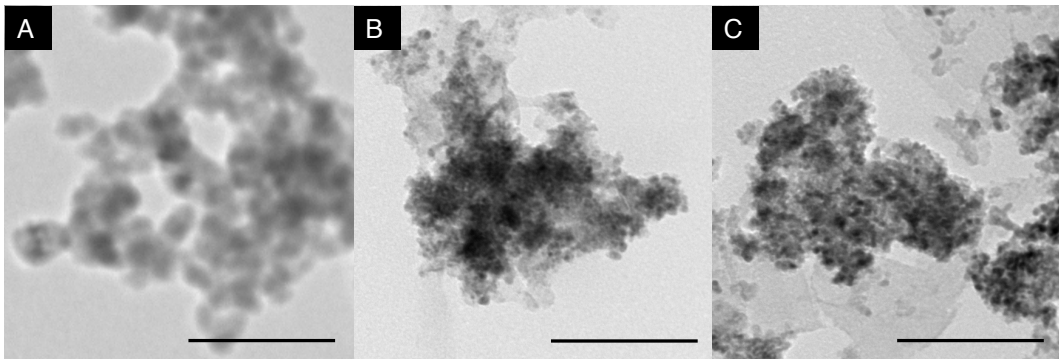

Figure 4.5. Transmission electron microscopy (TEM) images of (A) Fe@Fe_xO_y, (B) Fe@Fe_xO_y/Pd, and (C) Fe@Fe_xO_y/Pd after catalysis. The scale bars are 100 nm.

The catalytic activity of Fe@Fe_xO_y/M was investigated in cross-coupling reactions. Heck and Suzuki couplings, involving the reaction of aryl halides with alkenes or boronic acids (see Scheme 4.2), are important carbon-carbon bond forming reactions that would benefit from identification of a cost-effective, easily recoverable catalyst system. The expected benefit of magnetic recoverability was not confirmed in our studies, owing to changes in magnetic properties upon reduction of a different metal onto the surface. Qualitatively, Fe@Fe_xO_y were strongly magnetic, whereas the as-prepared catalyst Fe@Fe_xO_y/M was less attracted to a magnet placed on the side of the reaction flask. Thus, filtration was used as a means of removing and recovering the catalyst. It is unclear at this point what the origin of the change in magnetic properties is. Reduced magnetization has been attributed to surface oxidation, which is present in Fe@Fe_xO_y, as well as metal coatings and interaction of organic molecules with the particle surface.[49] Generally, any material that interacts strongly with the surface may influence magnetic properties. One way this is reasoned is by limited ability of spin

reorientation upon directional bonding of the surface atoms, leading to an overall reduction in magnetic moment. However, real systems of metal-coated iron-iron oxide nanoparticles are not yet sufficiently well described to truly account for observed changes in magnetic properties.[49]

Scheme 4.2. (a) Heck and (b) Suzuki coupling reactions investigated here.

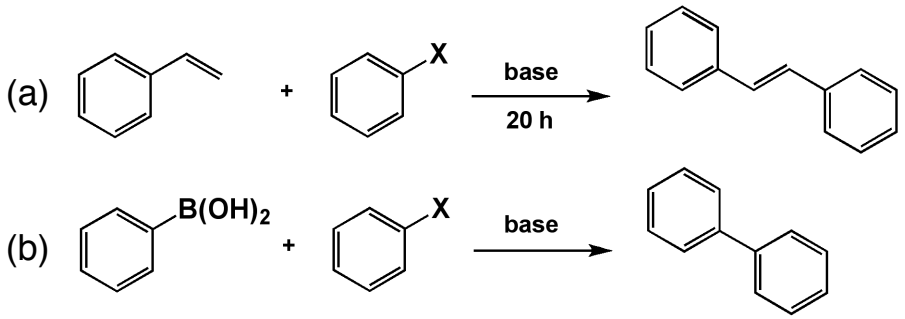

$Fe@Fe_xO_y/M$ (M = Au, Pd, Ru) was tested under a variety of conditions in Heck couplings of phenyl halides and styrene to yield biphenyl, and was generally found to have poor yields or even show no reactivity as determined by gas chromatography coupled with mass spectrometry (GC-MS). The results are summarized in Table 4.2. An investigation into different metals (M = Au, Pd, Ru) confirmed $Fe@Fe_xO_y/Pd$ as the catalyst system of choice (Table 4.2, entries 1 and 4, 2 and 5). The Pd loading was optimized at 2 mol% (Table 4.2, entries 3-5). A change of solvent from dimethylformamide (DMF) to ethanol showed only marginal changes in reactivity (Table 4.2, entries 6, 7). Upon varying the aryl halide from chloro- to bromo- to iodobenzene, we observed the expected trend:

For R = Cl, no coupling was observed (Table 4.2, entry 8), R = Br gave low yields (Table 4.2, entry 9) and R = I showed the most product formation (Table 4.2, entry 11). A second run, in which the catalyst was reused after washing, gave reduced yields, suggesting deactivation of the catalyst (Table 4.2, entries 10 and 12). In the absence of Pd, $Fe@Fe_xO_y$ does not catalyze Heck coupling reactions (Table 4.2, entry 13). Though yields obtained with $Fe@Fe_xO_y$/Pd under the investigated conditions are low, comparison with traditional heterogeneous catalysts such as Pd/C and Pd black suggest that our $Fe@Fe_xO_y$/Pd catalyst is superior under the employed conditions (Table 4.2, entries 4, 14, 15). A possible explanation for this may lie in the reducing power of the $Fe@Fe_xO_y$ support. Given the capacity has not been depleted by Pd^{2+} reduction onto the support, its electron donating ability may facilitate oxidative addition of the aryl halide, thereby improving the catalytic activity of $Fe@Fe_xO_y$/Pd.

In summary, though the catalytic activity of $Fe@Fe_xO_y$/Pd is not comparable to homogeneous catalysts, it appears there may be potential for this system in heterogeneous catalysis. This is further confirmed by results obtained from Suzuki cross-coupling studies.

In Suzuki cross-coupling reactions, an aryl halide (bromobenzene) is coupled with a boronic acid (phenylboronic acid) to yield a C-C bond. In a 20:1 mixture of DMF/H_2O, $Fe@Fe_xO_y$/Pd gave inferior yields compared to Pd/C and Pd black (Table 4.3, entries 16-18). Also, the $Fe@Fe_xO_y$ support was found to catalyze the formation of triphenylboroxin ring structures (Scheme 4.3), an unwanted byproduct (Table 4.3, entries 16, 19). A strong dependence of reactivity

on solvent became apparent upon investigating water and ethanol. At room temperature, no reaction was observed in water, while ethanolic solutions yielded 15% biphenyl (Table 4.3, entries 20, 21). At 80 °C and otherwise identical conditions, the reaction proceeded in water to give 81% yield (Table 4.3, entry 22). Employing a 1:1 mixture of water/ethanol resulted in 80% yield even at room temperature (Table 4.3, entry 23), which upon heating to 80 °C increased to 96% (Table 4.3, entry 24). When the Pd loading was increased from 0.1 mol% to 0.5 mol%, the yield further increased to 97% at room temperature and 99% at 80 °C (Table 4.3, entries 25, 26). Further increasing the Pd loading, however, resulted in decreased yields (Table 4.3, entries 27, 28). Comparing the activity of our catalyst system to Pd/C, we noted that Fe@Fe_xO_y/Pd is again slightly more active under these reaction conditions.

Scheme 4.3. Trimerization of phenylboronic acid to triphenylboroxin.

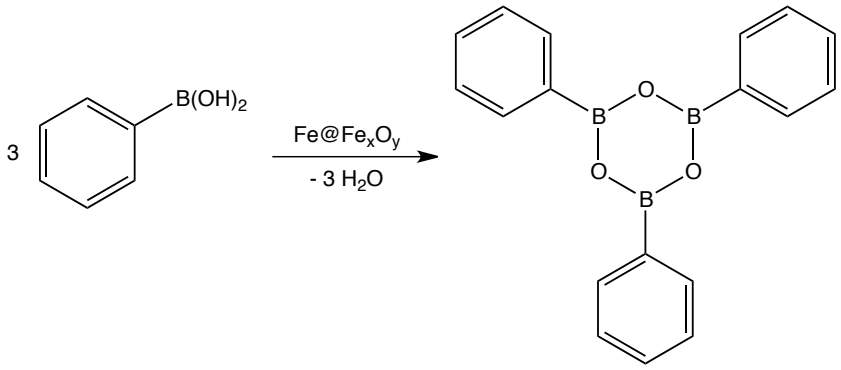

Catalyst leaching was investigated by inductively coupled plasma mass spectrometry (ICP-MS). Our expectation was that the capacity of $Fe@Fe_xO_y$ to reduce metal ions from solutions should lead to relatively low amounts of metal leaching into the final product, which was confirmed. In Suzuki coupling of bromobenzene and phenylboronic acid, the filtrate after one hour of reaction contained 1.87 ppm Pd, while the final product only contained 0.54 ppm. Both values are well below the 5 ppm limit mandated by the European Agency for the Evaluation of Medicinal Products.[50] Since only 0.15 ppm Pd were detected after one hour in a blank solution without bromobenzene and phenylboronic acid present, our hypothesis is that oxidative addition of bromobenzene facilitates dissolution/leaching of Pd, and some of the leached Pd is redeposited on the $Fe@Fe_xO_y$ support after reaction. Thus, it appears that $Fe@Fe_xO_y$/Pd acts as "source" and "sink" for the active catalyst in this reaction.

A further concern was the nature of the Pd surface species. In catalyst synthesis we noted the supernatant turned orange during washing steps at maximum loadings, suggesting dissolution of Pd ions from the $Fe@Fe_xO_y$ support. Since the surface $-O^-$ groups have the ability to coordinate Pd^{2+}, we propose any Pd^{2+} exceeding the reduction capacity of $Fe@Fe_xO_y$ remains coordinated to the catalyst support surface. Li and coworkers reported the reduction of adsorbed metal ions depends on the difference in reduction potentials.[34] Since the effective reduction potential of Fe will change due to oxidation as metal ions are reduced at the $Fe@Fe_xO_y$ surface, we propose the existence of a maximum reduction capacity, after which ions remain simply

adsorbed to the surface and no longer undergo reduction. To investigate this in more detail, we carried out an XPS study of Pd oxidation states as a function of $Fe@Fe_xO_y$/Pd loading amounts (Figure 4.6). We compared values for maximum, 2/3 and 1/3 loading and evaluated the corresponding Pd oxidation states. The XPS data supports our hypothesis of incomplete reduction at maximum loading. The black trace shows an intense signal for $3d_{5/2}$ and $3d_{3/2}$ at higher binding energies, associated with higher oxidation states of Pd. This signal decreases substantially with reduced Pd loading. At 1/3 loading capacity, the XPS signal is mostly due to elemental Pd, indicating that almost all adsorbed Pd ions are reduced by the support under these conditions. Though we have not investigated this experimentally, we hypothesize that the presence of different Pd species on the $Fe@Fe_xO_y$ surface will have profound influences on catalytic activity of these materials.

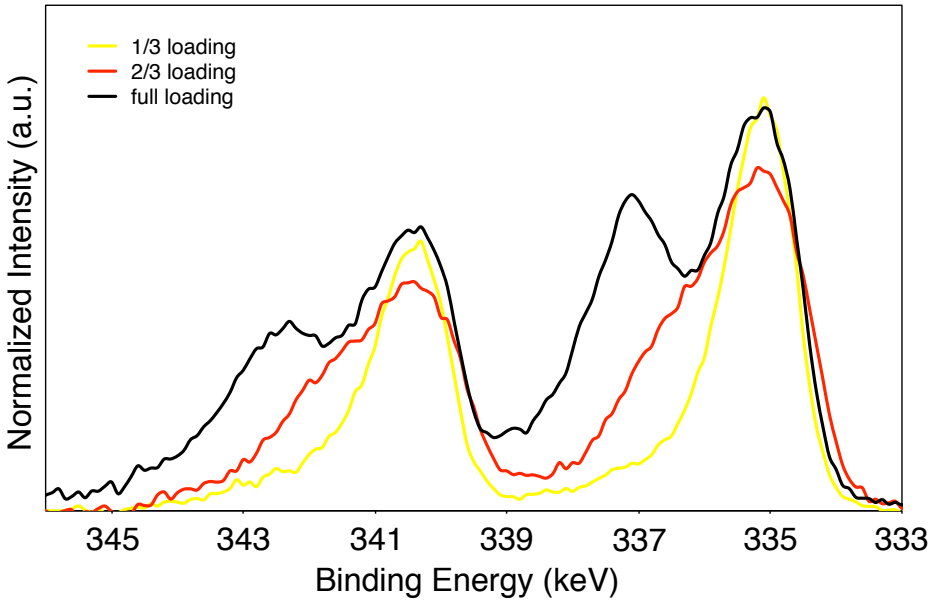

Figure 4.6. X-ray photoelectron (XP) spectrum of the Pd 3d region for Fe@Fe_xO_y/Pd prepared with the maximum (black trace), 2/3 of the maximum (red trace) and 1/3 of the maximum Pd loading (yellow trace).

4.4. Conclusions and Future Work

In the present study, Fe@Fe_xO_y/Pd was found to be a promising heterogeneous catalyst for C-C bond forming Heck and Suzuki reactions. Under the tested conditions, other metals (Au, Ru) did not yield comparable results, and common heterogeneous catalysts such as Pd black and Pd/C also gave lower yields. Though the magnetic recoverability, which the Fe@Fe_xO_y support was hoped to impart, was not reliably obtained, the heterogeneous system showed low metal leaching in products recovered by filtration. Thus, catalyst removal and recovery are relatively facile and the catalyst system could possibly be used in batch or flow-through industrial processes.

The leaching study appears to support homogeneous Pd as the active species in Suzuki coupling reactions. Here, higher Pd leaching was measured during the reaction than in the final product. We propose this is due to the ability of the $Fe@Fe_xO_y$ support to redeposit Pd ions from solution after catalysis is complete.

The reductive properties of the $Fe@Fe_xO_y$ support can be carefully tailored *via* the amount of deposited metal during catalyst synthesis. An XPS study into the influence of metal loading on metal oxidation state showed incomplete reduction of the catalytic metal at maximum loading capacity. Likely, it would be ideal to deposit lower amounts of metal in order to preserve the reductive capacity of $Fe@Fe_xO_y$ and avoid the presence of coordinated, unreduced metal ions on the support surface.

4.5. References

(1) Cong, H.; Porco, J. A., Jr. *ACS Catal.* **2012**, *2*, 65–70.
(2) Cuenya, B. R. *Thin Solid Films* **2010**, *518*, 3127–3150.
(3) Schätz, A.; Reiser, O.; Stark, W. J. *Chem. Eur. J.* **2010**, *16*, 8950–8967.
(4) Wagner, M.; Köhler, K.; Djakovitch, L.; Weinkauf, S.; Hagen, V.; Muhler, M. *Top. Catal.* **2000**, *13*, 319–326.
(5) Köhler, K.; Wagner, M.; Djakovitch, L. *Catal. Today* **2001**, *66*, 105–114.
(6) Astruc, D.; Aranzaes, J. R.; Lu, F. *Angew. Chem. Int. Ed.* **2005**, *44*, 7852–7872.
(7) Zhu, Y.; Stubbs, P.; Ho, F.; Liu, R.; Ship, P. *Chem. Cat. Chem.* **2010**, *2*, 365–374.
(8) Liu, J.; Peng, X.; Sun, W.; Zhao, Y.; Xia, C. *Org. Lett.* **2008**, *10*, 3933–3936.
(9) Baruwati, B.; Guin, D.; Manorama, S. V. *Org. Lett.* **2007**, *9*, 5377–5380.
(10) Wang, Z.; Shen, B.; Aihua, Z.; He, N. *Chem. Eng. J.* **2005**, *113*, 27–34.
(11) Roucoux, A.; Schulz, J.; Patin, H. *Chem. Rev.* **2002**, *102*, 3757–3778.
(12) Durand, J.; Teuma, E.; Gomez, M. *Eur. J. Inorg. Chem.* **2008**, *2008*, 3577–3586.
(13) Ferrando, R.; Jellinek, J.; Johnston, R. L. *Chem. Rev.* **2008**, *108*, 845–910.
(14) Lee, J.-K.; Kung, M. C.; Kung, H. H. *Top. Catal.* **2008**, *49*, 136–144.
(15) Narayanan, R. *Molecules* **2010**, *15*, 2124–2138.
(16) Rouhi, A. M. *Chem. Eng. News* **2004**, *82*, 49–58.
(17) de Vries, J. G. *Can. J. Chem.* **2001**, *79*, 1086–1092.
(18) *http://www.nobelprize.org/nobel_prizes/chemistry/laureates/2010/.*
(19) Mizoroki, T.; Mori, K.; Ozaki, A. *Bull. Chem. Soc. Jpn.* **1971**, *44*, 581.
(20) Heck, R. F.; Nolley, J. P. *J. Org. Chem.* **1972**, *37*, 2320–2322.
(21) Miyaura, N.; Suzuki, A. *Chem. Rev.* **1995**, *95*, 2457–2483.
(22) Alonso, F.; Beletskaya, I. P.; Yus, M. *Tetrahedron* **2005**, *61*, 11771–11835.
(23) Alonso, F.; Beletskaya, I. P.; Yus, M. *Tetrahedron* **2008**, *64*, 3047–3101.
(24) Gaikwad, A. V.; Holuigue, A.; Thathagar, M. B.; ten Elshof, J. E.; Rothenberg, G. *Chem. Eur. J.* **2007**, *13*, 6908–6913.
(25) Glasnov, T. N.; Findenig, S.; Kappe, C. O. *Chem. Eur. J.* **2009**, *15*, 1001–1010.
(26) Duran Pachon, L.; Rothenberg, G. *Appl. Organometal. Chem.* **2008**, *22*, 288–299.
(27) Crudden, C. M.; McEleney, K.; MacQuarrie, S. L.; Blanc, A.; Sateesh, M.; Webb, J. D. *Pure Appl. Chem.* **2007**, *79*, 247–260.
(28) Li, X.-Q.; Elliott, D.; Zhang, W.-X. *Crit. Rev. Solid State Mater. Sci.* **2006**, *31*, 111–122.
(29) Li, X.-Q.; Zhang, W.-X. *Langmuir* **2006**, *22*, 4638–4642.
(30) Macdonald, J. E.; Kelly, J. A.; Veinot, J. G. C. *Langmuir* **2007**, *23*, 9543–9545.

(31) Sun, Y.-P.; Li, X.-Q.; Cao, J.; Zhang, W.-X.; Wang, H. P. *Adv. Colloid Interface Sci.* **2006**, *120*, 47–56.
(32) *CRC Handbook of Chemistry and Physics*; Weast, R. C.; Lide, D. R.; Astle, M. J.; Beyer, W. H., Eds. CRC Press, Inc.: Boca Raton, FA; pp. D–152.
(33) Lien, H.-L.; Zhang, W.-X. *Appl. Catal., B* **2007**, *77*, 110–116.
(34) Li, X.-Q.; Zhang, W.-X. *J. Phys. Chem. C* **2007**, 6939–6946.
(35) Macdonald, J. E.; Veinot, J. G. C. *Langmuir* **2008**, *24*, 7169–7177.
(36) Shih, Y.-H.; Chen, Y.-C.; Chen, M.-Y.; Tai, Y.-T.; Tso, C.-P. *Colloids Surf., A* **2009**, *332*, 84–89.
(37) Bedford, R. B.; Betham, M.; Bruce, D. W.; Davis, S. A.; Frost, R. M.; Hird, M. *Chem. Commun.* **2006**, 1398–1400.
(38) Yan, J.-M.; Zhang, X.-B.; Han, S.; Shioyama, H.; Xu, Q. *Angew. Chem. Int. Ed.* **2008**, *47*, 2287–2289.
(39) Rangheard, C.; de Julián Fernández, C.; Phua, P.-H.; Hoorn, J.; Lefort, L.; de Vries, J. G. *Dalton Trans.* **2010**, *39*, 8464–8471.
(40) Phua, P.-H.; Lefort, L.; Boogers, J. A. F.; Tristany, M.; de Vries, J. G. *Chem. Commun.* **2009**, 3747–3749.
(41) Guin, D.; Baruwati, B.; Manorama, S. V. *Org. Lett.* **2007**, *9*, 1419–1421.
(42) Yi, D. K.; Lee, S. S.; Ying, J. Y. *Chem. Mater.* **2006**, *18*, 2459–2461.
(43) Hu, A.; Yee, G. T.; Lin, W. *J. Am. Chem. Soc.* **2005**, *127*, 12486–12487.
(44) Stevens, P. D.; Li, G.; Fan, J.; Yen, M.; Gao, Y. *Chem. Commun.* **2005**, 4435–4437.
(45) Stevens, P. D.; Fan, J.; Gardimalla, H. M. R.; Yen, M.; Gao, Y. *Org. Lett.* **2005**, *7*, 2085–2088.
(46) LeBlond, C. R.; Andrews, A. T.; Sun, Y.; Sowa, J. R. *Org. Lett.* **2001**, *3*, 1555–1557.
(47) *http://srdata.nist.gov/xps*.
(48) Zhou, S.; Johnson, M.; Veinot, J. G. C. *Chem. Commun.* **2010**, *46*, 2411–2413.
(49) Huber, D. L. *Small* **2005**, *1*, 482–501.
(50) Note for Guidance on Specification Limits for Residues of Metal Catalysts - http://www.emea.europa.eu/ema/pdfs/human/swp/444600en.pdf (accessed Jul. 2012).

Chapter 5:

Conclusions

and

Future Work

5.1. Germanium Nanoparticle Synthesis

Germanium nanomaterials are attractive for a variety of applications ranging from medicine (fluorescent labels, photothermal therapy) to (opto)electronics including photodetectors and memory devices.[1-7] Ge-NCs may exhibit photoluminescence, which arises from quantum confinement or defect states.[8,9] In the case of quantum confinement, the larger Bohr exciton radius than Si promises size-controlled properties at larger (and easier to synthesize) crystal sizes.[1,10,11] A common defect that can determine luminescence properties is caused by oxidation. The formation and stability of GeO_2 is a complicating factor in Ge due to the unstable nature of the oxide at atmospheric conditions. With its size-tunable electronic properties, high refractive index and low toxicity, Ge is also of interest in a variety of other electronic and optical applications.[12-14] For example, oxide-embedded Ge-NCs are being investigated as a replacement of polycrystalline Si floating gates in memory devices.[4,7]

The aim of this work has been to investigate factors underlying the synthesis of Ge-NPs. Straightforward, cost-effective synthesis that yields reliable, well-defined materials is still not generally achieved, driving us to better understand how the organic substituents influence Ge-NP formation in the solid state and in solution.

5.1.1. Solid-State Synthesis from $RGeO_{1.5}$

In Chapter Two, we presented an investigation of the influence of organic substituents on oxide-embedded Ge-NC formation from $RGeO_{1.5}$ sol-gel materials.[15] The study showed substituents with more favourable elimination characteristics (*i.e.*, presence of β-hydrides on substituent, formation of stable radicals) will eliminate at lower temperatures. The lowest temperatures achieved were 400 °C for powders and 300 °C in molten films (in contrast to 525 °C in the original synthesis).[16] The elimination of R-groups at lower temperatures enables the Ge-NC-forming disproportionation reaction (equation 6.1) to proceed at lower temperatures. Beyond a lowering of the processing temperature requirements, our approach also limits Ge(0) production to a single process. At the previously required higher temperature, both reduction and disproportionation were active contributors to Ge-NC formation.[17] Limiting the formation of elemental Ge to one source is expected to yield better-defined products with lower size polydispersity, though this still needs to be supported by experimental evidence.

$$4\ GeO_{1.5} \rightarrow Ge + 3\ GeO_2 \qquad (5.1)$$

One issue that remains to be addressed is the incorporation of carbonaceous residue into the oxide composite. Currently, exact location and chemical nature of this impurity is unknown, but its presence has hampered liberation of freestanding Ge-NCs (FS-Ge-NCs). The formation of germanium

oxycarbides and carbides, though thermodynamically unfavourable,[18] cannot fully be ruled out and may in itself impart useful properties to the material.

5.1.2. Future Work

The presented method, at least at the current stage, is not well suited for the production of FS-Ge-NCs. If FS-Ge-NCs are the material of interest, efforts may be better placed into developing sol-gel reactions of germanium precursors such as tetraethoxygermane (TEOG) with other oxide precursors of similar reactivity, to obtain near-homogeneous mixtures of the two. Thermal processing in a reducing atmosphere can then produce Ge-NCs embedded in the oxide of the second material. For this route to be useful, the embedding oxide must be stable against hydrogen reduction up to 500 °C, electrochemically stable against reduction by the forming elemental Ge, and removable by a method leaving Ge-NCs unaffected. This approach has been demonstrated with a SiO_2 matrix, however, the different reaction rates between TEOG and tetraethoxysilane (TEOS) give a poor distribution of Ge within the matrix.[19] This leads to extremely low yields of Ge-NCs after removal of bulk surface Ge and SiO_2 matrix by peroxide and hydrofluoric acid etching.[19] Related to this approach of localizing GeO_2 within an oxide matrix to produce Ge-NCs, future efforts could be directed at the synthesis and hydrogen reduction of freestanding GeO_2 nanostructures as a route to a variety of Ge nanomaterials. Here, shape and size of the nanomaterial may be tailored through different geometries of the GeO_2 precursors.[20,21]

Ideally, the presented method of Ge-NC synthesis by thermal disproportionation would be improved by the use of $HGeO_{1.5}$, which would cleanly decompose to yield Ge-NCs in a germanium oxide matrix. However, methods to counteract the disproportionation of $HGeCl_3$ and the hydrolysis of the H-Ge bond during sol-gel synthesis need to be found to make this approach viable. Considering synthetic methods not based on sol-gel chemistry, currently the possibly best way to achieve well-defined Ge-NCs is by plasma-synthesis from $GeCl_4$.[3] This method minimizes the presence of contaminants in comparison to solution-based synthesis. Disadvantages include the more expensive and specialized instrumentation and the inability to carry out *in-situ* surface functionalization. Also, the presence of halide may eventually be found to be detrimental to optical properties (as found in a recent study of Si PL in our group).

Future research on the presented thermal decomposition of organogermane polymers may mitigate the challenges associated with removal of oxide matrix and carbon impurities, and functionalization of oxide-free Ge-NCs, which are not straightforward to obtain from these materials.

Complete liberation of the organic substituent would simplify the etching process, and may be achieved by processing the sol-gel precursor at lower temperatures first to remove the organic substituent before increasing the temperature to grow Ge-NCs. This method may reduce or completely remove the carbonization deduced from C/H ratios in elemental analysis of our composites. Further, the synthesis of an impurity-free composite of Ge-NCs embedded in an oxide-matrix may in itself be of interest for device applications. Here, the sol-gel

reaction would need to be modified to produce thin layers of sol-gel material on a substrate. Since the processing conditions now allow temperatures as low as 400 °C for powder composites (R = ethyl, allyl), they can be incorporated into electronic devices that use CMOS technology, which generally are only stable up to 400 °C.[22]

Alternatively, a better understanding of the nature of the carbon impurities is required. This knowledge could lead either to pathways for Ge-NC liberation, or to applications of the oxycarbide or carbide material itself.

Etching with hydrofluoric acid, hydrogen peroxide and nitric acid have thus far not been successful routes to FS-Ge-NCs, since these methods were found to remove both GeO_2 and Ge preferentially. These approaches may be more useful if isolation of Ge-NCs from the etching suspension containing carbonaceous residue can be achieved. An in-situ functionalization strategy that permanently renders the NCs hydrophobic may aid this process by facilitating Ge-NC extraction. For example, etching may be carried out in hydrofluoric acid solution in the presence of an alkene, which under UV irradiation has been shown to add to the Ge-NC surface through light-induced hydrogermylation.[23]

If the carbon impurities are found to positively impact the properties of the oxide-embedded Ge-NCs, for example by introducing a further way of tuning the electronic properties next to NC size, these materials can be explored for application in devices. Thin films of the oxide-embedded Ge-NCs (or (oxy)carbides) would be of interest for applications such as non-volatile memory or photovoltaics.[4,7,24,25]

Of interest to the same types of applications are the *n*-butyl- and benzyl-substituted precursors, in which the variation in organic substituents led to melting at low temperatures (~300 °C). Under the presented conditions, films of oxide-embedded Ge-NCs were rough, and also contained unidentified carbonaceous residue. For thin film applications in optical and electronic devices,[25-27] it may be of interest to investigate the melting behaviour in detail and determine ways to obtain smooth, continuous films with potentially interesting optical and electronic properties. Ways this may be achieved include processing at lower temperatures to remove the substituents and avoid further gas formation before melting the films, or processing the melt for extended times to allow smoothening of the film surface after gas formation ceases.

The patterning of freestanding Ge nanostructures using block-copolymer self-assembly is explored in Appendix B of this thesis. A functional block copolymer is used to localize and catalyze sol-gel reaction of tetraethoxygermane to yield patterns of GeO_2. These are converted to patterns of elemental Ge *via* thermal hydrogen reduction. The method demonstrates that block copolymers can be exploited not only to direct the assembly of adsorbed particles, molecules or ions, but also to participate in their chemical transformation. Oxide and semiconductor patterns are of interest to applications such as solar cells, and, in the case of Ge, can be further used to produce semiconductor/metal heterostructures or metallic patterns by electroless deposition of more noble metals.[28-31]

5.1.3. Solution Synthesis by Hot Injection of $n\text{Bu}_x\text{GeH}_{4-x}$

In the solid-state study discussed in Chapter Two, the *n*-butyl substituted germanium-rich oxide yielded Ge-NCs at the lowest processing temperature (300 °C). This prompted the study detailed in Chapter Three, in which the investigation of substituent effects was continued with solution-synthesis of Ge-NPs from molecular *n*-butylgermanes. The presence of increasing numbers of hydride substituents in $n\text{Bu}_x\text{GeH}_{4-x}$ (x = 1-4) was found to lower the decomposition temperature of the molecular precursors in hot injection reactions from 390 °C in $n\text{Bu}_4\text{Ge}$ to ~285 °C in $n\text{BuGeH}_3$. In line with the argument made in Chapter Two regarding the effect of different elimination pathways on Ge-C bond-breaking temperature, a possible reason for this observation may be facile reductive elimination of hydrogen with the butyl-group or a second hydrogen atom.[32]

Since no coordinating surface ligand was added in initial reactions, the products obtained by hot injection of $n\text{Bu}_x\text{GeH}_{4-x}$ (x = 1-4) were amorphous, polydisperse, aggregated Ge-NPs. At constant temperature (400 °C and 325 °C), differing nucleation and growth processes may explain differences in observed sizes and shapes. For $n\text{Bu}_4\text{Ge}$, the decomposition temperature is very close to the reaction temperature of 400 °C, likely leading to slower decomposition, which provides a continuous supply of monomer "Ge" and is expected to prolong the nucleation phase, yielding size-polydisperse material. As the decomposition temperature is lowered with decreasing x, we are more likely to obtain burst nucleation, in which the initial monomer concentration is high but rapidly

decreases upon nucleation, transitioning into a growth phase and yielding less polydisperse products.[33] Since we used a relatively long reaction time for a hot injection method, this is the likely origin of the wide size distribution observed for *n*$BuGeH_3$ and *n*Bu_2GeH_2. Thus, this precursor can be expected to undergo the fastest decomposition, giving it the longest growth period, in which Ostwald ripening will lead to a broadening of the size distribution.[34] Hot injection was also carried out in a weakly coordinating solvent, trioctylamine, at 325 °C. Products obtained displayed improved dispersibility, and, in the case of *n*$BuGeH_3$, smaller NPs that were well dispersed, not aggregated, in TEM. However, oxidative stability and crystallinity were not achieved, characteristics that will be targeted in future experiments.

5.1.4. Future Work in *n*Bu_xGeH_{4-x}-based Synthesis

Ge-NCs have previously been synthesized by hot injection methods. Both injection of a mixture of $Ge[N(SiMe_3)_2]_2$ and oleylamine into octadecene at 300 °C, and injection of tetrabutyl-, tetraethyl- or trichlorogermane (in squalene) into trioctylamine, squalene or octacosane at temperatures around 400 °C were able to produce Ge-NCs.[35,36] Thus, a point of interest is the lack of crystallinity observed in our materials at this point. Different solvents, peak reaction temperatures, and growth times are factors that should be investigated in the quest to obtain Ge-NCs.[37] Attention should also be paid to the possibility that crystallinity is lost upon oxidation of the poorly surface-protected Ge-NPs. Other studies demonstrate crystallinity at low temperatures, but samples have experienced minimal exposure

to air before analysis.[35] Laser annealing has also been used in the past to crystallize Ge-NPs.[38] Microwave synthesis may be another interesting route to consider, since the ability to operate at elevated pressures may aid crystallization, and Ge NPs may experience localized heating as they are formed in solution.

To improve surface stability against oxidation and aggregation, appropriate surfactants or coordinating solvents such as phosphines or amines, or other surface-capping agents such as terminal alkenes, may be added into the reaction mixture. The interaction of these groups with the surface of Ge-NCs will interrupt growth and may lead to well-dispersed, oxidatively stable products with narrower size distributions. Tertiary amines have already been ruled out as appropriate surface capping agents in reactions with trioctylamine. They may be unsuitable due to the weak coordination between the lone pair on nitrogen and the Ge surface, as well as packing issues with neighbouring molecules on the surface. Here, the investigation of primary amines may be more beneficial.[39] Other factors influencing particle size and size distribution are reaction temperature and time, which need to be optimized for each precursor in order to identify the 'optimal' reagent for Ge-NC synthesis in the $n\text{Bu}_x\text{GeH}_{4-x}$ (x = 1-4) series. A time of 30 min was picked at the beginning of the study since Zaitseva *et al.* observed an induction time of 30 min in decomposition of tetrabutylgermane. Preliminary results with $n\text{Bu}_x\text{GeH}_{4-x}$ (x = 1-3) indicate this is not the case here, leading us to investigate shorter reaction times in the future.

The effect of different solvents on NP properties is also of interest. Related work from our group regarding the surface termination of Si-NCs suggests

heteroatoms play an important role in their luminescence properties. This effect would be interesting to study once crystallization has been achieved.

The decomposition of *n*-butylgermanes to give elemental Ge can also be applied to the synthesis of other nanostructures, possibly including nanowires (NWs) and heterostructures. Ge-NWs are often grown by a vapour-liquid-solid mechanism, using metal nanoparticles as seeds.[40] However, Zaitseva *et al.* observed the formation of Ge-NWs in the absence of a seed NP, and proposed the condensation of solvent droplets in reactions run at reflux leads to Ge-NW formation.[36,41] We may be able to exploit this by carrying out the reaction in a solvent that boils close to the decomposition temperatures of $n\mathrm{Bu}_x\mathrm{GeH}_{4-x}$ (x = 1-3), for example octadecene (315 °C) for x = 2, 3 or hexadecane (287°C) for x = 1. Further, heterostructures could be produced by seeded growth, where the core material is supplied in suspension, and *n*-butylgermanes decompose to grow on these seeds. For example, it may be interesting to grow Si/Ge core-shell structures to investigate their optical and electronic properties.[42]

5.2. Metal-Decorated Iron/Iron Oxide Nanoparticles in Catalysis

Nanoparticle catalysis aims to combine high activity and selectivity arising from high surface area, curvature and faceting with good recoverability, in iron oxides primarily based on magnetic properties.[43-45] Iron/iron-oxide based catalysts are already used in dehalogenation of organic compounds.[46] They are easily synthesized by room-temperature reduction of iron (III) chloride followed by electroless deposition of the catalytic metal.[47] The latter process is spontaneous for most metals due to the low electrochemical potential of iron ($E°(Fe/Fe^{2+})$ = -0.447 V).[48] The catalysis of C-C bond formation by M/Fe@Fe_xO_y was the subject of investigation in Chapter Four.

5.2.1. Conclusions

C-C bond formation by Heck and Suzuki cross-coupling reactions is most commonly catalyzed by Pd.[49-52] Under the presented conditions, Pd/Fe@Fe_xO_y showed promising catalytic activity in comparison to other heterogeneous catalysts such as Pd/C. Two other metals that are active towards Heck coupling are Ru and Au.[53-55] However, Ru/Fe@Fe_xO_y and Au/Fe@Fe_xO_y were not of comparable activity to Pd/Fe@Fe_xO_y in Heck couplings under the presented conditions. For these catalysts, there may be a need for stabilizing agents or variation of other conditions to achieve high activity.[54,55] Also, the Ru oxidation states after complexation by the Fe@Fe_xO_y support are not straightforward to deduce.[56] The absence of zerovalent metal may explain the reduced activity

observed in the presented study.[54] Magnetic recovery of the catalysts was not achieved, likely due to changes in magnetic properties upon metal deposition. Surface coatings have been shown to influence magnetic properties of nanoparticles, in some cases leading to a reduction of the net magnetization.[57-59]

Upon removing the catalyst by filtration, only low metal leaching was observed in the final product. In contrast, we detected higher Pd levels in solution during the reaction. This suggests a quasi-homogeneous mechanism, in which solvated Pd (ions) are the active species, accounting for the observed catalytic activity from Pd/Fe@Fe_xO_y. When the reaction is complete, the solvated Pd is deposited back onto Fe@Fe_xO_y by virtue of the support's reductive capacity.[60]

The metal oxidation states that are present on the surface of Fe@Fe_xO_y will be one of the factors determining catalytic activity. An XPS study of metal oxidation states as a function of metal loading shows incomplete reduction of Pd at maximum loading capacity, and almost complete reduction upon decreasing to 1/3 of the loading capacity. The presence of adsorbed Pd ions may change the catalytic mechanism, or, since Pd(0) is the active species in the suggested homogeneous mechanism, may reduce the activity by "wasting" Pd in non-active forms. This phenomenon requires further investigation.

5.2.2. Future Work

Future work in this area should concentrate on two aspects: better understanding the material properties and tailorability of the heterogeneous catalyst (*i.e.,* morphology and oxidation state of active metal, solution stability of

M/Fe@Fe_xO_y) to tailor catalytic performance, and increasing the breadth of catalyzed reactions.

In the majority of iron nanoparticle literature, it has been overlooked (at least in the writing of manuscripts, but likely beyond) that borohydride reduction of metal salts can lead to the formation of borides. In particular, Fe borides have been synthesized from $FeSO_4$ in aqueous solution.[61,62] However, in a different study, borides were shown to form preferentially in organic solvents, not in aqueous solution.[63] Since these findings are in conflict with one another, and a third study actually induces ~2 wt% boride incorporation by exposing hematite (α-Fe_2O_3) nanoparticles to sodium borohydride,[64] this should be investigated in more detail for our materials. X-ray photoelectron survey spectra of Fe@Fe_xO_y currently do not suggest the presence of B in any oxidation state, though high-resolution spectra should be obtained to verify this.

Working towards the goal of obtaining a truly well defined, tailorable catalyst, it may be desirable to move to a better-defined support material. The Fe@Fe_xO_y support has a very broad size distribution (~20-80 nm). If this size distribution is variable between different batches, the surface area per mass of catalyst support will be different, influencing the amount of deposited metal and complicating standardization of the method. Also, the different sizes will have iron cores of varying sizes, since there is a limited thickness of ~3 nm to the surface oxide shell.[65] The differences in core size may also influence the reductive capacity, and thus the surface reactivity and metal deposition, on these supports. Instead, iron nanoparticles could be synthesized by established techniques to

generate particles of narrow size distribution, such as high-temperature decomposition of $Fe(CO)_5$ and related compounds.[66]

High-resolution transmission electron microscopy (HRTEM) imaging of M/Fe@Fe_xO_y would be beneficial to elucidate the actual morphology and distribution of metal deposits on Fe@Fe_xO_y. Hindering factors here may be the tendency of agglomeration in Fe@Fe_xO_y, and the large particle size in contrast to the assumed size of metal deposits (as deduced from lack of observation in low-resolution TEM). Techniques that may be able to overcome these challenges include high-angle annular dark field imaging, which gives excellent Z contrast, as well as elemental mapping techniques such as EELS or EDS mapping.[67-70]

The catalyst system will likely show a dependence of catalytic activity on initial loading of the catalytic metal.[46] As shown in Chapter Four, the initial loading is one factor influencing the oxidation states of the metal supported on Fe@Fe_xO_y. Thus, catalytic activity should be investigated with regards to not only the amount of catalytic metal and its ratio to the support, but also the oxidation states that are present. The metal oxidation state may be tailored to achieve complete reduction (low loading) or a mixture of oxidation states on the support surface (higher loading). By reducing the amount of metal deposited, more reductive capacity remains with the Fe@Fe_xO_y support, changing the ways it can interact with the catalytically active metal and substrates.

In future leaching studies, which are key to the applicability of catalyst systems, attention should be paid not only to the amount of metal released into solution, but also the amount remaining on the Fe@Fe_xO_y support. Since our

preliminary data suggests the dissolution and redeposition of catalytic metal during reaction, a potential pitfall next to issues such as catalyst coarsening due to redeposition is the loss of catalytic metal through deposition onto reactor walls and components, rather than the support itself. This may be a contributing factor in the reduced reactivity observed after reuse of the Pd/Fe@Fe_xO_y catalyst. Thorough material characterization, including HRTEM, is needed to understand the deactivation process and provide the necessary information to reduce its effects.

In an effort to reduce aggregation, improve homogenization, and increase reusability of M/Fe@Fe_xO_y catalysts, the use of stabilizing agents should be considered. In our work, we chose not to employ surface ligands to reduce additional need for purification and avoid extra impurities. Also, zero-valent iron in environmental remediation is used without further protection of the surface, unless mobility of the material in the environment is desired.[60,71] However, the high reactivity of nanoscale surfaces likely causes aggregation of the system, amplifying any coarsening that may occur during redeposition of the catalytic metal. Potential ligands for Fe@Fe_xO_y include organic acids (*e.g.*, oleic acid) or polymers (*e.g.*, polystyrene).[60,72] It may also be of interest to investigate ligands that will interact with the catalytic metal surface, though this kind of stabilization could also be expected to lower catalytic activity, since it both inhibits dissolution of the metal and access of substrate to the surface, depending on the mechanism that underlies catalytic activity of M/Fe@Fe_xO_y. Suitable ligands used to stabilize

Pd colloids in catalysis include ammonium salts and polymers such as polyvinylpyridine (PVP).[52]

Further, it would be interesting to thoroughly understand the change in electronic and magnetic properties observed upon metal deposition on $Fe@Fe_xO_y$. For this purpose, it may be of value to measure the magnetic moments of the material as a function of the amount of metal deposited, as well as evaluating surface charge through zeta potential measurements. To the best of our knowledge, there has been no detailed investigation into the distribution of charge after reduction of metal ions onto $Fe@Fe_xO_y$.

In terms of investigating a wider breadth of catalytic reactions, other industrially relevant processes should be considered. We have carried out some initial work on hydrogenation reactions, which could be expanded further. Interestingly, the $Fe@Fe_xO_y$ support displays catalytic activity in hydrogenation reactions,[73] offering the possibility of combining the support reactivity with that of the deposited metal. If appropriate catalytic activity is observed, it will be of interest to carry out catalyst poisoning studies. Here, $Fe@Fe_xO_y$ may protect the catalytically active metal from poisoning, *i.e.*, deactivation of the catalyst. The iron oxide may have the ability to protect the catalytically active metal from poisoning by compounds containing elements such as sulfur, present for example in oil sands crude. Hydrogenation of these mixtures would be improved by the presence of the $Fe@Fe_xO_y$ support, if it sacrificially converts to the sulfide while protecting the more noble catalytic metal.[74,75]

5.3. References

(1) Prabakar, S.; Shiohara, A.; Hanada, S.; Fujioka, K.; Yamamoto, K.; Tilley, R. D. *Chem. Mater.* **2010**, *22*, 482–486.

(2) Lambert, T. N.; Andrews, N. L.; Gerung, H.; Boyle, T. J.; Oliver, J. M.; Wilson, B. S.; Han, S. M. *Small* **2007**, *3*, 691–699.

(3) Holman, Z. C.; Kortshagen, U. R. *Langmuir* **2009**, *25*, 11883–11889.

(4) Das, S.; Singha, R. K.; Manna, S.; Gangopadhyay, S.; Dhar, A.; Ray, S. K. *J. Nanopart. Res.* **2011**, *13*, 587–595.

(5) Boyle, T. J.; Tribby, L. J.; Ottley, L. A. M.; Han, S. M. *Eur. J. Inorg. Chem.* **2009**, 5550–5560.

(6) Xue, D.-J.; Wang, J.-J.; Wang, Y.-Q.; Xin, S.; Guo, Y.-G.; Wan, L.-J. *Adv. Mater.* **2011**, *23*, 3704–3707.

(7) Knebel, S.; Kyriakidou, A.; Bracht, H.; Roesner, H.; Wilde, G. *Appl. Phys. A* **2011**, *103*, 149–158.

(8) Stavarache, I.; Lepadatu, A.-M.; Gheorghe, N. G.; Costescu, R. M.; Stan, G. E.; Marcov, D.; Slav, A.; Iordache, G.; Stoica, T. F.; Iancu, V.; Teodorescu, V. S.; Teodorescu, C. M.; Ciurea, M. L. *J. Nanopart. Res.* **2010**, *13*, 221–232.

(9) Ruddy, D. A.; Johnson, J. C.; Smith, E. R. R.; Neale, N. R. *ACS Nano* **2010**, *4*, 7459–7466.

(10) Maeda, Y.; Tsukamoto, N.; Yazawa, Y.; Kanemitsu, Y.; Masumoto, Y. *Appl. Phys. Lett.* **1991**, *59*, 3168–3170.

(11) Lee, D. C.; Pietryga, J. M.; Robel, I.; Werder, D. J.; Schaller, R. D.; Klimov, V. I. *J. Am. Chem. Soc.* **2009**, *131*, 3436–3437.

(12) Das, S.; Manna, S.; Singha, R.; Anopchenko, A.; Daldosso, N.; Pavesi, L.; Dhar, A.; Ray, S. K. *Phys. Status Solidi A* **2011**, *208*, 635–638.

(13) Shih, G. H.; Allen, C. G.; Potter, B. G. *Sol. Energy Mater. Sol. Cells* **2010**, *94*, 797–802.

(14) Fan, J.; Chu, P. K. *Small* **2010**, *6*, 2080–2098.

(15) Hoffman, M.; Veinot, J. G. C. *Chem. Mater.* **2012**, *24*, 1283–1291.

(16) Henderson, E. J.; Hessel, C. M.; Veinot, J. G. C. *J. Am. Chem. Soc.* **2008**, *130*, 3624–3632.

(17) Henderson, E. J.; Hessel, C. M.; Cavell, R. G.; Veinot, J. G. C. *Chem. Mater.* **2010**, *22*, 2653–2661.

(18) Kim, B.-S.; Lee, J.-H.; Son, K.; Hwang, S. W.; Choi, B. L.; Lee, E. K.; Kim, J. M.; Whang, D. *ACS Appl. Mater. Interfaces* **2012**, *4*, 805–810.

(19) Henderson, E. J.; Seino, M.; Puzzo, D. P.; Ozin, G. A. *ACS Nano* **2010**, *4*, 7683–7691.

(20) Wu, J.; Sun, Y.; Zou, R.; Song, G.; Chen, Z.; Wang, C.; Hu, J. *Cryst. Eng. Comm.* **2011**, *13*, 3674–3677.

(21) Wu, H. P.; Liu, J. F.; Ge, M. Y.; Niu, L.; Zeng, Y. W.; Wang, Y. W.; Lv, G. L.; Wang, L. N.; Zhang, G. Q.; Jiang, J. Z. *Chem. Mater.* **2006**, *18*, 1817–1820.

(22) Takeuchi, H.; Wung, A.; Sun, X.; Howe, R. T.; King, T. J. *IEEE Trans. Electron Devices* **2005**, *52*, 2081–2086.

(23) Sato, S.; Ikeda, T.; Hamada, K.; Kimura, K. *Solid State Commun.* **2009**, *149*, 862–865.
(24) Che, X.; Liu, Z.; Li, Y. *Appl. Surf. Sci.* **2012**, *258*, 6212–6216.
(25) Zhang, B.; Shrestha, S.; Huang, S. J.; Aliberti, P.; Green, M. A.; Conibeer, G. *Energy Procedia* **2010**, *2*, 243–250.
(26) Batra, Y.; Kabiraj, D.; Kanjilal, D. *Solid State Commun.* **2007**, *143*, 213–216.
(27) Lee, P. F.; Lu, X. B.; Dai, J. Y.; Chan, H. L. W.; Jelenkovic, E.; Tong, K. Y. *Nanotechnology* **2006**, *17*, 1202–1206.
(28) Hamley, I. W. *Nanotechnology* **2003**, *14*, R39–R54.
(29) Darling, S. B. *Prog. Polym. Sci.* **2007**, *32*, 1152–1204.
(30) Guldin, S.; Docampo, P.; Stefik, M.; Kamita, G.; Wiesner, U.; Snaith, H. J.; Steiner, U. *Small* **2011**, *8*, 432–440.
(31) Zhang, J.; Gao, Y.; Hanrath, T.; Korgel, B. A.; Buriak, J. M. *Chem. Commun.* **2007**, 1438–1440.
(32) Low, J. J.; Goddard, W. A. *Organometallics* **1986**, *5*, 609–622.
(33) Robb, D. T.; Privman, V. *Langmuir* **2008**, *24*, 26–35.
(34) Talapin, D. V.; Rogach, A. L.; Haase, M.; Weller, H. *J. Phys. Chem. B* **2001**, *105*, 12278–12285.
(35) Gerung, H.; Bunge, S. D.; Boyle, T. J.; Brinker, C. J. J.; Han, S. M. *Chem. Commun.* **2005**, 1914–1916.
(36) Zaitseva, N.; Dai, Z. R.; Grant, C. D.; Harper, J.; Saw, C. *Chem. Mater.* **2007**, *19*, 5174–5178.
(37) Vaughn, D. D., II; Bondi, J. F.; Schaak, R. E. *Chem. Mater.* **2010**, *22*, 6103–6108.
(38) Kornowski, A.; Giersig, M.; Vogel, R.; Chemseddine, A.; Weller, H. *Adv. Mater.* **1993**, *5*, 634–636.
(39) Foos, E. E.; Wilkinson, J.; Mäkinen, A. J.; Watkins, N. J.; Kafafi, Z. H.; Long, J. P. *Chem. Mater.* **2006**, *18*, 2886–2894.
(40) Hanrath, T.; Korgel, B. A. *J. Am. Chem. Soc.* **2002**, *124*, 1424–1429.
(41) Zaitseva, N.; Harper, J.; Gerion, D.; Saw, C. *Appl. Phys. Lett.* **2005**, *86*, 053105.
(42) de Oliveira, E. L.; Albuquerque, E. L.; de Sousa, J. S.; Farias, G. A.; Peeters, F. M. *J. Phys. Chem. C* **2012**, *116*, 4399–4407.
(43) Cong, H.; Porco, J. A., Jr. *ACS Catal.* **2012**, *2*, 65–70.
(44) Cuenya, B. R. *Thin Solid Films* **2010**, *518*, 3127–3150.
(45) Polshettiwar, V.; Luque, R.; Fihri, A.; Zhu, H.; Bouhrara, M.; Basset, J.-M. *Chem. Rev.* **2011**, *111*, 3036–3075.
(46) Lien, H.-L.; Zhang, W.-X. *Appl. Catal., B* **2007**, *77*, 110–116.
(47) Zhou, S.; Johnson, M.; Veinot, J. G. C. *Chem. Commun.* **2010**, *46*, 2411–2413.
(48) *CRC Handbook of Chemistry and Physics*; Weast, R. C.; Lide, D. R.; Astle, M. J.; Beyer, W. H., Eds. CRC Press, Inc.: Boca Raton, FA; pp. D–152.
(49) Fihri, A.; Bouhrara, M.; Nekoueishahraki, B.; Basset, J.-M.; Polshettiwar, V. *Chem. Soc. Rev.* **2011**, *40*, 5181–5203.

(50) Narayanan, R. *Molecules* **2010**, *15*, 2124–2138.
(51) Glasnov, T. N.; Findenig, S.; Kappe, C. O. *Chem. Eur. J.* **2009**, *15*, 1001–1010.
(52) Durand, J.; Teuma, E.; Gomez, M. *Eur. J. Inorg. Chem.* **2008**, *2008*, 3577–3586.
(53) Alonso, F.; Beletskaya, I. P.; Yus, M. *Tetrahedron* **2005**, *61*, 11771–11835.
(54) Na, Y.; Park, S.; Han, S. B.; Han, H.; Ko, S.; Chang, S. *J. Am. Chem. Soc.* **2004**, *126*, 250–258.
(55) Tsunoyama, H.; Sakurai, H.; Ichikuni, N.; Negishi, Y.; Tsukuda, T. *Langmuir* **2004**, *20*, 11293–11296.
(56) Macdonald, J. E.; Veinot, J. G. C. *Langmuir* **2008**, *24*, 7169–7177.
(57) Daou, T. J.; Grenèche, J. M.; Pourroy, G.; Buathong, S.; Derory, A.; Ulhaq-Bouillet, C.; Donnio, B.; Guillon, D.; Begin-Colin, S. *Chem. Mater.* **2008**, *20*, 5869–5875.
(58) Hormes, J.; Modrow, H.; Bönnemann, H.; Kumar, C. S. S. R. *J. Appl. Phys.* **2005**, *97*, 10R102.
(59) Paulus, P. M.; Bönnemann, H.; van der Kraan, A. M.; Luis, F.; Sinzig, J.; de Jongh, L. J. *Eur. Phys. J. D* **1999**, *9*, 501–504.
(60) Li, X.-Q.; Elliott, D.; Zhang, W.-X. *Crit. Rev. Solid State Mater. Sci.* **2006**, *31*, 111–122.
(61) Mustapic, M.; Pajic, D.; Novosel, N.; Babic, E.; Zadro, K.; Cindric, M.; Horvat, J.; Skoko, Z.; Bijelic, M.; Shcherbakov, A. *Croat. Chem. Acta* **2010**, *83*, 275–282.
(62) Wells, S.; Charles, S. W.; Mørup, S.; Linderoth, S.; van Wonterghem, J.; Larsen, J.; Madsen, M. *J. Phys.: Condens. Matter* **1989**, *1*, 8199–8208.
(63) Glavee, G. N.; Klabunde, K. J.; Sorensen, C. M.; Hadjipanayis, G. C. *Inorg. Chem.* **1995**, *34*, 28–35.
(64) de Resende, V.; De Grave, E.; da Costa, G.; Janssens, J. *J. Alloys Compd.* **2007**, *440*, 236–247.
(65) Fauth, K.; Goering, E.; Schütz, G.; Kuhn, L. T. *J. Appl. Phys.* **2004**, *96*, 399–403.
(66) Kura, H.; Takahashi, M.; Ogawa, T. *J. Phys. Chem. C* **2010**, *114*, 5835–5838.
(67) Vaneski, A.; Susha, A. S.; Rodriguez-Fernandez, J.; Berr, M.; Jäckel, F.; Feldmann, J.; Rogach, A. L. *Adv. Funct. Mater.* **2011**, *21*, 1547–1556.
(68) Carbone, L.; Cozzoli, P. D. *Nano Today* **2010**, *5*, 449–493.
(69) Franchini, I. R.; Bertoni, G.; Falqui, A.; Giannini, C.; Wang, L. W.; Manna, L. *J. Mater. Chem.* **2010**, *20*, 1357–1366.
(70) Egerton, R. F. *Rep. Prog. Phys.* **2009**, *72*, 016502.
(71) Borda, M. J.; Venkatakrishnan, R.; Gheorghiu, F. In *Environmental Applications of Nanoscale and Microscale Reactive Metal Particles*; American Chemical Society: Washington, DC, 2009; pp. 219–232.
(72) Gupta, A. K.; Gupta, M. *Biomaterials* **2005**, *26*, 3995–4021.
(73) Hudson, R.; Rivière, A.; Cirtiu, C. M.; Luska, K. L.; Moores, A. *Chem. Commun.* **2012**, *48*, 3360–3362.

(74) Ko, T.-H. *Environ. Eng. Sci.* **2008**, *25*, 969–974.
(75) Dunleavy, J. K. *Platinum Met. Rev.* **2006**, *50*, 110–110.

Appendix A:

Supplementary Data for

Chapter 2:

Understanding the formation of elemental germanium by thermolysis of sol-gel derived organogermanium oxide polymers

A version of this appendix has been published as Supporting Information for:

Hoffman, M.; Veinot, J. G. C. Chem. Mater. ***2012****, DOI: 10.1021/cm2035129*

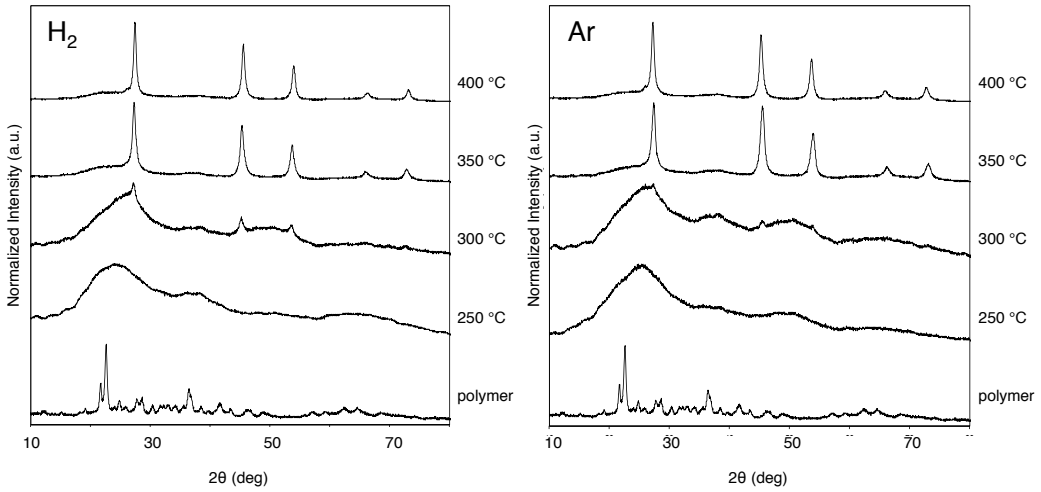

Figure A1. XRD patterns of **2** processed at increasing temperature for one hour in 5% H_2/95% Ar (left) and 100% Ar atmosphere (right).

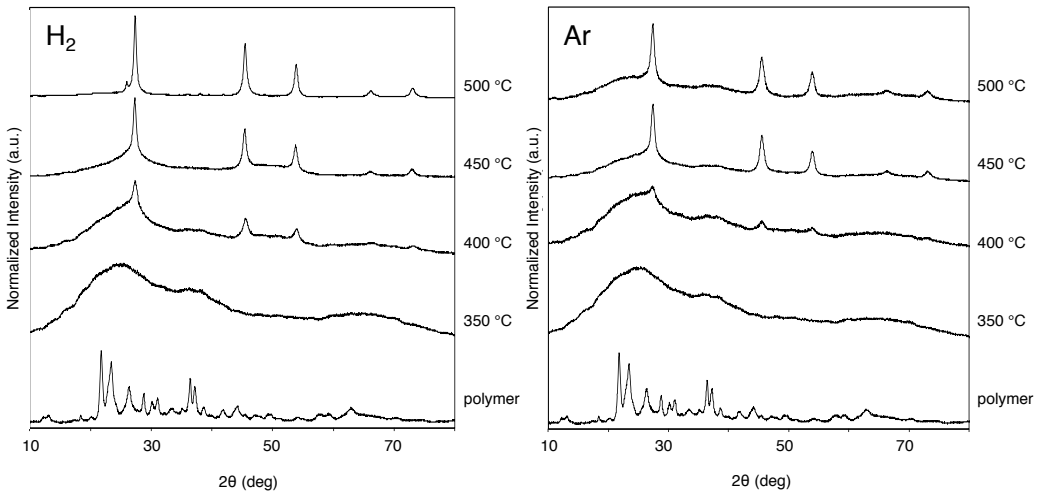

Figure A2. XRD patterns of **3** processed at increasing temperature for one hour in 5% H_2/95% Ar (left) and 100% Ar atmosphere (right).

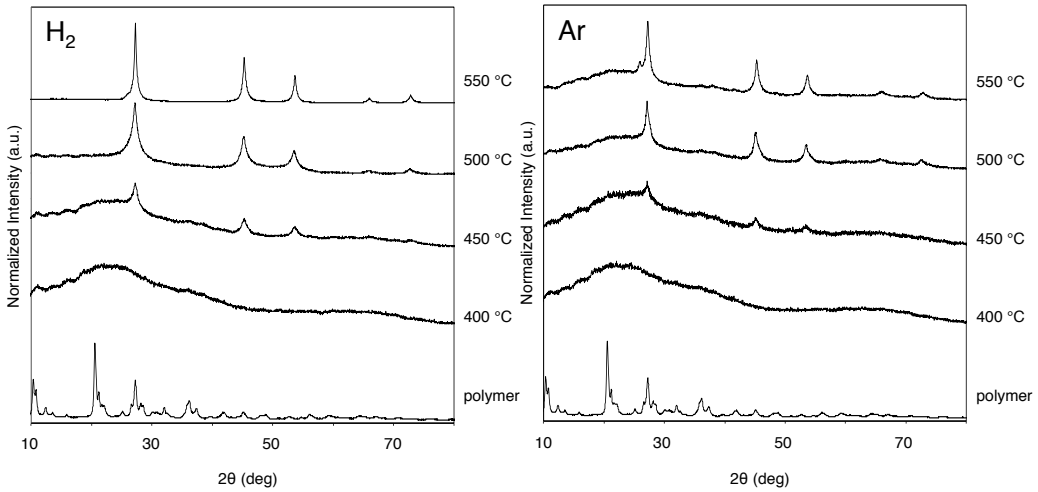

Figure A3. XRD patterns of **4** processed at increasing temperature for one hour in 5% H2/95% Ar (left) and 100% Ar atmosphere (right).

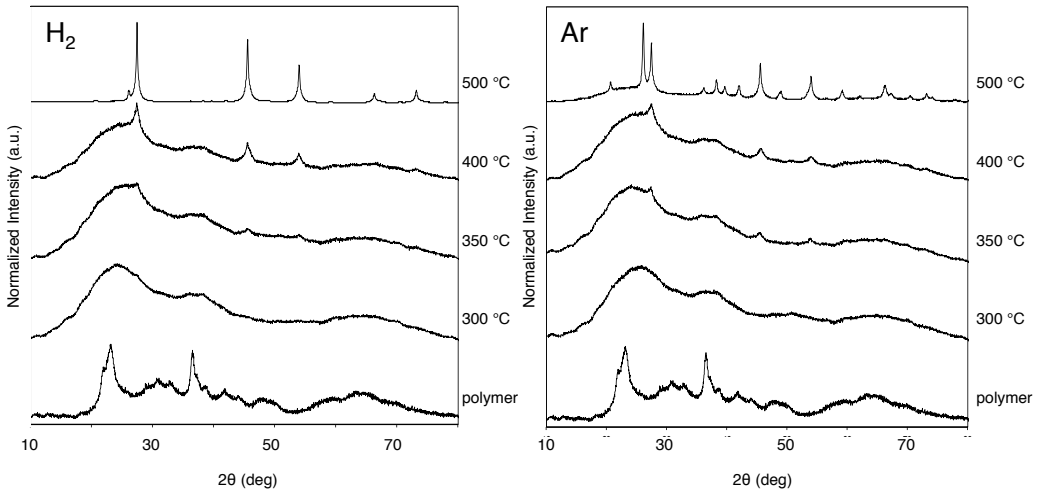

Figure A4. XRD patterns of **5** processed at increasing temperature for one hour in 5% H_2/95% Ar (left) and 100% Ar atmosphere (right).

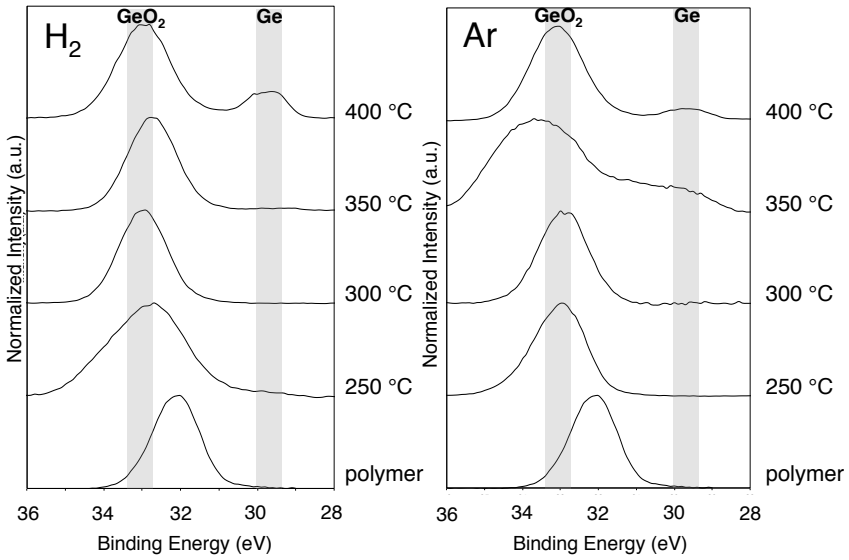

Figure A5. X-Ray Photoelectron (XPS) spectra of the Ge 3d region of **2** processed at indicated peak temperatures for one hour in 5% H_2/95% Ar (left) or 100% Ar atmosphere (right).

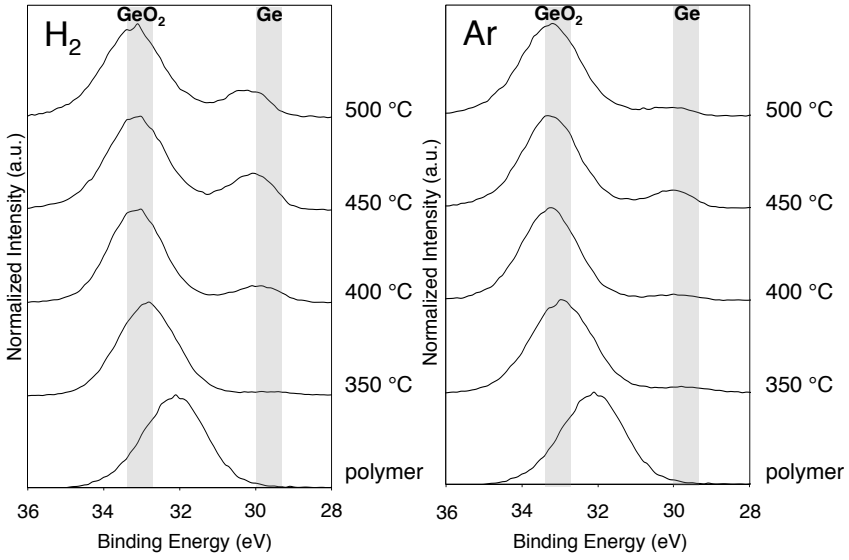

Figure A6. XPS spectra of the Ge 3d region of **3** processed at indicated peak temperatures for one hour in 5% H_2/95% Ar (left) or 100% Ar atmosphere (right).

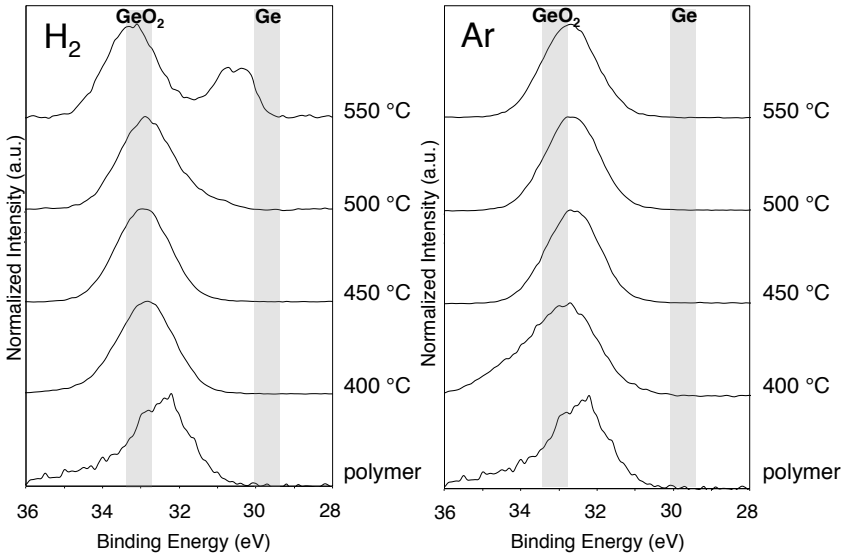

Figure A7. XPS spectra of the Ge 3d region of **4** processed at indicated peak temperatures for one hour in 5% H_2/95% Ar (left) or 100% Ar atmosphere (right).

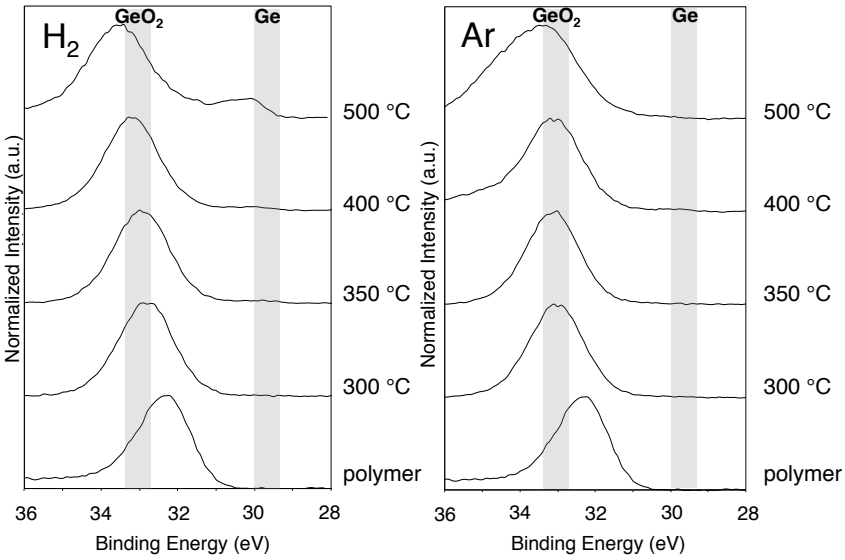

Figure A8. XPS spectra of the Ge 3d region of **5** processed at indicated peak temperatures for one hour in 5% H_2/95% Ar (left) or 100% Ar atmosphere (right).

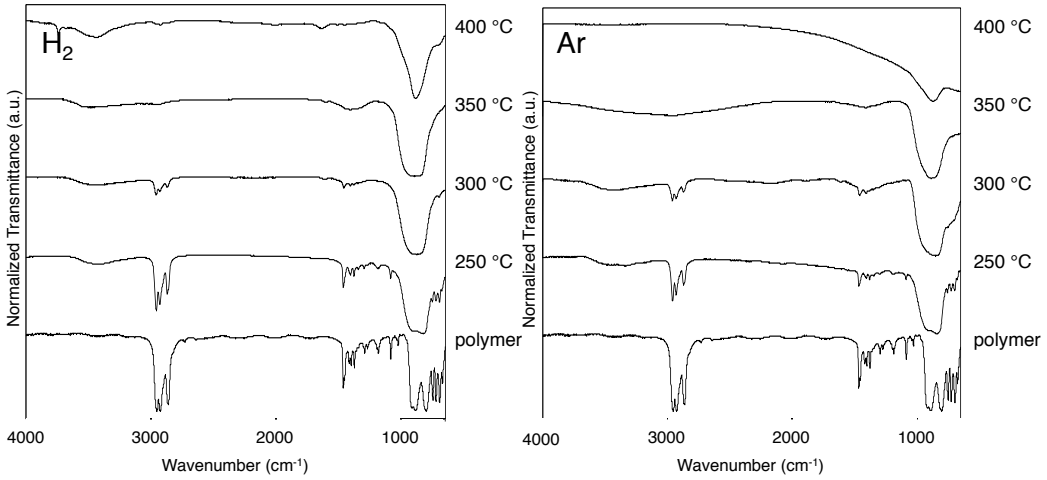

Figure A9. FT-IR spectra of **2** processed at indicated peak temperatures for one hour in 5% H_2/95% Ar (left) or 100% Ar atmosphere (right).

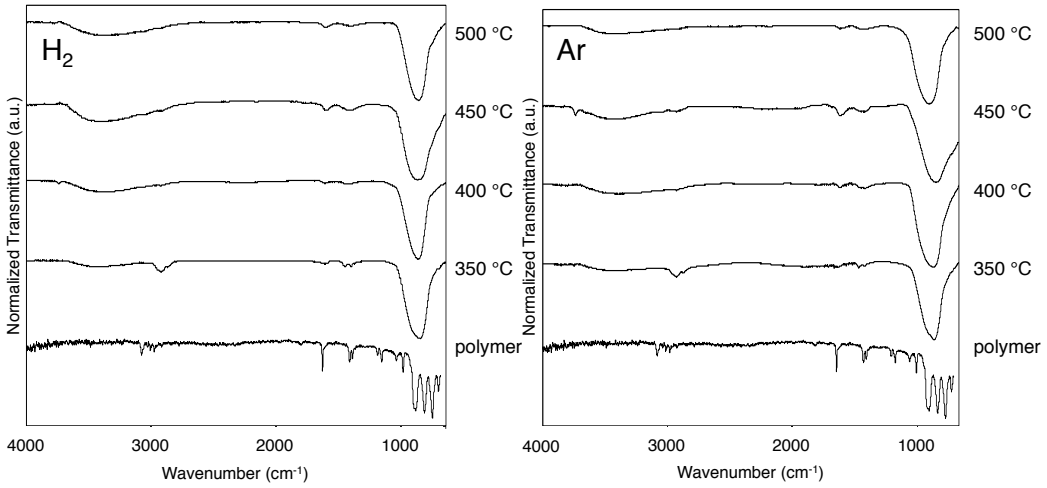

Figure A10. FT-IR spectra of **3** processed at indicated peak temperatures for one hour in 5% H_2/95% Ar (left) or 100% Ar atmosphere (right).

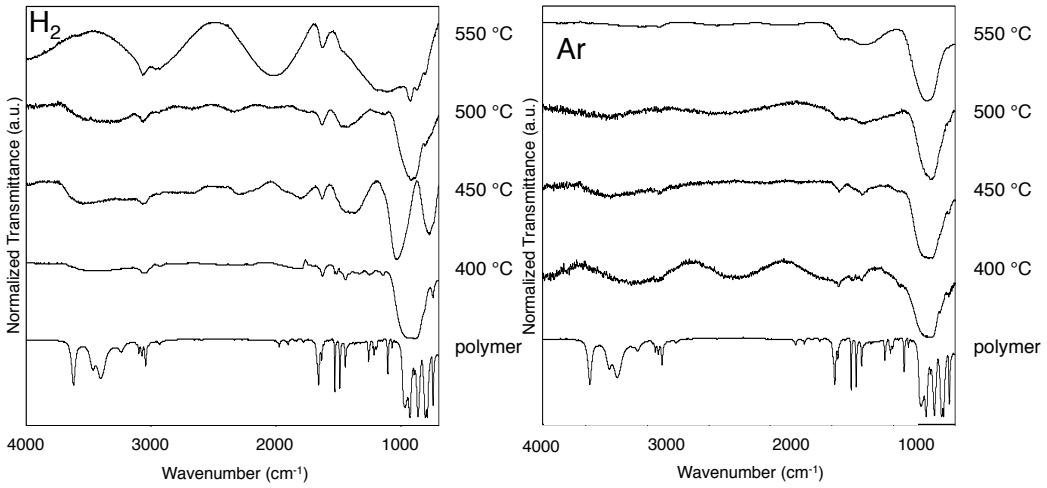

Figure A11. FT-IR spectra of **4** processed at indicated peak temperatures for one hour in 5% H_2/95% Ar (left) or 100% Ar atmosphere (right).

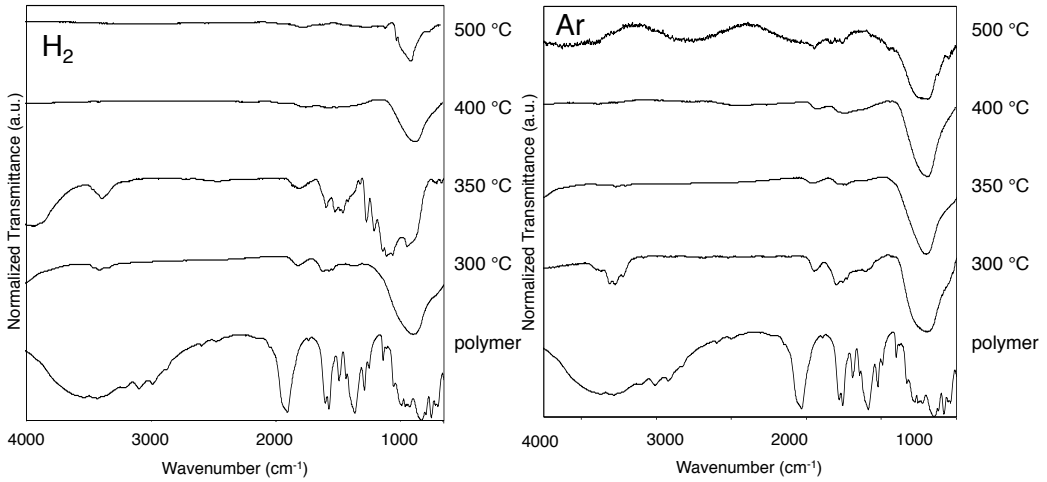

Figure A12. FT-IR spectra of **5** processed at indicated peak temperatures for one hour in 5% H_2/95% Ar (left) or 100% Ar atmosphere (right).

Appendix B:

Oxide, semiconductor and metal patterned surfaces based on sol-gel chemistry within block-copolymer micelles

A portion of this chapter has been published:

Rodriguez Núñez, J. R.; Johnson, M.; Veinot, J. G. C. MRS Proc. ***2011****, 1359, 187-192.*

B.1 Introduction

In very general terms, nanomaterial synthesis involves the isolation and stabilization of nanometer-sized structures. This can be achieved in different ways, including electrostatic repulsion between surfaces,[1,2] application of protective surface coatings that impart solubility and thus prevent agglomeration,[3,4] or embedding the nanomaterial in a matrix, for example oxides (as seen in Chapter 2) or polymers.[5,6] One class of polymers that afford spatial segregation is block-copolymers (here diblock-copolymers, of generic structure A_n-B_m). They will separate into domains based upon the different chemical properties of the two blocks that make up each polymer chain. Factors that direct this self-assembly into different sizes and shapes are block and solvent polarity, block lengths, and interaction between the two blocks.[7,8]

The localization of reagents and/or reactions into one of the block copolymer units can be desirable for different reasons. A large body of work uses block-copolymer self-assembly in three dimensions to generate mesoporous materials for a variety of applications.[9-11] Thin film examples include the patterning of solution-processible floating gate memory, and photovoltaic devices.[12-14] Another area of research is developing block copolymer patterning as bottom-up approach in fabrication of electronics, where the production of defect-free patterns is an art that is still being refined.[15-19]

In the work described in this chapter, block copolymers were used to localize Si nanocrystal precursors (hydrogen silsesquioxane, HSQ) and induce sol-gel chemistry (i.e., hydrolysis and condensation or suitable precursors) in

nanodomain patterns on substrates. Block-copolymers were chosen such that one block incorporated functional groups (*i.e.*, containing a basic functionality) suitable to catalyze sol-gel chemistry – this approach precluded adding other reagents to induce reaction.

B.1.1. Block-copolymer mediated patterning

Block-copolymers are ordered, non-random polymers composed of terminally connected homopolymer blocks (*i.e.*, AAA-BBB-CCC). The diblock-copolymers investigated here are made up of a non-polar (polystyrene) and a polar (poly-4-vinylpyridine or polymethylmethacrylate) block (Scheme B.1). Based upon the straightforward concepts of "like dissolves like", blocks of the same type tend to interact, leading to self-assembly in selective solvents. Some structures that can be obtained by solution-phase self-assembly of block copolymers and in the solid state are shown in Scheme B.2.

Scheme B.1. Structural formula of (A) Polystyrene-*block*-poly-4-vinylpyridine (PS-*b*-P4VP) and (B) Polystyrene-*block*-polymethylmethacrylate (PS-*b*-PMMA).

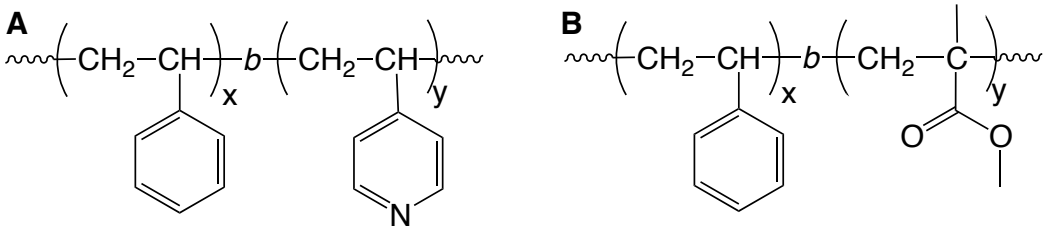

Scheme B.2. Examples of block copolymer self-assembly in solution (B-F) and in the solid state (G): (A) Schematic representation of AB-diblock copolymer, (B) vesicle, (C) micelles, (D) inverse micelles, (E) lamellar blocks, (F) cylindrical or tubular micelle, (G) equilibrium morphologies in the solid state (S: spherical, C: cylindrical, G: gyroidal, L: lamellar). Adapted from refs. 20-22.

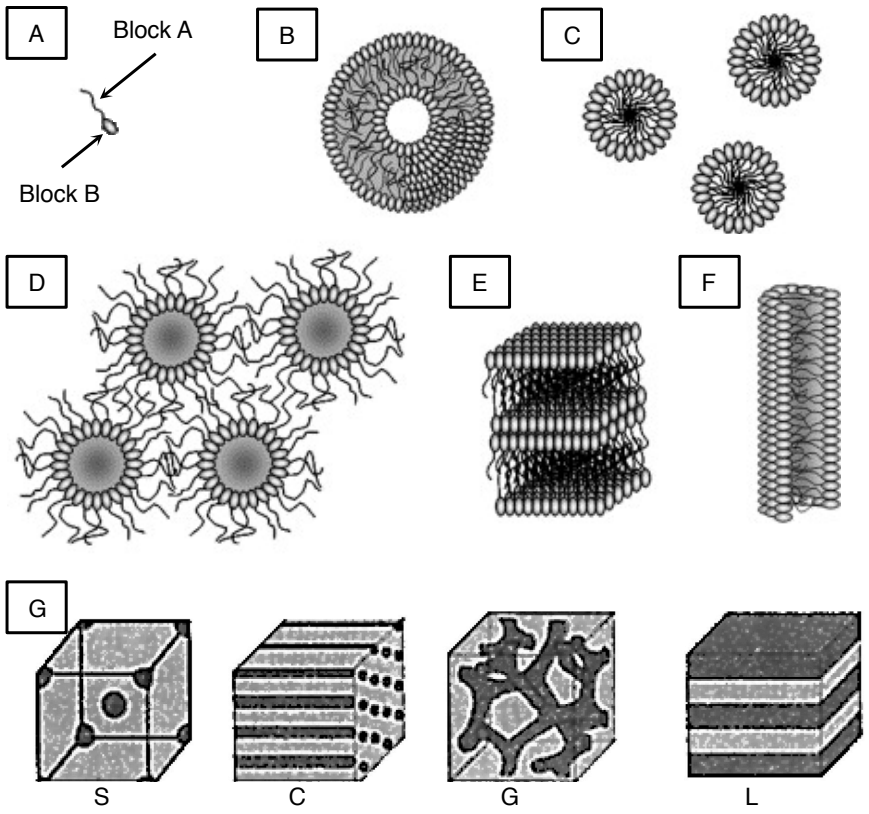

The differences between the two ends of each polymer chain cause block-copolymers to self-assemble yielding different structures, offering their application as templating agents. The self-assembly process may be directed controlling factors such as concentration, type and length of respective blocks, solvent composition, post-deposition annealing, interaction with the substrate and pre-existing surface patterns (*e.g.*, from lithography).[12,16,20-23] In this way,

different surface structures comprised, for example, of dots or lines can be produced.[12,15,16,22,24-26]

The polymer blocks may be tailored to achieve selective interactions of one of the blocks with other chemical entities. In this way, block-copolymer patterns may be exploited as a pattern template. After self-assembly in the presence of an appropriate precursor, patterns of metals or oxides may be produced by procedures such as the application of a plasma, or addition of a reducing agent or catalyst with appropriate characteristics to be taken up into the same block as the reagent. Ideally, tailoring of the blocks can progress to a point where blocks not only interact, but also exhibit selective reactivity. The following discussion presents an example in which a basic side-chain (i.e., pyridine) of a BCP is used to catalyze sol-gel chemistry and induce patterning.

B.1.2. Sol-Gel Reactions

Sol-gel methods are "soft chemical" (*chimie douce*) approaches used in the synthesis of oxide materials.[27] The chemical processes taking place in sol-gel reactions are hydrolysis and condensation (See: Equations B.1 and B.2). These reactions lead to formation of a sol (a solution of colloidal particles) that subsequently crosslinks to form a gel (a network of sol particles with encapsulated solvent). The gel is aged and dried to obtain the final product. Sol-gel reactions are generally carried out in aqueous or alcoholic solution, but can also occur in organic solvents (involving water, or nonhydrolytically under anhydrous conditions).[27,28]

$$Si(OR)_4 + 4\ H_2O \rightarrow Si(OH)_4 + 4\ ROH \qquad (B.1)$$

$$n\ Si(OH)_4 \rightarrow (SiO_2)_n + 2n\ H_2O \qquad (B.2)$$

In the context of this work, the catalysis of the hydrolysis and condensation reactions is of particular interest. Here, we differentiate between acid- and base-catalyzed reactions. This classification does not, however, revolve around a pH of 7, but is relative to the point of zero charge (PZC) of the material (*e.g.*, SiO_2 or GeO_2). The PZC is the pH at which surface groups are neither protonated nor deprotonated.[27]

At pHs below the PZC, hydroxyl groups are protonated and acid catalysis takes place. In acid catalysis of Si and Ge sol-gel reactions (Scheme B.2.A), the first step involves protonation of a hydroxyl or alkoxyl group. Protonation creates a good leaving group, and the positively charged oxygen further reduces electron density at the Si or Ge, making it susceptible to nucleophilic attack. Hydrolysis occurs when water acts as a nucleophile and attacks the Si or Ge centre. Condensation occurs when a Si-OH (or Ge-OH) functional group acts as a nucleophile. In the final step, the catalytic proton is released to generate the hydrolyzed or condensed product.[27]

At pHs higher than the PZC, hydroxyl groups are deprotonated and base catalysis occurs (Scheme B.2.B). In this case, a hydroxide or alkoxide (in the case of hydrolysis) or sila-/germanolate (in the case of condensation) attacks the Si or Ge center of a neutral molecule, displacing a hydroxyl or alkoxyl group.[27]

Scheme B.3. Mechanisms of (A) acid- and (B) base-catalyzed sol-gel reaction of Si or Ge alkoxides (adapted from ref. 28).

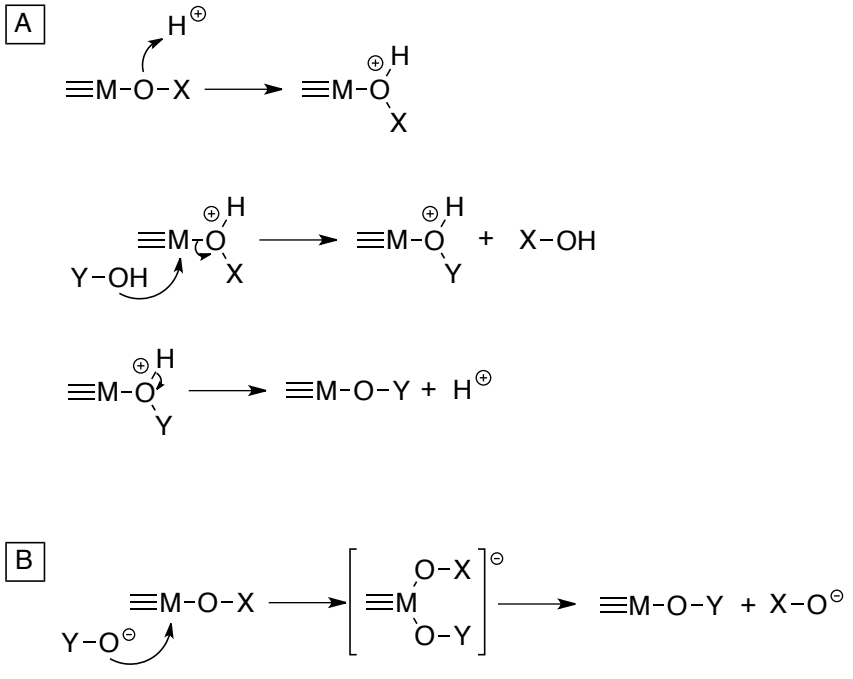

B.1.3. Scope of this Work

The idea to study block-copolymers in conjunction with methods of nanocrystal synthesis developed in our group had two directions: i) Using block-copolymers to achieve spatial separation of individual oxide-embedded nanocrystals, and ii) to localize and pattern the products of sol-gel reactions. In the former approach (i), hydrogen silsesquioxane, a Si-NC precursor, was selectively taken up into the P4VP units and converted to SiO_2-embedded Si-NCs

by thermal processing. These annealing conditions also removed the block-copolymer template leaving SiNC/SiO_2 patterns.[29] The latter approach (ii) was aimed at the synthesis of a sol-gel derived precursor suitable for the formation of Ge patterns upon thermal reduction. This was achieved using a block-copolymer possessing a basic side chain (i.e., pyridine) with the ability to catalyze hydrolysis and condensation reactions. In this chapter, we show preliminary results from patterning of Ge sol-gel chemistry on surfaces. Tetraethoxygermane was reacted within the P4VP units of a PS-*b*-P4VP polymer pattern on a Si wafer to produce patterns of GeO_2. Sol-gel patterns of GeO_2 were subsequently reduced to Ge upon heating above 450 °C in a hydrogen containing atmosphere.[30,31]

B.2 Experimental Details

B.2.1 Material Preparation

B.2.1.1 Reagents and Materials

m-xylene ($C_6H_4(CH_3)_2$, anhydrous, ≥99%) was purchased from Aldrich. Tetraethoxygermane (TEOG, $Ge(OC_2H_5)_4$, >99.99% metal basis) was purchased from Gelest and stored in an argon-filled glovebox. Poly-styrene-*block*-poly-4-vinylpyridine (PS-*b*-P4VP, MW 57500-*b*-18500) and poly-styrene-*block*-poly-methylmethacrylate (PS-*b*-PMMA, MW 123000-*b*-35000) were purchased from Polymer Source Inc. Palladium nitrate ($Pd(NO_3)_2 \cdot xH_2O$, ~40% Pd, Pd 99.9%) was purchased from Strem Chemicals. Cupric sulfate ($CuSO_4$, anhydrous, 97.8%) was purchased from Fisher Scientific. All reagents were used as received.

B.2.1.2 Silicon and germanium oxide patterns

2 wt% PS-*b*-P4VP solution in *m*-xylene was stirred for 24 h at 70 °C. PS-*b*-P4VP solution was mixed with equal volume of 2 wt% TEOG solution in *m*-xylene and gently shaken. 50 μL of this mixture was dropped by autopipet onto a Si wafer piece of 1.5 cm side length mounted in a spin-coater. The wafer was spun at 3000 rpm for 45 s. To improve pattern alignment, the wafer was annealed in a Pyrex desiccator filled with 22 mL 10:1 THF:H_2O mixture for 20 h. Thermal processing in a tube furnace for 15 min at 400 °C (heating rate 9 °C/min) in air yielded spot patterns of silicon or germanium oxide that were analyzed by AFM, XPS and Auger mapping.

B.2.1.3 Conversion of germanium oxide patterns to germanium patterns

Patterns of germanium oxide on Si were converted to elemental germanium by thermal reduction with hydrogen gas. Wafers were prepared as above, but the thermal processing protocol was adjusted as follows: processing was carried out for 20 min at 400 °C (heating rate 9 °C/min) followed by 470 °C for 1 h (heating rate 18 °C/min). After 15 min at 400 °C in air, the furnace tube was flushed with 20% H_2 (balance Ar) for 5 min, and processing at 470 °C proceeded in a static 20% H_2 atmosphere. After processing, samples were treated as air-sensitive, and were transferred from the tube furnace immediately into a glovebox.

B.2.1.4 Conversion of germanium patterns to metal patterns

Metal patterns were generated from elemental germanium *via* galvanic displacement reaction. The wafers were removed from the glovebox and immediately immersed in 10 mL 1.3 mM $Pd(NO_3)_2$ and 10 mM $CuSO_4$ solutions. After 1 min exposure, the wafers were washed with copious amounts of Millipore water followed by ethanol and dried in a stream of N_2.

B.2.2 Material Characterization

B.2.2.1 Thermogravimetric Analysis (TGA)

TGA was carried out using a Perkin-Elmer Pyris TGA equipped with Pyris Thermal Analysis 7.0 software. Samples were placed in a platinum pan and heated in air from room temperature to 600 °C at 10 °C/min.

B.2.2.2 Atomic Force Microscopy (AFM)

AFM was performed on a Dimension 3100 Atomic Force Microscope (Digital Instruments) using tapping mode with Si tips (Nanoworld, 4.6 μm thick, 160 μm long, 45 μm wide, 285 kHz resonance frequency and 42 N/m force constant). Both height and phase images were collected, though height images are used exclusively in this chapter.

B.2.2.3 X-Ray Photoelectron Spectroscopy (XPS)

XPS was performed on an AXIS-165 XPS spectrometer from Kratos Analytical at the Alberta Centre for Surface Engineering and Science (ACSES), University of Alberta. The base pressure and operating pressure in the chamber were maintained at $\leq 10^{-7}$ Pa. A monochromatic Al K_α X-ray (λ = 8.34Å) was used to irradiate the samples at a power of 210 W. To control sample charging, the charge neutralizer filament was used during the experiment. The pass energy for the survey and the high-resolution spectra were 160 and 20 eV, respectively. Spectra were calibrated to the C 1s emission at 284.8 eV attributed to adventitious carbon using CasaXPS (VAMAS) software. Following calibration, the background of each spectrum was subtracted using a Shirley-type background to remove most of the extrinsic loss structure.

B.3 Results and Discussion

Self-assembled PS-*b*-P4VP has previously been demonstrated as a template for free-standing mesoporous oxides *via* sol-gel synthesis.[32] However, this procedure employs a preformed sol. In the current study, the role of PS-*b*-P4VP was extended to the dual function of catalyst and patterning agent to obtain nanoscale surface patterns of sol-gel materials. Obtained by a straightforward method with few possible contaminants, these patterns can be developed for applications in electronics, photovoltaics and optics, and can act as precursors for further transformation.[12,26,33,34]

B.3.1 Patterning of GeO_2

PS-*b*-P4VP forms spherical micelles that arrange into pseudo-hexagonal patterns on a Si wafer when spin-coated from *m*-xylene solution, as observed by atomic force microscopy (AFM, Figure B.1.A). Since this polymer contains a basic pyridine unit, we explored its use for concurrent patterning and catalysis of the sol-gel reaction of tetraethoxygermane (TEOG). Solutions of PS-*b*-P4VP and TEOG were mixed and spin-coated on Si wafers, followed by processing in a tube furnace for 15 min at 400 °C in air. The processing step removes the BCP by pyrolysis, which was confirmed both by AFM of the substrate (Figure B.1.B) and thermogravimetric analysis (TGA) of PS-*b*-P4VP (Figure B.1.C). AFM shows remnants of the BCP pattern that are negligible in height, while TGA confirms complete mass loss around 400 °C. In the absence of BCP, TEOG forms deposits

of different sizes and shapes (with diameters ranging from 25 to 150 nm and heights ranging from 4 to 16 nm) on the Si surface, and no particular ordering is evident (Figure B.1.D). However, in the presence of BCP, patterns comparable to the pseudo-hexagonally arranged spheres in the parent BCP are observed after processing (Figure B.1.E). The spheres or discs vary in diameter and height (diameters ~40-90 nm, heights ~15-35 nm), but are generally much higher than in the parent BCP (compare Figure B.1.A, diameters ~25-70 nm, heights ~1.5-4 nm). The observation of a peak for a binding energy around 33 eV in X-ray photoelectron spectroscopy (XPS) confirms the presence of Ge^{4+} (Figure B.1.F).[35]

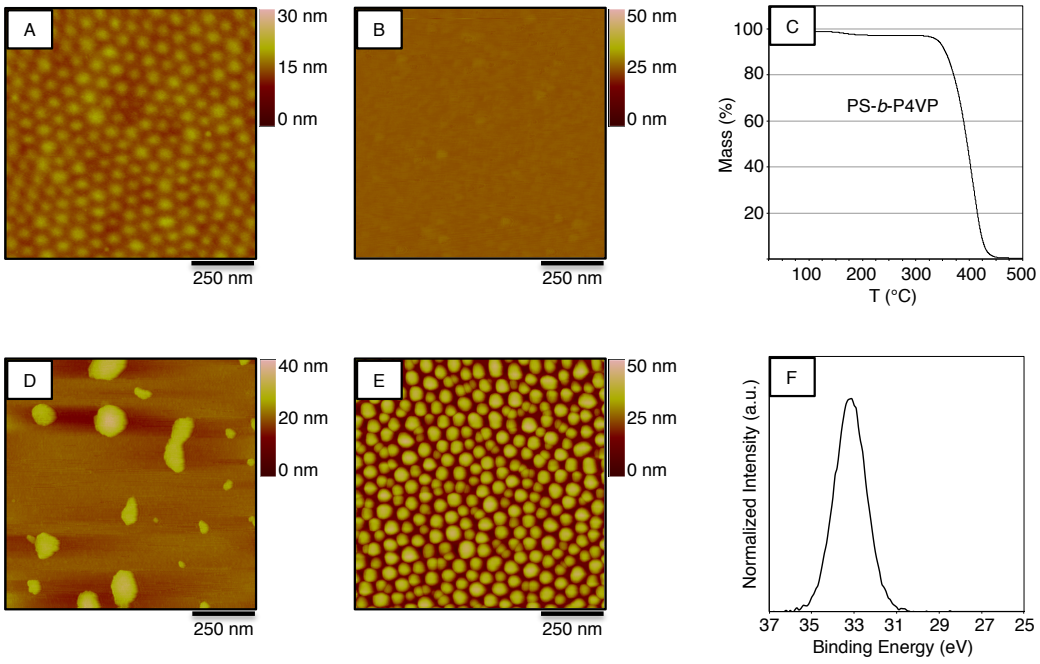

Figure B.1. Atomic Force Microscopy (AFM) images of (A) PS-*b*-P4VP (annealed), (B) PS-*b*-P4VP (annealed and processed in air), (C) Thermogravimetric Analysis (TGA) of PS-*b*-P4VP in air, (D) TEOG (annealed and processed in air), (E) PS-*b*-P4VP with TEOG (annealed and processed in air), and (F) X-ray Photoelectron Spectroscopy (XPS) of the Ge 3d region for (E).

To confirm the necessity of a basic unit in one of the polymer blocks, a second polymer that lacks such functionality, PS-*b*-PMMA, was investigated. The block copolymer pattern obtained after 24 h solvent annealing in THF/H_2O displayed some inconsistencies, with some areas showing line patterns, and others showing very sparse dots in AFM (Figure B.2.A and B). After mixing with TEOG and processing, AFM of the obtained structures (Figure B.2.C) compares better to results obtained without block copolymer present (Figure B.2.F), than to the more uniform patterns obtained with patterning of PS-*b*-P4VP (Figure B.2.E). These results suggest that it is the base functionality of the pyridine units that aids both sol-gel reaction and the patterning process.

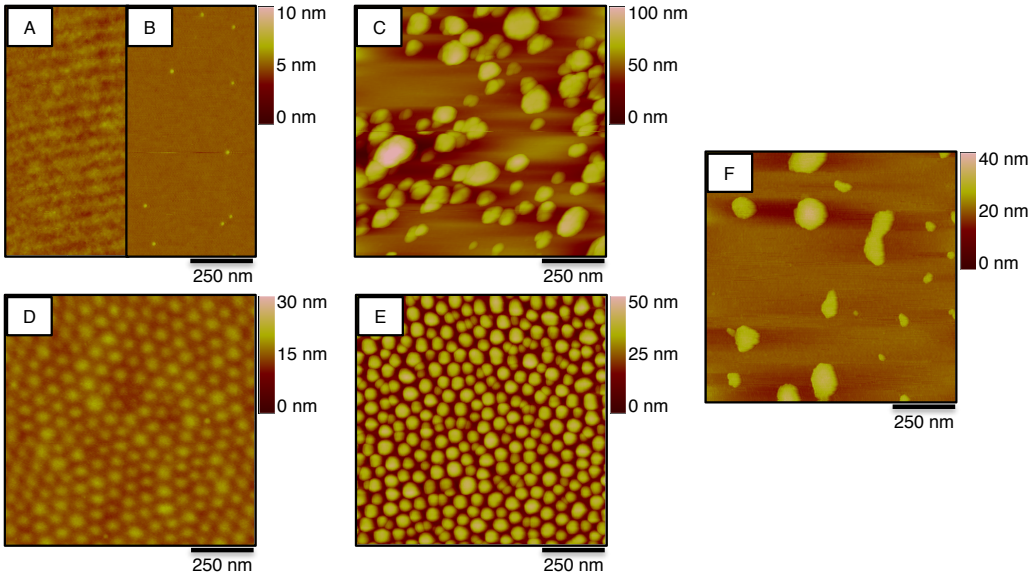

Figure B.2. AFM images of (A-B) PS-*b*-PMMA (annealed), (C) PS-*b*-PMMA with TEOG (annealed and processed in air), (D) PS-*b*-P4VP (annealed), (E) PS-*b*-P4VP with TEOG (annealed and processed in air), and (F) TEOG blank (annealed and processed in air).

The hydrophilic pyridine unit is proposed to localize water from the atmosphere within the P4VP moieties of BCP micelles. Pyridine will react with water to form hydroxide ions, which will catalyze hydrolysis and condensation of TEOG to form crosslinked GeO_2 (see Scheme B.3).

Scheme B.4. Proposed crosslinking mechanism for sol-gel reaction of TEOG in the presence of P4VP and trace water.

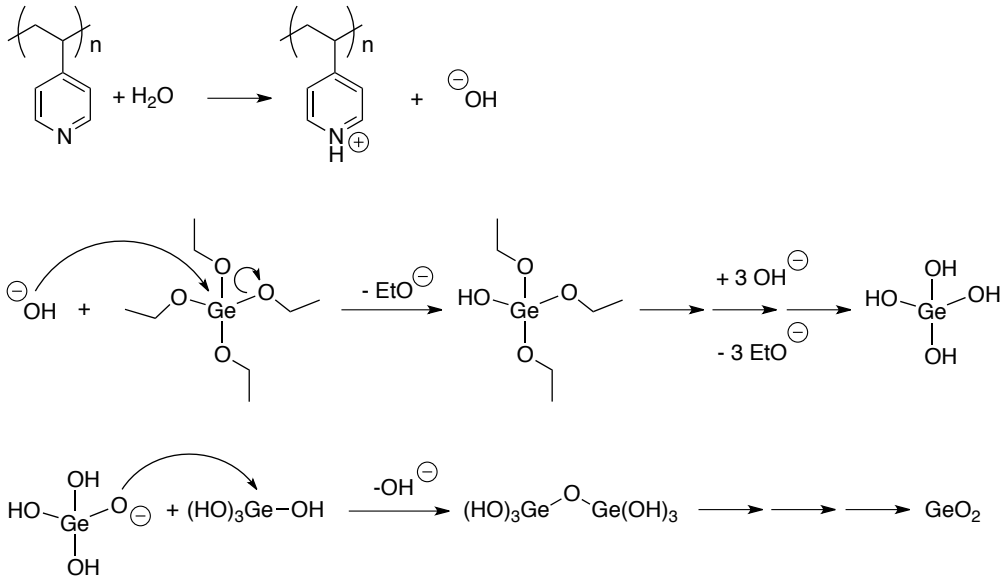

B.3.2 Conversion of GeO_2 patterns to elemental Ge

Hydrogen gas can reduce germanium oxides to elemental Ge at relatively low temperatures (≥ 450 °C).[30,31] By thermally processing above this temperature in an atmosphere of 20% H_2, the GeO_2 patterns could be converted to elemental Ge. AFM shows a reduction in domain size compared to GeO_2 (Figure B.3.d, e and f). This can be attributed both to evaporation of Ge and GeO_x at elevated temperatures, and to shrinkage due to removal of oxygen. XPS confirms the reduction to elemental Ge by observation of a peak at a binding energy of ~30 eV (Figure B.3.a, b).[35]

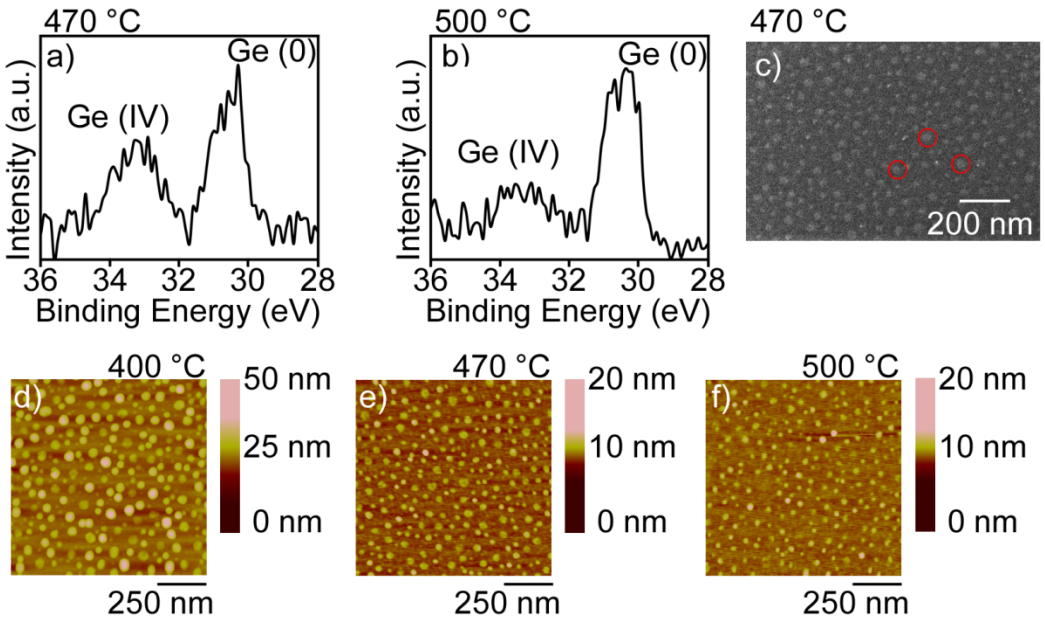

Figure B.3. XPS of the Ge 3d region for PS-*b*-P4VP/TEOG processed at (a) 470 °C in 20% H_2, and (b) 500 °C in 20% H_2; (c) Scanning electron micrograph of PS-*b*-P4VP/TEOG processed at 470 °C in 20% H_2; AFM images of PS-*b*-P4VP/TEOG processed at (d) 400 °C in air, (e) 470 °C in 20% H_2, and (f) 500 °C in 20% H_2.

B.4 Conclusions and Future Work

In conclusion, functional block copolymer patterning using PS-*b*-P4VP was able to locally catalyze sol-gel reactions and create surface patterns of GeO_2. Comparison with a block copolymer lacking basic side groups, PS-*b*-PMMA, suggests the presence of pyridine units is key to localized sol-gel reaction of tetraethoxygermane. By thermal reduction, GeO_2 patterns were converted to elemental Ge.

Patterns of elemental Ge can be converted to Ge/metal heterostructures, or to metal patterns. Based on the low reduction potential of Ge in comparison to many metals, this may proceed through a spontaneous electroless deposition process.[18,36-42]

This technique can also be extended to other sol-gel reactions for patterning of technologically interesting materials, for example to produce thin patterned layers for sensors, photovoltaics, and ultimately electronics, if this method is fully developed for such applications.[26,43-45]

B.5 References

(1) Schneider, C.; Hanisch, M.; Wedel, B.; Jusufi, A.; Ballauff, M. *J. Colloid Interface Sci.* **2011**, *358*, 62–67.
(2) Holman, Z. C.; Kortshagen, U. R. *Nano Lett.* **2011**, *11*, 2133–2136.
(3) Murray, C. B.; Norris, D. J.; Bawendi, M. G. *J. Am. Chem. Soc.* **1993**, *115*, 8706–8715.
(4) Kelly, J. A.; Veinot, J. G. C. *ACS Nano* **2010**, *4*, 4645–4656.
(5) Khoury, El, J. M.; Caruntu, D.; O' Connor, C. J.; Jeong, K.-U.; Cheng, S. Z. D.; Hu, J. *J. Nanopart. Res.* **2007**, *9*, 959–964.
(6) Maeda, Y.; Tsukamoto, N.; Yazawa, Y.; Kanemitsu, Y.; Masumoto, Y. *Appl. Phys. Lett.* **1991**, *59*, 3168–3170.
(7) Hayward, R. C.; Pochan, D. J. *Macromolecules* **2010**, *43*, 3577–3584.
(8) Bates, F. S.; Fredrickson, G. H. *Annu Rev Phys. Chem.* **1990**, *41*, 525–557.
(9) Hsueh, H.-Y.; Ho, R.-M. *Langmuir* **2012**, *28*, 8518–8529.
(10) Shen, C.; Shaw, L. L.; Zhang, L. C.; Thomas, E. L. *J. Sol-Gel Sci. Technol.* **2012**, *63*, 72–84.
(11) Warren, S. C.; Perkins, M. R.; Adams, A. M.; Kamperman, M.; Burns, A. A.; Arora, H.; Herz, E.; Suteewong, T.; Sai, H.; Li, Z.; Werner, J.; Song, J.; Werner-Zwanziger, U.; Zwanziger, J. W.; Grätzel, M.; DiSalvo, F. J.; Wiesner, U. *Nat. Mater.* **2012**, *11*, 460–467.
(12) Darling, S. B. *Prog. Polym. Sci.* **2007**, *32*, 1152–1204.
(13) Wei, Q.; Lin, Y.; Anderson, E. R.; Briseno, A. L.; Gido, S. P.; Watkins, J. J. *ACS Nano* **2012**, *6*, 1188–1194.
(14) Guldin, S.; Docampo, P.; Stefik, M.; Kamita, G.; Wiesner, U.; Snaith, H. J.; Steiner, U. *Small* **2011**, *8*, 432–440.
(15) Tseng, Y.-C.; Darling, S. B. *Polymers* **2010**, *2*, 470–489.
(16) Black, C. T.; Ruiz, R.; Breyta, G.; Cheng, J. Y.; Colburn, M. E.; Guarini, K. W.; Kim, H. C.; Zhang, Y. *IBM J. Res. & Dev.* **2007**, *51*, 605–633.
(17) Chai, J.; Wang, D.; Fan, X.; Buriak, J. M. *Nat. Nanotechnol.* **2007**, *2*, 500–506.
(18) Aizawa, M.; Buriak, J. M. *Chem. Mater.* **2007**, *19*, 5090–5101.
(19) Wu, N. L. Y.; Zhang, X.; Murphy, J. N.; Chai, J.; Harris, K. D.; Buriak, J. M. *Nano Lett.* **2012**, *12*, 264–268.
(20) Rodriguez Hernandez, J.; Checot, F.; Gnanou, Y.; Lecommandoux, S. *Prog. Polym. Sci.* **2005**, *30*, 691–724.
(21) Alexandridis, P. *Curr Opin Colloid Interface Sci* **1996**, *1*, 490–501.
(22) Kim, H.-C.; Park, S.-M.; Hinsberg, W. D. *Chem. Rev.* **2010**, *110*, 146–177.
(23) Zhang, X.; Harris, K. D.; Wu, N. L. Y.; Murphy, J. N.; Buriak, J. M. *ACS Nano* **2010**, *4*, 7021–7029.
(24) Kim, H.-C.; Hinsberg, W. D. *J Vac Sci Technol A* **2008**, 1369–1382.
(25) Biswas, A.; Bayer, I. S.; Biris, A. S.; Wang, T.; Dervishi, E.; Faupel, F. *Adv. Colloid Interface Sci.* **2012**, *170*, 2–27.

(26) Herr, D. J. C. *J. Mater. Res.* **2011**, *26*, 122–139.
(27) Schubert, U.; Hüsing, N. *Synthesis of Inorganic Materials*; 3rd ed. Wiley-VCH: Weinheim, 2005.
(28) Vioux, A. *Chem. Mater.* **1997**, *9*, 2292–2299.
(29) Rodríguez Núñez, J. R.; Johnson, M.; Veinot, J. G. C. *MRS Proc.* **2011**, *1359*, 187–192.
(30) Baba, H. *Bull. Chem. Soc. Jpn.* **1956**, 789–793.
(31) Hasegawa, R.; Kurosawa, T.; Yagihashi, T. *J. Jpn. Inst. Met.* **1970**, 132–137.
(32) Chen, D.; Park, S.; Chen, J.-T.; Redston, E.; Russell, T. P. *ACS Nano* **2009**, *3*, 2827–2833.
(33) Parker, A. R.; Townley, H. E. *Nat. Nanotechnol.* **2007**, *2*, 347–353.
(34) Schacher, F. H.; Rupar, P. A.; Manners, I. *Angew. Chem. Int. Ed.* **2012**, *51*, 2–26.
(35) *http://srdata.nist.gov/xps*.
(36) Fasasi, A.; Griffiths, P. R.; Scudiero, L. *Appl. Spectrosc.* **2011**, *65*, 750–755.
(37) Scudiero, L.; Fasasi, A.; Griffiths, P. R. *Appl. Surf. Sci.* **2011**, *257*, 4422–4427.
(38) Sayed, S. Y.; Buriak, J. M. *ACS Appl. Mater. Interfaces* **2010**, *22*, 3515–3524.
(39) Brejna, P. R.; Griffiths, P. R.; Yang, J. *Appl. Spectrosc.* **2009**, *63*, 396–400.
(40) Carraro, C.; Maboudian, R.; Magagnin, L. *Surf Sci Rep.* **2007**, *62*, 499–525.
(41) Aizawa, M.; Buriak, J. M. *J. Am. Chem. Soc.* **2005**, *127*, 8932–8933.
(42) Zhang, J.; Gao, Y.; Hanrath, T.; Korgel, B. A.; Buriak, J. M. *Chem. Commun.* **2007**, 1438–1440.
(43) Hutter, E.; Fendler, J. H. *Adv. Mater.* **2004**, *16*, 1685–1706.
(44) La Fata, P.; Cordella, F.; Puglisi, R.; Lombardo, S.; Bongiorno, C. *Superlattices Microstruct.* **2008**, *44*, 693–698.
(45) Cha, M.-A.; Shin, C.; Kannaiyan, D.; Jang, Y. H.; Kochuveedu, S. T.; Ryu, D. Y.; Kim, D. H. *J. Mater. Chem.* **2009**, *19*, 7245.